CRANFIELD UNIVERSITY

Hao Li

Aerodynamic Analysis and Experiment of a Micro Flapping Wing Rotor

School of Aerospace, Transportation and Manufacture

MSc by Research
Academic Year: 2014 - 2015

Supervisor: Dr. Shijun Guo

March 2015

CRANFIELD UNIVERSITY

School of Aerospace, Transportation and Manufacture

MSc by Research

Academic Year 2014 - 2015

Hao Li

Aerodynamic Analysis and Experiment of a Micro Flapping Wing Rotor

Supervisor: Dr. Shijun Guo

March 2015

This thesis is submitted in partial fulfilment of the requirements for the degree of MSc by Research

ABSTRACT

This project is aimed at developing a bio-inspired flyable micro/nano aerial vehicle (MAV) of high agility and performance capable of vertical take-off and landing and hovering (VTOLH). To achieve the aim, a novel flapping wing rotor (FWR) concept invented by Dr. Guo has been adopted, which is ideal for MAVs of sub 60 gm and especially for nano scale of sub 5 gm according to aerospace industry's definition.

The advantages and potential of the FWR concept for MAV development has been studied consistently by Dr. Guo's research team in the last five years. However making a flyable micro FWR model especially in sub 5gm and demonstrate its VTOLH feasibility remains as a big challenge and has not been achieved in previous projects. To meet the above objective, the first achievement in the project is the successful design, build and test of a flyable micro FWR model (FWR-EX1) of only 3 gm based on off-the-shelf available micro motor. The key breakthrough is to achieve the necessary large aeroelastic twist of the flapping wing during the upstroke in an adaptive manner for structural and aerodynamic efficiency.

To achieve the next objective for design and performance improvement, study has also been focused on deeper scientific understanding and analysis of the FWR mechanisms. Attention has therefore been paid to a systematic study on aerodynamic modelling and efficiency of the FWR. The method is based on a revised quasi-steady aerodynamic model that combines the theoretical method and experimental data. The numerical results of the revised quasi-steady aerodynamic model are in agreement with existing results obtained via CFD methods. Based on the model and analysis, the optimal kinematics for the FWR has been determined. Subsequently a comparison of the FWR aerodynamic efficiency was made with two other most studied configurations of MAVs, the insect flapping wing and rotorcraft.

As part of the further development for a step change of the technology readiness, investigation has been extended into the design and analysis of a

multi-bar mechanical amplifier, which is of high mechanical efficiency and suitable for nano scale MAVs. Within the designed MAV scale, the results show a maximum amplification ratio of 28 can be obtained. The ratio and efficiency of the system can be further enlarged with the elastic joint and resonance effect of the mechanism. A physical model has also been made and tested to demonstrate the concept and design.

The objectives set for the research has been successfully achieved. The author has made the following knowledge contribution to this particular research field.

- Achievement of large aeroelastic twist of the flapping wing in theory and practice.
- Extend the quasi-steady aerodynamic model to FWR based on test data from micro traditional flapping wing and rotorcraft.
- Analysis of the optimal kinematics of motion for the FWR and evaluation of its efficiency and potential application in comparison with other competitive alternative MAVs.

The current research has paved the way towards the next steps in studies consisting of aeroelasticity, dynamic stability and control of a practical FWR MAV.

Keywords:

Flapping Wing Rotor, MAV, VTOLH, quasi-steady aerodynamics, efficiency.

ACKNOWLEDGEMENTS

First of all I would like to acknowledge my supervisor Dr. Shijun Guo for his valuable guidance and advice throughout the research work, and providing a critical view to the topics covered and the conclusions reached at every stage.

I would also like to acknowledge Dr. YanLai Zhang for his advice and discussions, which has been very helpful for my research work.

In addition, I would like to express my regards to my fellow student Yin Liu and visiting student Chao Zhou and Hanhan Mao for the time spent together at the laboratory working on our flyable FWR test model and sharing valuable ideas.

Finally, I owe my greatest gratitude to my family for their words of support and encouragement, which have always given an extra push to my motivation for undertaking such an academic challenge.

TABLE OF CONTENTS

LIST OF FIGURES

LIST OF TABLES

LIST OF ABBREVIATIONS

FWR	Flapping wing rotor
MAV	Micro aerial vehicle
ISTAR	Intelligence, surveillance, target acquisition and reconnaissance
VTOLH	Vertical take-off and landing and hovering
LEV	Leading edge vortex
CFD	Computational fluid dynamics
AoA	Angle of attack
DPIV	Digital particle image velocimetry
SHF	Simple harmonic function
CP	Centre of pressure
DARPA	Defence Advanced Research Projects Agency
AU	Geometric AoA at mid-downstroke
AD	Geometric AoA at mid-upstroke

LIST OF NOTATIONS

ρ	Air density
R	Wing length
$\bar{c}$	Mean chord length of wing
ϕ	Flapping amplitude
α	Angle of attack
$\hat{r}$	Non-dimensional radial position along the wing span
$\hat{c}(\hat{r})$	non-dimensional chord length
C_L	Lift coefficient
C_D	Drag coefficient
C_N	Normal force coefficient of thin airfoil
U_∞	Free stream velocity
$\hat{x}_0$	Non-dimensional location of the rotational axis
ω	Rotation rate
C_{rot}	Coefficient of rotational circulation
$\widehat{\omega}$	Non-dimensional angular velocity of wing rotation
U_t	Wing tip velocity
C_T	Translational lift coefficient
C_R	Rotational lift coefficient
Γ	Circulation
Ω_i	Angular velocity of Euler angle
I_i	Moment of inertia
τ^{aero}	Aerodynamic torque
ω_0	Induced velocity at actuator disc
A	Area of the actuator disc
β	Stroke plane deviation angle
k_{ind}	Correction factor for non-uniform downwash distributions
ψ	Euler angle for describing rotation of FWR wing
ϕ	Euler angle for describing flapping of FWR wing
α	Euler angle for describing pitching of FWR wing
$\mathbf{R}$	Rotation matrix
$\boldsymbol{\omega_i}$	Angular velocity vector of the FWR wing in the inertial frame

$\boldsymbol{\omega}$	Rotation rate of the FWR wing in the wing-fixed frame
$\mathbf{U}(\mathbf{r})$	velocity vector of the 2D wing section at span-wise location r
$\dot{\mathbf{U}}(\mathbf{r})$	Acceleration vector of the 2D wing section at span-wise location r
u_x	Velocity of the 2D wing section at x_w axes
u_y	Velocity of the 2D wing section at y_w axes
$\dot{u}_x$	Acceleration of the 2D wing section at x_w axes
$\dot{u}_y$	Acceleration of the 2D wing section at y_w axes
α_e	Effective angle of attack
ψ_0	Rotation speed of FWR wing
f	Flapping frequency
$\Delta\Phi$	Flapping amplitude
$\Delta\alpha$	Pitching amplitude
α_0	Zero pitching angle
α_u	Geometric AoA at mid-upstroke
α_d	Geometric AoA at mid-downstroke
$\hat{\mathrm{r}}_1(\mathrm{S})$	The first radius of non-dimensional moment of wing area
$\hat{\mathrm{r}}_2(\mathrm{S})$	The second radius of non-dimensional moment of wing area
$\hat{\mathrm{r}}_3(\mathrm{S})$	The third radius of non-dimensional moment of wing area
AR	Wing aspect ratio
x_{pitch}	The location of the pitching axis with respect to leading edge
$\hat{h}$	Non-dimensional local coordinate of the semi-chord
$c(r)$	Local chord length of the 2D wing section
$\mathbf{C_t}(\boldsymbol{\alpha_e})$	Quasi-steady force coefficient
C_l	Lift coefficient in lift and drag frame
C_d	Drag coefficient in lift and drag frame
C_{Lmax}	Emprical value of quasi-steady coefficient
C_{Dmax}	Emprical value of quasi-steady coefficient
C_{D0}	Emprical value of quasi-steady coefficient
C_H	Horizontal force coefficient
C_V	Vertical force coefficient
x_{cp}	Chord-wise location of CP
λ_y	Added mass coefficient

$\lambda_{y\omega}$	Added mass coefficient
λ_{ω}	Added mass coefficient
$\mathbf{\Omega}$	Angular velocity vector
$\mathbf{F_q}$	Quasi-steady force vector
$\mathbf{M_q}$	Quasi-steady moment vector
$\mathbf{F_a}$	Added mass force vector
$\mathbf{M_a}$	Added mass moment vector
$\dot{m}$	Mass flow rate across the control surface
$\mathbf{U_{in}}$	Inflow velocity vector
$\mathbf{U_{induced}}$	Induced velocity vector
$\hat{\mathbf{n}}$	Unit normal vector of the control surface
Φ_e	Equivalent stroke amplitude
ψ	Stroke plane deviation angle
P^{aero}	Time averaged power output
l	Instantaneous lift
τ_r	Instantaneous rotational torque
p	Instantaneous power
Re	Reynolds number
C_M	Instantaneous rotational torque coefficient
$\bar{C}_L$	Mean lift coefficient
$\bar{C}_M$	Mean rotational torque coefficient
C_P	Power coefficient
U_{ref}	Reference velocity
η	Velocity ratio of rotation to flapping
$\hat{\dot{\phi}}$	Non-dimensional flapping angular velocity
$\mathrm{P_f}$	Hover flight power factor
β	The angle of velocity deflection due to vertical flapping motion
α_i	The angle due to induced downwash
υ	Kinematic viscosity of the fluid
n	Rotational speed
$M_{flapping}$	Flapping drive moment
$T_{pitching}$	Reaction torque of wing pitching

1 INTRODUCTION

1.1 General Background

Micro aerial vehicles (MAVs) or micro UAVs have attracted increasing research effort and investment on developing relevant technologies especially in the last decade. This is due to their advantages for potential applications in civil and military operations, especially intelligence, surveillance, target acquisition and reconnaissance (ISTAR) missions in highly complex and risky environments and inside buildings.

The versatile flight skills of insect flapping wing such as hovering, escaping, landing and vertical take-off along with the small size and energy efficiency all meet the demand of MAVs. Therefore, bio-inspired flight model has initiated numerous MAV programs around the world such as the DelFly of TU Delft; Nano Hummingbird of AeroVironment Inc.; Robotic Insect of Harvard[1] (see Figure 2-5).

However the previous attention and development on bio-inspired MAVs were mainly focusd on mimicking the flapping wing in a so-called figure-of-eight kinematics of insects. In 2009, Guo et al. [2] proposed an alternative flapping wing rotor (FWR) concept of novel configuration that combines both insect-like (dragonfly) flapping wing and the man-made rotation machinery (rotorcraft). Its feasibility of flapping and simultaneously rotating of the wing was demonstrated in an initial test. Their later investigations of numerical modelling show that high lift can be achieved by giving enough amplitude of the flapping motion[3].

Recent investigations regarding insect flight are mainly focused on the unsteady aerodynamics in very low Reynolds number (Re, 10^2~10^4). This is because most insect flight fall into this regime [4]. Ellington [4] and Dickinson et al.[5], used a semi-empirical quasi-steady aerodynamic model to predict the aerodynamic forces generated by insect wing. Sun et al.[6-8] employed computational fluid dynamics (CFD) method to predict the aerodynamic forces and power of insect flight. These previous studies have revealed the

aerodynamic mechanisms manipulated by flying insects, which mainly include: stable LEV, rotational forces, added mass forces and wake capture [4; 5; 9].

In terms of aerodynamic efficiency, Wang [10] used a simplified two stroke flapping wing comparing with steady airfoil, and analysed their power efficiency for hovering flight. Later Umberto and Wang [11] used 2D CFD method also comparing the power efficiency between flapping flight and steady flight in hovering, their result showed that flapping flight may be more power efficient in optimal stroke motion. In the experimental study of Lentink and Dickinson[12], however, the man-made rotary wing exhibits superior aerodynamic efficiency than insect flapping wing at a wide range of Reynolds number (100~14000). Though, it seems that insect flapping wing is superior in control and maneouvre through delicate alteration of the wing kinematics.

In this study, instead of mimicking insect flapping flight, the potential improvement and technology of the FWR are investigated, which combines both the flight model in nature (dragonfly) and the man-made machinery (rotary wing).

1.2 **Objectives**

The aim of this project is to develop a flyable FWR MAV of high agility and performance with the capability of vertical take-off, landing and hovering (VTOLH). The objectives towards the aim are described below.

- Establish a theoretical framework for the aerodynamic analysis of the FWR at very low Reynolds number and create a quasi-steady aerodynamic model to predict the aerodynamic force and power produced by a micro FWR.
- Validate the aerodynamic model against CFD results, and determine the optimal flapping kinematics of motion for the FWR by using the model.
- Evaluate the aerodynamic power efficiency of the FWR and compare with two other existing configurations namely the traditional flapping wing and rotorcraft wing, which are competitive alternative MAVs in terms of performance.

- Design, build and experiment of FWR and finally a flyable micro FWR test model under 6gm to demonstrate the FWR's potential capability of VTOLH. The work includes the mechanical system, model build-up, aerodynamic force measurement and experimental test.

1.3 **Thesis Outline**

This thesis is structured in four parts according to the study contents covered in the project and the approach taken in each chapter.

The first part of the thesis corresponds to the literature review of the relevant research field, which is broadly covered in chapter 2. Firstly, some background on micro aerial vehicles (MAVs) is presented with a focus on their main specifications and applications. The up-to-date technologies regarding bio-inspired MAVs are also presented, followed by a review of the kinematics and aerodynamic mechanisms of the insect flapping flight. The final part of this chapter covers the quasi-steady aerodynamic theory and the mathematical models, which are widely used by previous researchers for analysing the aerodynamic forces and power of flapping flight.

Chapters 3 and 4 constitute the second part of the thesis and contain the complete theoretical and numerical aerodynamic analysis of the FWR. In chapter 3, a quasi-steady aerodynamic model for the FWR configuration is developed and validated based on previous studies on insect flight. The critical kinematic parameters of this configuration are identified. The lift and rotational torque production and aerodynamic power efficiency of the FWR configuration is further analysed in chapter 4. The optimal kinematics of the wing at equilibrium rotational speed for FWR MAV is given. The optimal aerodynamic efficiency of FWR is further compared with insect flapping wing and rotorcraft.

The third part of the thesis covers the design, manufacture and experimental testing of the FWR MAV. Chapter 5 deals with the structure of the wing for optimal asymmetric and passive pitching motion and experiments. The trend of change of the lift production with the pitching rigidity of the passive pitching wing is outlined based on the experimental results. The complete design-test process

of a light weight flyable FWR MAV (FWR-EX1) is presented in chapter 6. The instantaneous and mean lift production and initial flight demonstration is also presented, together with data analysis and discussions.

In order to pave the way towards more efficient FWR MAV, the study has been extended to the design, analysis, fabrication and test of a novel 5-bar mechanical thorax device. It is aimed at developing a micro flapping mechanism of large amplification ratio. This part of study is presented in chapter 7.

Finally, chapter 8 contains the relevant and most significant conclusions reached throughout the numerical and experimental studies on the development of the FWR MAV.

2 LITERATURE REVIEW

2.1 The Micro Air Vehicles

2.1.1 Definition and specifications

The term micro air vehicle or MAV corresponds to a new class of unmanned flight vehicles characterised by its small dimensions and its wide variety of applications. This revolutionary aircraft concept was initially defined by the Defence Advanced Research Projects Agency (DARPA) in the 1990's, as a category of unmanned air vehicles limited by a maximum size of 15 cm in each physical dimension and weighing no more than 50 grams [13].

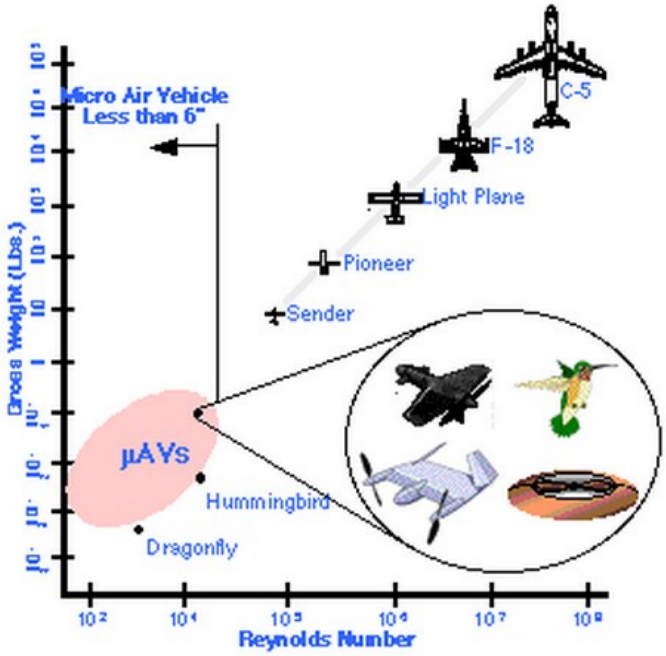

Figure 2-1 The Micro Air Vehicle (MAV) Flight Regime Compared to other Flight Vehicles (Reproduced from[13]).

MAVs typically operate at Reynolds numbers range between 10^2 and 10^4, which are much lower than those characteristic for conventional aircraft. The comparison of vehicle gross weight VS Reynolds number is depicted in Figure 2-1 above. It can be seen that the Reynolds number for MAVs, as defined by DARPA, has more similarities with that for insects and small birds rather than other conventional aircraft concepts.

Among other relevant characteristics of micro aerial vehicles there are flight autonomy and flight range. These requirements are established according to the kind of mission to be developed by the vehicle, but they are limited by the restrictions in terms of size and weight imposed to the propulsive system and the power supply system. Typical values for flight autonomy and flight range are determined from[13] as 20 to 60 minutes and 10 km, respectively.

2.1.2 **MAV applications**

The uniqueness of the characteristics of MAVs, especially their small size and agility, makes them suitable for a wide range of missions which are not possible for any other systems. Most of these missions are based on the ability of MAVs to operate in constrained urban environments and even inside buildings.

Intelligence, surveillance and reconnaissance (ISR) missions: MAVs have tremendous advantages in performing ISR missions. They can be remotely operated by individual soldiers in the battle field for local reconnaissance. This advantage is boosted in civil environments, where their stealth capabilities are best exploited. Furthermore, they are also applied to many other ISR missions such as prevention of maritime terrorism, detection of hostile units on the battle field or real-time detection and analysis of biological or chemical agents in infected environments.

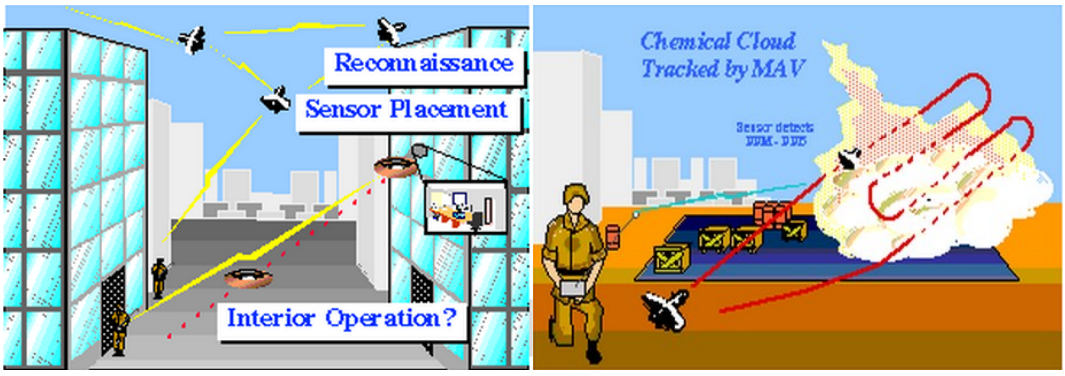

Figure 2-2 Urban operations and detection of biological or chemical agents in infected environments missions for the MAV (Reproduced from[13]).

Armed reconnaissance and suppression of enemy air defences: MAVs can be equipped with sensors and miniaturised warheads in order to make them

capable of attacking high-value enemy targets such as radars. The global positioning system allows precise autonomous navigation and position reporting for micro aerial vehicles, which are critical for this type of missions[14].

Search and rescue: Due to its small size and reduced weight, MAVs can be packed in some specific units, such as the ejection seat mechanism of a fighter aircraft, to provide reconnaissance information and send rescue signals in eventual requirement of search and rescue operations [14].

Structural health monitoring: Large structures such as bridges have to be continually inspected for cracks and fatigue. This inspection is carried out manually by a single inspector, or inspection crew, which can be complicated by areas that are difficult to access. MAVs with the ability to hover can perch on the structure, therefore, could be used to access difficult areas so that an easier, and less hazardous remote inspection could be performed. Furthermore, health monitoring of large distances of pipeline can also be performed with MAVs equipped with sensors to detect leaks.

2.1.3 **Existing MAV types**

2.1.3.1 **Fixed wing**

Fixed wing MAVs are simply small airplanes that use fixed lifting surfaces to provide lift for flight, and use control surfaces to provide directional control. They are typically used for comparatively long endurance outdoor missions. So far, a large number of different fixed-wing MAV designs have been developed around the world (see Figure 2-3 below).

Figure 2-3 Fixed wing Wasp MAV (left) and Black Widow (right) developed by DARPA (Reproduced from internet source).

2.1.3.2 **Rotary wing**

Rotary-wing MAVs are essentially small helicopters. These vehicles are mainly intended for short endurance indoor and outdoor missions that require hovering capability (such as ISTAR missions). Same as fixed-wing MAVs, many different rotary-wing MAVs have been developed, some of which are mentioned below.

Figure 2-4 Rotary wing Black Hornet developed by Prox Dynamics AS (left); Quadcopter, BLADE NANO QX BNF (right) (Reproduced from internet source).

2.1.3.3 **Flapping wing**

The flapping wing MAVs are the category of micro UAVs that operate by a pair of insect-like (or bird-like) wings. There are typically two kinds of flapping wing MAVs: bird-like and insect-like. The kinematics of the two are slightly different. The bird-like flapping wing MAVs use flapping wing to generate the propulsive force for flight, and the wing operates more like a fixed airfoil. The insect-like

flapping wing MAVs, however, directly use the flapping motion of the wing for lift generation. Compared with fixed wing and rotary wing, flapping wing flight offers the abilities of sustained hover and agile manoeuvres in confined spaces such as birds and insects in nature, therefore, it is especially suitable for indoor applications and complex environments. Many researchers and engineers in the last decade are trying to mimic this flight model, some of the developed flapping wing MAVs are listed below.

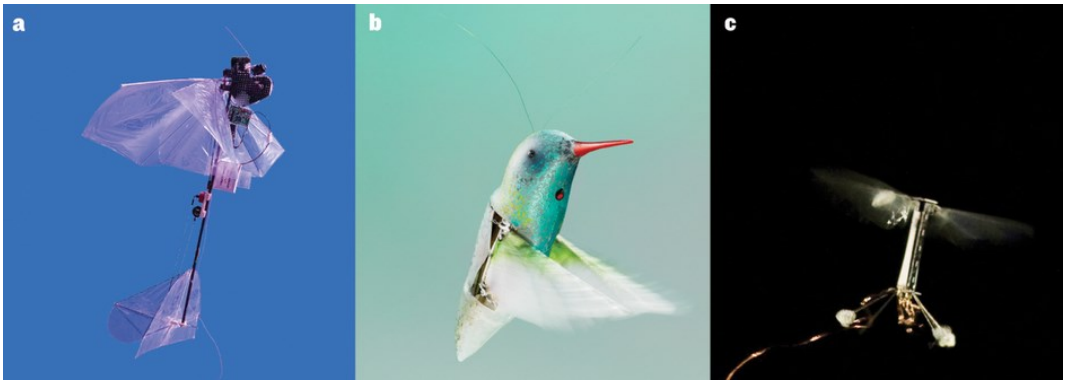

Figure 2-5 (a) DelFly of TU Delft; (b) Nano Hummingbird of AeroVironment Inc.; (c) Robotic Insect of Harvard (Reproduced from[1]).

2.2 **Mechanisms of Insect Flapping Flight**

2.2.1 **Kinematics of flapping wing**

For small scale flapping wing flyers, the flow field around the wing is highly unsteady, and the aerodynamic force generation is susceptible to the kinematics of the wing (translation and pitching rotation). Insects in nature utilize the alteration of the detailed wing kinematics (stroke amplitude, angle of attack, timing and duration of wing rotation, and stroke-plane deviation) in association with the unsteady effects to change the aerodynamic force production, in order to control and manoeuvre. Therefore, the kinematics of insect flapping wing is first reviewed.

2.2.1.1 **Flapping cycle**

The flapping cycles of most insect wings are composed of a downstroke and an upstroke. At each stroke, the wing translates at a relatively constant angle of

attack from its most aft (or forward) position to its most forward (or aft) position. The wing accelerates from the beginning of each stroke to a constant or peak angular velocity around mid-stroke, after which the wing begins to decelerate and reverses its direction at the beginning of the subsequent stroke. At the stroke reversal, the wing rotates about a longitudinal axis and changes the angle of attack. The rotations of the wings at the end of upstroke and downstroke are termed as pronation and supination, respectively. Figure 2-6 shows the typical flapping cycle of insect flapping wing.

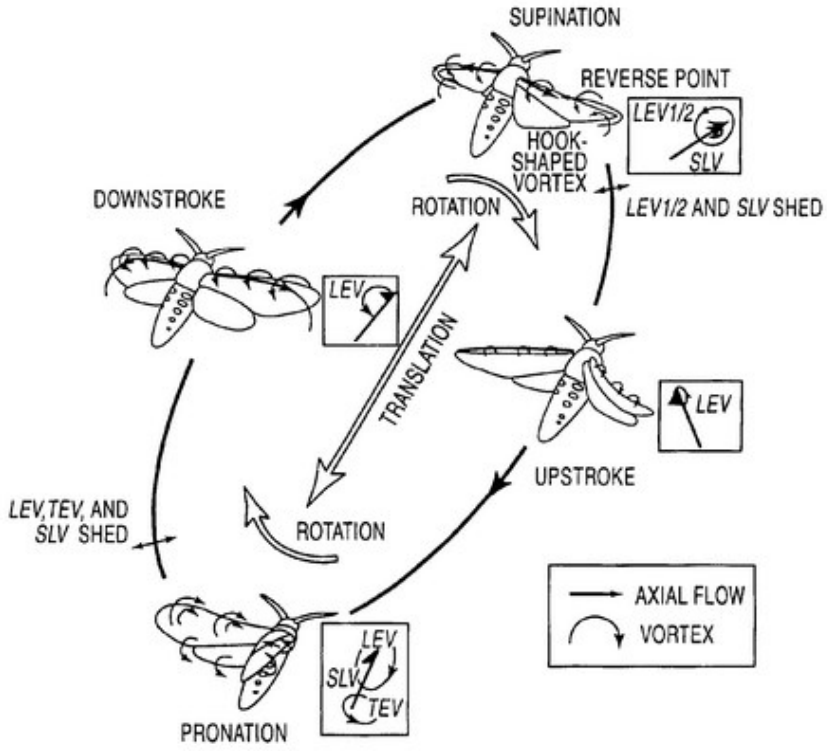

Figure 2-6 Typical flapping cycle of insect flapping wing (Reproduced from[15]).

For insect flight, the translation of the wing covers large portion of the flapping period. Supination and pronation are, however, largely confined to the acceleration and deceleration at the end of each half-stroke, and are approximately equal in duration. Each lasts 10%~20% of the whole flapping period [16].

2.2.1.2 **Flapping stroke plane and tip paths**

The flapping motion of the wing can be described in a stroke plane. The wing translation of the upstroke and downstroke mainly occurs in the stroke plane. During translation, the wing will also deviate from the stroke plane. The typical wing tip paths of the Bumble Bee (*Bumbus Hortorum*) of different flight tests are shown in Figure 2-7 below.

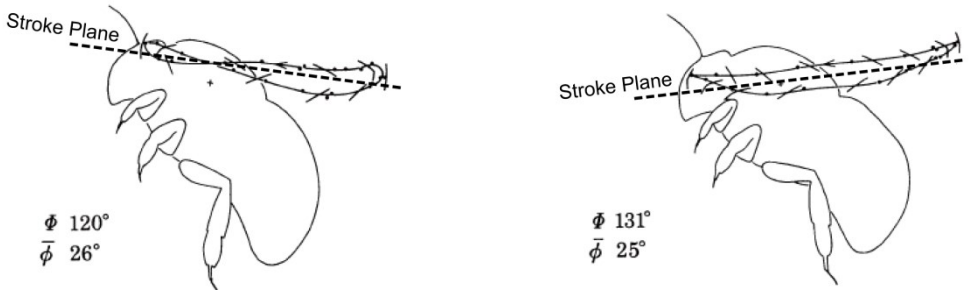

Figure 2-7 Typical wing tip paths of the Bumble Bee (*Bumbus Hortorum*) of different flight tests. The left shows the figure-of-eight tip path; the right shows banana-type shape (Reproduced from[16]).

The wing tip paths of insect flapping wing can take on many shapes, including ellipses, arcs, banana-type shapes and figure-of-eight [16]. The latter one is most commonly considered for the recent investigations on insect flight and engineering design [17; 18]. Although the tip paths of insect flight vary, the majority of the aerodynamic force is produced at the mid-stroke, where the translational velocity of the wing reaches its maximum. Therefore, the deviation of the wing from the stroke plane can be neglected in most studies [16].

2.2.1.3 **Horizontal and inclined flapping motion**

There are typically two kinds of kinematic patterns of flapping wing: Some insects (fruit fly, hawkmoth, bumble bee, etc.) adapt flapping wing motion at horizontal stroke plane in a so-called figure-of-eight kinematics for lift generation. For this flight model, the pitching of the wing is nearly symmetric, and has equal geometric angle of attack (AoA) at upstroke and downstroke (for hovering flight) [16]. On the other hand, dragonfly uses inclined or vertical flapping stroke plane to generate lift. The pitching of the wing at upstroke and downstroke is asymmetric, which leads to a different geometric AoA at each

flapping stroke. The two typical kinematic patterns are shown in Figure 2-8 below.

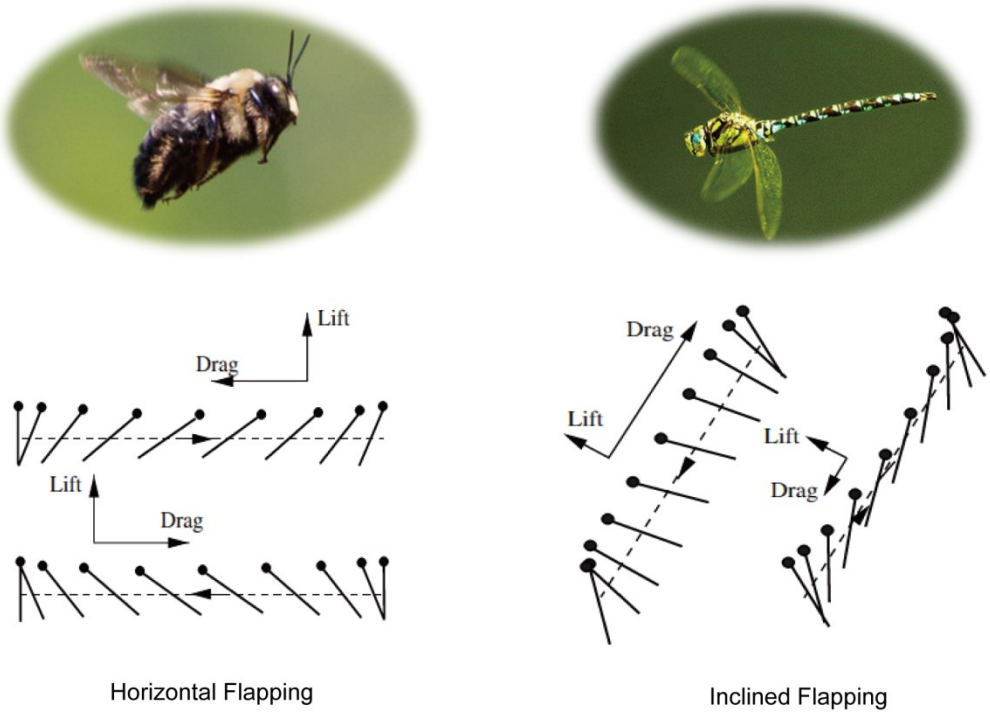

Figure 2-8 Typical kinematic patterns of insect flapping flight. Horizontal flapping with symmetric angle of attack (left); inclined flapping with asymmetric angle of attack (right) (Reproduced from[19]).

The asymmetric pitching of the dragonfly wings results in a net drag force over a stroke period, accompanying by an inclined flapping stroke plane, the drag force will contribute to the upward vertical lift [20] (see Figure 2-8). This distinct kinematic pattern differs from most of the other insects of the symmetric pitching and horizontal stroke plane, where the drag force is attributed to be the penalty for lift production. Wang [20] showed that by properly manipulate the drag force of the inclined flapping kinematics, the aerodynamic efficiency may be substantially improved.

2.2.2 **Aerodynamic mechanisms**

The basic aerodynamic mechanisms that dominate the fly of insects, birds and other flyers that uses flapping wing for flight can be found on many existing literature [4; 5; 21]. Here we will simply review the classical knowledge without

giving any detailed explanations of the aerodynamic theory, for it is not the intention of this study to extend these well-established theories.

According to previous researchers [4; 5; 21], the aerodynamic mechanisms that is thought to be used by flying insects mainly include: *Stable LEV, Rotational circulation, Virtual mass force, Wake capture, and Clap and fling mechanism*.

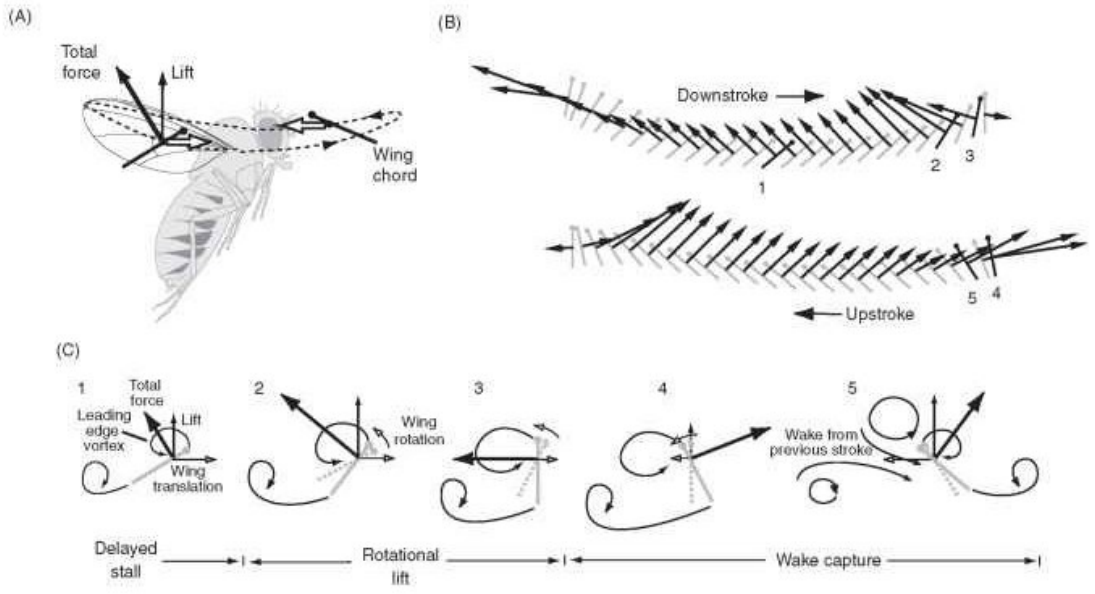

Figure 2-9 Basic unsteady aerodynamic mechanisms of insect flapping flight. *Stable LEV, Rotational Force, Added Mass Inertia and Wake Capture* (Reproduced from internet source).

2.2.2.1 **Stable LEV**

During the translational process of the flapping stroke, the flow separates at the leading edge of the wings and grows into a vortex that covers large part of the wing surfaces and merges with the tip vortex at wing tip, this vortex forms a low pressure region on the upper surface of the wing and therefore increases the lift. This phenomenon is recognized as the stable LEV (as shown in Figure 2-10).

In the recent investigation on revolving wings (Usherwood and Ellington [22]), the stable LEV is also found in steadily revolving of the model hawkmoth (*Manduca sexta*) wing in Re~10^3. This indicates that a rotary wing with low

aspect ratio and works in Re~10^3 may also generate a high lift force that is identical to the lift generated by flapping wing during the translational process.

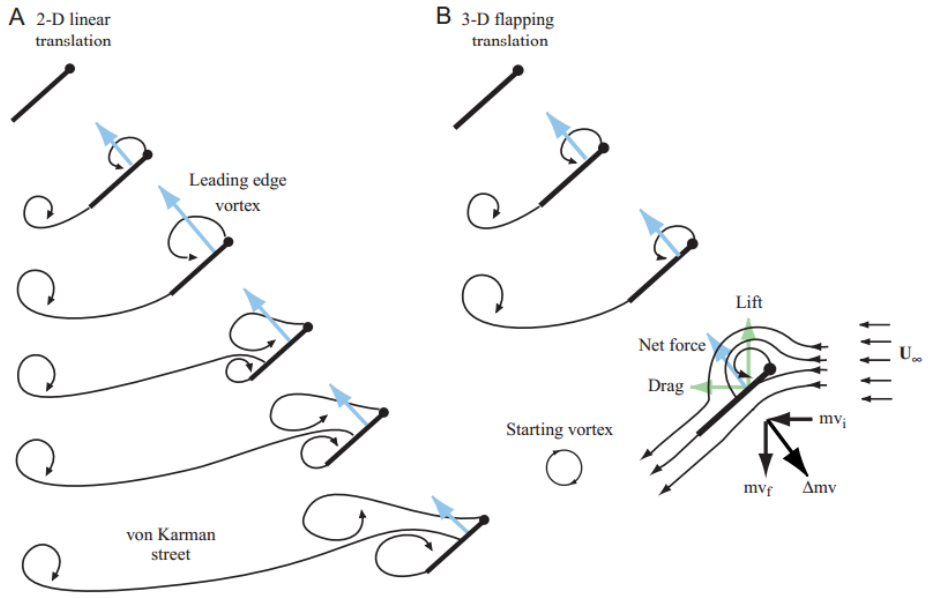

Figure 2-10 Comparison of unstable and stable LEV on 2D airfoil and 3D airfoil, respectively. (A) A translating 2D airfoil generates a leading and trailing edge vortex. During translation, the leading edge vortex and trailing edge vortex perform cyclic shedding, forming a von Karman vortex street. (B) For a 3D translating airfoil, the axial flow stabilizes LEV on the upper surface of the wing which augments the force generation (Reproduced from[23]).

2.2.2.2 **Rotational force (Kramer effect)**

During the rapid rotation of the flapping motions, the wings will experience a change in fluid force (increase or decrease) to a level beyond steady state values. When the wing rotates about the pitching axis while at the same time translating, flow around the wing deviates from the Kutta condition and the stagnation region moves away from the trailing edge. This causes a sharp, dynamic gradient at the trailing edge, leading to shear. As the fluids tends to re-establish the Kutta condition at the trailing edge, additional circulation will be generated on the wing. In other words, the wing generates a rotational circulation in the fluid to counteract the effects of rotation. Therefore, rotational forces will be generated that either add to or subtract from the net force due to translation, depending on the direction of rotation [23]. This phenomenon can

be described by the ‘Kramer effect’ [24], or alternatively as ‘rotational forces’ [5; 25].

2.2.2.3 **Added mass effect**

When an insect accelerates its wings, it will set the surrounding air in motion, therefore the inertia of the wing is increased by the mass of the air that is accelerated [5]. This apparent increase in wing mass is known as Virtual mass. This virtual mass can be comparable to the wing mass itself for some insects [4], and is affected by wing geometry and flapping kinematics. Virtual mass will affect instantaneous forces on the wing, and will cause extra power consumption.

2.2.2.4 **Wake capture**

The reciprocating motion of insect wings suggests there may be interactions between the vortex shedding and the wing. As proposed by Dickinson et al. [5; 26] that the wing recapturing shed vorticity from the previous half stroke will add to the wing’s bound vorticity and therefore enhance lift. The wake capture of flapping wing serves as a way that an insect recovers energy from the air that was lost during the previous stroke, which in turn improves the aerodynamic efficiency of force production [5].

2.2.2.5 **Clap and fling**

Another aerodynamic mechanism that is thought to be exploited by insects is the Clap and Fling mechanism, which was found by Weis-Fogh [21] in flight characteristics of small wasp (*Encarsia Formosa*). In this mechanism, the wings come together dorsally at the end of the upstroke to perform a 'clap', after the clap the wings 'fling' apart, air is sucked in as the wings start to move downwards creating a bound vortex on each of the wings which produces an instantaneous high lift force. This mechanism is shown in Figure 2-11.

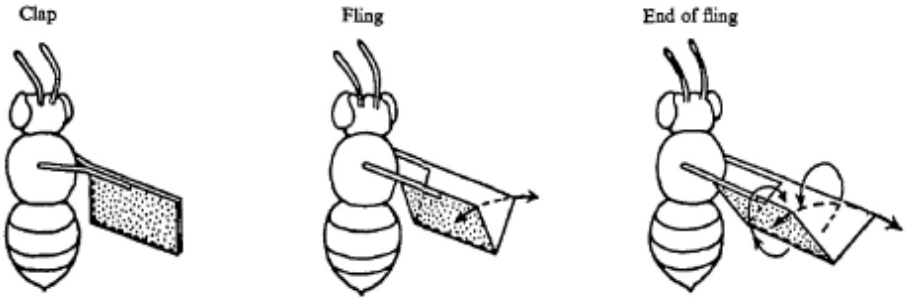

Figure 2-11 The Clap and Fling mechanism (Reproduced from[21]).

In the above aerodynamic mechanisms, The Clap and Fling mechanism does not apply to most insects. Generally, the most prominent aerodynamic mechanism for insects flight at low Reynolds number is the delayed stall of LEV, which accounts for 80% of the average lift generated by insect wing[7], the remaining three mechanisms are significant only in the case that the acceleration at the beginning and the deceleration near the end of a stroke are very large [7].

2.2.2.6 **LEV stability of FWR**

For a typical rotary wing with low aspect ratio and working at low Reynolds numbers (Re~10^3), the axial flow exists so as to stabilize the leading edge vortex (LEV) in a similar manner with flapping wing during translation. Usherwood and Ellington [22] confirmed this by experimentally analysis the revolving hawkmoth (*Manduca sexta*) wing. Although it seems that for the back-and-forth motion of the flapping wing, the wing typically travels 3 to 5 chord lengths (within 180° of flapping amplitude), therefore, the LEV should be more stable than the rotary wing case, however, the critical Reynolds number that the LEV become unstable and perform cyclic shedding for the rotary wing is unknown. In the experiment of Usherwood and Ellington [22], the Reynolds number is as high as Re~8071, and still observed a stable LEV.

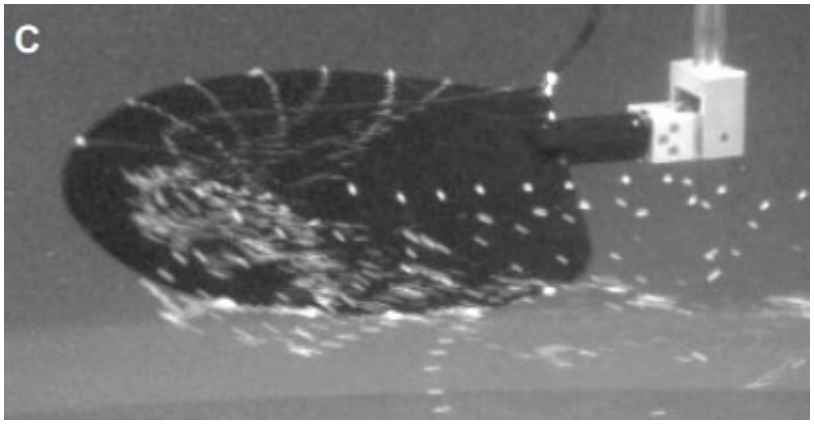

Figure 2-12 Stable LEV on a revolving model fruit fly (*Drosophila Melanogaster*) wing (Reynolds number~110) (Reproduced from[12]).

Lentink and Dickinson [12] found that the stability of the LEV depends only on the radius of gyration of the wing and is governed by Rossby Number[12; 27; 28]:

$$Ro = \frac{U}{Lf} \tag{2-1}$$

Where U and L are, respectively, characteristic velocity and length scales of the phenomenon and $f = 2\Omega sin\varphi$ is the Coriolis frequency. Lentink and Dickinson showed that for hovering insect flight, this dimensionless number is equivalent to single wing aspect ratio[12]:

$$Ro = AR_s = \frac{R}{\bar{c}} \tag{2-2}$$

with a low Ro (of order 1), the gyration of a wing (such as propeller, rotorcraft and also FWR) is most likely to maintain a stabilized LEV and has augmented fluid force. Due to the similarity in wing kinematics, FWR manipulates similar aerodynamic mechanisms as insect flapping wing, which can be largely explained by the stably attached leading edge vortex (LEV)[29]. In the 3D CFD numerical investigation of Wang et al.[29], it is observed that at Re~9000, a strong LEV still exists for the flapping and rotating wing and contributes to a high lift force.

2.3 **Quasi-Steady Aerodynamic Theory of Flapping Flight**

Recent experimental and computational studies on insect flight have revealed that the unsteady aerodynamic force of flapping wing can be well approximated by quasi-steady aerodynamic model[5; 12; 18; 22; 25]. The quasi-steady theory of flapping wing aerodynamics is formulated based on conventional steady airfoil theory and the well-established blade element method that is widely used in the aerodynamic analysis of rotorcraft for its simple and explicit form. Ellington[30] explained the basic formulation and presented the preliminary results in detail. Later Dickinson et al.[5; 18; 25] experimentally measured a scaled mechanical model of Fruit fly (*Drosophila melanogaster*) wing immersed in a tank of mineral oil, and analysed the aerodynamic forces using quasi-steady model. In this work, the aerodynamic forces of the model fruit fly wing are separated by translational force, rotational force and added mass force, and the corresponding force coefficients are studied empirically.

2.3.1 **Fluid force due to translation**

The kinematics of the model fruit fly wing used by Dickinson et al.[5; 18; 25] is described by a triangular waveform of the angular position of the wing within the stroke plane and a trapezoidal wave function of the angle of attack, the Reynolds number is around 100. The formula that is used to estimate the magnitude of the added mass force is written as:

$$F_{a,N} = \rho \frac{\pi}{4} R^2 \bar{c}^2 \left(\ddot{\phi} sin\alpha + \dot{\phi}\dot{\alpha} cos\alpha\right) \int_0^1 \hat{r}\hat{c}^2(\hat{r}) d\hat{r} - \ddot{\alpha}\rho \frac{\pi}{16} \bar{c}^3 R \int_0^1 \hat{c}^2(\hat{r}) d\hat{r} \qquad \textbf{(2-3)}$$

where ρ is the fluid density, R is the wing length, $\bar{c}$ is the mean chord length, $\hat{r}$ and $\hat{c}(\hat{r})$ are the non-dimensional radial position along the wing and non-dimensional chord length, respectively, ϕ is the angular position of the wing and α is the angle of attack. This formula is an approximation of the solution of basic two-dimensional flat plate that moves in potential flow and integrated along the span through a standard blade element method. The original problem was solved by Sedov[31]. By subtracting the added mass force from the total aerodynamic force, they approximated the lift and drag coefficient of the wing in translation by the following equations:

$$C_L = 0.225 + 1.58\,sin(2.13\alpha - 7.2) \quad \textbf{(2-4)}$$

and

$$C_D = 1.92 - 1.55cos(2.04\alpha - 9.82) \quad \textbf{(2-5)}$$

Where α is the angle of attack in degree. Wang et al.[32] in a subsequent investigation used a 2D CFD computation in comparison with the above 3D experimental results, and gave an alternative fit of the lift and drag coefficient based on 2D CFD results:

$$C_L = 1.2sin(2\alpha) \quad \textbf{(2-6)}$$

$$C_D = 1.4 - cos(2\alpha) \quad \textbf{(2-7)}$$

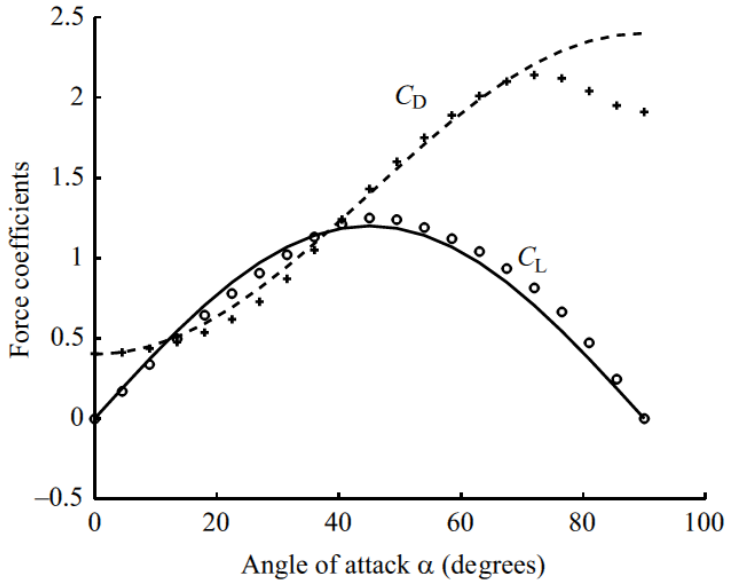

Figure 2-13 Quasi-steady lift C_L (circles) and drag C_D (crosses) coefficients measured from 2D CFD computation (equations (2-6), (2-7)) compared to the empirical function described by equations (2-4), (2-5) (solid and broken lines, respectively) (Reproduced from[32]).

An observation is also presented that the coefficients, unlike the Kutta–Joukowski lift, which is valid at small values of α and is proportional to $sin\alpha$, are valid for all values of α and depend explicitly on 2α, rather than α[32]. An equivalent interpretation is found in Usherwood and Ellington[22] that the

dominate force for flapping or revolving wings in low Reynolds number (Re~10^3) during translation is the pressure force which acts normal to the wing surface and is proportional to $sin\alpha$, i.e.:

$$C_N = C_{Nmax} sin(\alpha) \quad \textbf{(2-8)}$$

This equation will give the $sin2\alpha$ relationship by a simple rotation from the wing frame to the lift and drag frame. The aerodynamic mechanism behind this relationship is that during translation, the leading-edge vortices are a result of leading-edge separation and so are directly associated with a loss of leading-edge suction, therefore, the high vertical (or lift) forces due to leading-edge vortices must inevitably result in high horizontal (or drag) forces[22; 33].

2.3.2 **Fluid force due to wing rotation**

The fundamental theory for the unsteady aerodynamics of a pitching airfoil was derived based on potential flow theory. The early work of Theodorsen[34], Sedov[31], and Fung[35] gives the formula that calculates the aerodynamic force acting on a pitching 2D flat plate in potential flow and undergoing small sinusoidal motion is written as:

$$F_{rot} = \rho U_\infty \pi (0.75 - \hat{x}_0) \omega c^2 \quad \textbf{(2-9)}$$

Where $\hat{x}_0$ is the non-dimensional location of the rotational axis, ω is the rotation rate of the flat plate, and c is the chord length. By applying the impermeability boundary condition, which requires that no fluid travels across the surface of the wing, and the Kutta condition, which requires that the vorticity generated by the trailing edge of the wing must equal to zero[34; 35], the circulation due to wing rotation is derived as:

$$\Gamma_{rot} = \pi (0.75 - \hat{x}_0) \omega c^2 = C_{rot} \omega c^2 \quad \textbf{(2-10)}$$

Where C_{rot} is the coefficient of rotational circulation, which varies linearly with $\hat{x}_0$ [25]. Sane and Dickinson[25] experimentally measured the C_{rot} of a dynamically scaled mechanical model of fruit fly (*Drosophila Melanogaster*)

wing and found that the coefficient varies with the change of the rotation rate of the wing as well as the location of the rotational axis (see Figure 2-14, below).

These experimental results match the theoretical prediction that the rotational circulation decays as the axis of rotation is moved toward the trailing edge, and changes sign at approximately three-quarters of the chord length from the leading edge of the wing[5; 25]. While due to the separation of the flow, the Kutta condition cannot be satisfied, therefore, the theoretical value fail to explain the variation of C_{rot} with the change of $\hat{\omega}$.

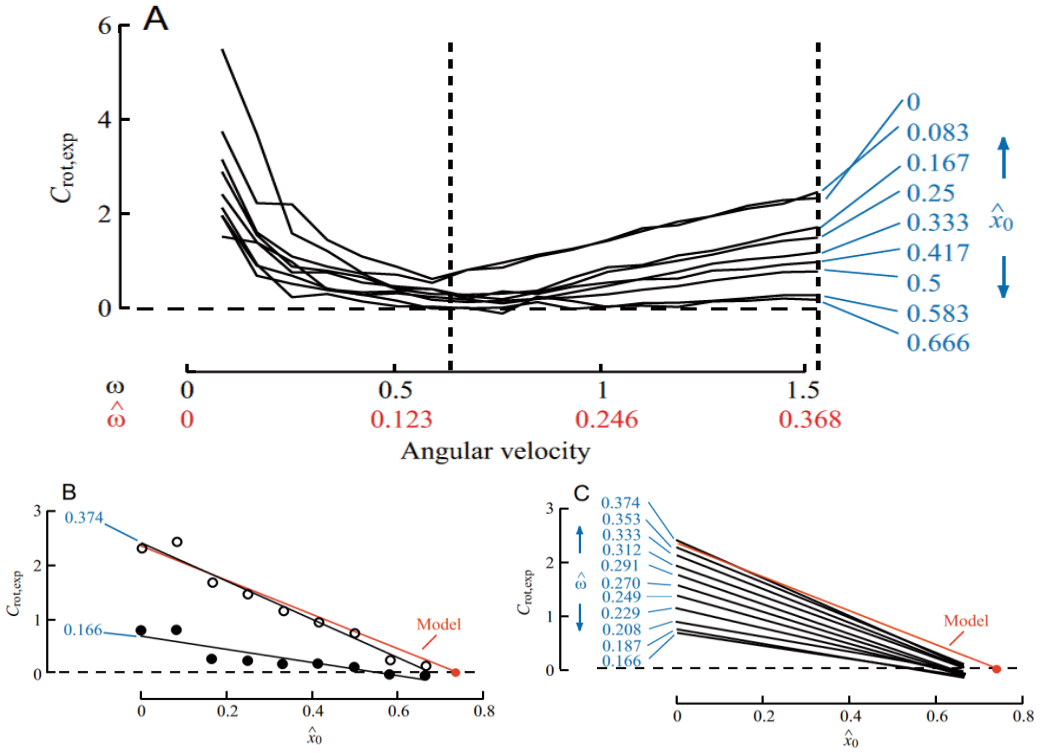

Figure 2-14 Variation in rotational coefficient C_{rot} with angular velocity and axis of rotation. (A) Rotational coefficients versus angular velocity ($\omega, rads^{-1}$) for each axis of rotation. (B) Rotational coefficient versus axis of rotation ($\hat{x}_0$) and non-dimensional angular velocity of wing rotation ($\hat{\omega} = \omega\bar{c}/U_t$). (C) A series of regression lines for representative values of angular velocity plotted together with the quasi-steady prediction (Reproduced from[25]).

2.3.3 **Induced downwash velocity of insect flight**

It should be noted that for a flying insect (as well as a rotorcraft), the instantaneous aerodynamic force is affected by the history of the shed vorticity. In fact, the summation of the whole wake of the wing generates a 'downwash' in the flow field, which changes the direction of the relative velocity with respect to the wing, and therefore, changes the instantaneous angle of attack. The downwash velocity (also called 'induced velocity') of the flow will induce a drag to the airfoil, which, together with the profile drag due to the viscosity of the flow, decides the energy cost for flight. Ellington[36] used a *Rankine-Froude momentum theory* combined with a *vortex theory* to analysis the downwash induced by the wake of insect flapping wing. In the simple *Rankine-Froude theory*, the wake is considered as a steady jet with a uniform axial velocity across any cross-sectional area[36; 37]. By applying Bernoulli's principle, the theory shows that the velocity at far-field wake equals to twice the induced velocity at the actuator disc[36; 37], i.e.:

$$\omega = 2\omega_0 \tag{2-11}$$

Therefore, apply Newton's second law for the fluid across the actuator disc gives the force required to generate a steady flow of velocity ω as:

$$F = \rho\omega^2 A \tag{2-12}$$

Where A is the area of the actuator disc. Through an elaborate analysis of the vorticity shedding of the insect wing, Ellington[36] showed that the area of the actuator disc for a hovering insect shall equal to the projection of the area swept by the wing onto the horizontal plane, i.e.:

$$A = \Phi R^2 cos(\beta) \tag{2-13}$$

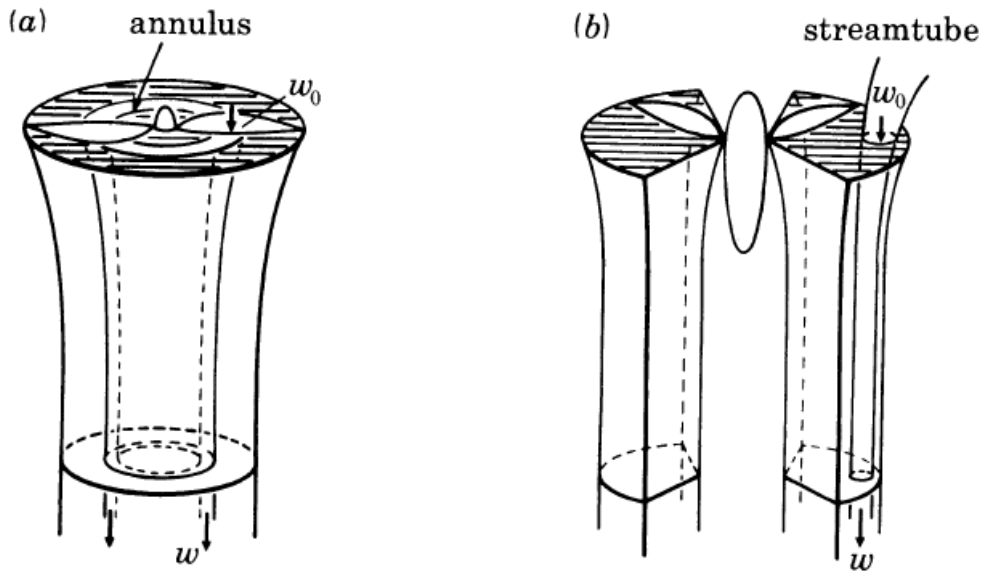

Figure 2-15 The idealized wake flow of the axial momentum theory for hovering rotor in (a) and for hovering insects in (b). The actuator disc is represented by the shaded area (Reproduced from[36]).

Where Φ is the stroke amplitude, R is the wing span, and β is the stroke plane deviation angle. Usherwood and Ellington[22] used the momentum theory to analysis a revolving hawkmoth (*Manduca Sexta*) wing, by differentiating the force coefficients of the 'early' (between 60° and 120° from the start of revolution) and 'steady' (between 180° and 450° from the start of revolution) coefficient. The 'early' coefficients are used to approximate the 'real' coefficient without the downwash flow for the induced downwash of the propeller wake has hardly begun in this period[22]. In this case, since the revolving wing is in fact a propeller, except that it is an insect wing (model) and works in low Reynolds number (Re~10^3), the induced velocity is tackled through a standard *Rankine-Froude theory*, and the induced velocity on each wing section is easily derived by assuming a triangular distribution along the wing span:

$$w_0 = k_{ind}\frac{r}{R^2}\sqrt{\frac{F_v}{\rho\pi}} \qquad \textbf{(2-14)}$$

Where k_{ind} is the correction factor accounting for non-uniform downwash distributions[22; 37]. Birch and Dickinson[38] used two-dimensional digital particle image velocimetry (DPIV) to visualize flow patterns around a

dynamically scaled model fruit fly wing (Re~100). Their results show that the structure of the flow within the wake at mid-stroke consists of a relatively constant unidirectional downward flow below the wing (though pulsatile)[38]. Thus, the flow pattern fulfils the basic assumptions for the classical *Rankine-Froude momentum theory*, and the induced velocity of the downwash flow for flapping wing can be tackled through the method stated above.

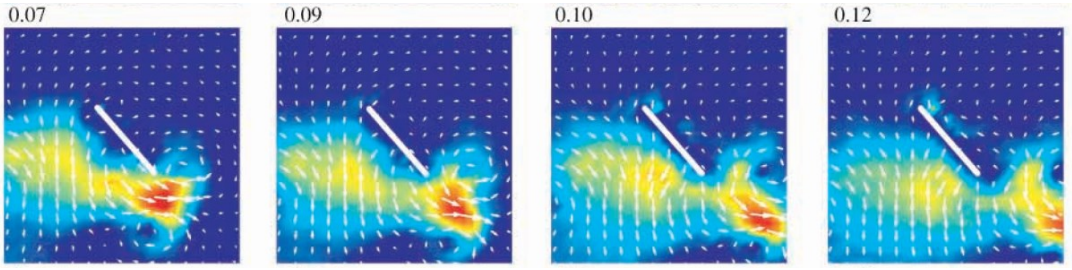

Figure 2-16 Subtractive reconstruction of wake velocity fields using DPIV. Pseudocolor represents the magnitude of the velocity difference; arrows indicate direction and magnitude of flow. The flow within the wake at mid-stroke consists of a relatively constant unidirectional downward flow below the wing (Reproduced from[38]).

2.3.4 **Quasi-steady model applied to insect flight**

Due to the efficiency of implementation, the quasi-steady aerodynamic model is widely used by previous researchers for the investigation of insect flight and engineering design. Berman and Wang[39] used an optimization algorithm to find the most energy-efficient flapping motion for hovering flight of insects based on a quasi-steady aerodynamic model. The power consumption was assumed to have no elastic storage effect, which means that only positive power of the dynamic system was taken into account (which is reasonable for the effect of elastic storage for a flying insect is approximately on the order of 10%[40]). The quasi-steady aerodynamic model that is used in this investigation differs slightly from that was mentioned above, the total circulation of a 2D wing section is written as:

$$\Gamma = -\frac{1}{2}C_T c(r)|\mathbf{v}|sin(2\alpha) + \frac{1}{2}C_R c^2(r)\dot{\eta} \qquad \textbf{(2-15)}$$

Where α is the angle of attack, C_T and C_R are the translational and rotational lift coefficients respectively. The viscous force of the wing section is approximated by:

$$\mathbf{F^v} = \frac{1}{2}\rho_f c(r)\left[C_D(0)cos^2(\alpha) + C_D\left(\frac{\pi}{2}\right)sin^2(\alpha)\right]|\mathbf{v}|\langle \mathbf{v_{x'}}, \mathbf{v_{y'}}\rangle dr \quad \textbf{(2-16)}$$

Where $C_D(\alpha)$ is the wing's drag coefficient as a function of the angle of attack. The above equation is written in vector form, $\langle \mathbf{v_{x'}}, \mathbf{v_{y'}}\rangle$ indicates the scalar product of the velocity vector of the wing in the wing-fixed frame. The values for C_T, $C_D(0)$ and $C_D\left(\frac{\pi}{2}\right)$ for different insects are taken from model flapping wing experiments (Dickinson et al.[18], Usherwood and Ellington[22], and Dudley and Ellington[41]). The total mechanical power of the hovering insect wing is obtained by direct multiplication of the angular velocity vector of the wing with the force vector of the wing in the wing-fixed frame, the ith component of the mechanical power at time step t is expressed as:

$$P_i(t) = \Omega_i\left[I_i\dot{\Omega}_i - \Omega_j\Omega_k\left(I_j - I_k\right) - \tau_i^{aero}\right] \quad \textbf{(2-17)}$$

Where (i, j, k) is a cyclic permutation of the Euler angle (ϕ, α, η), τ^{aero} is the aerodynamic torque, I_i is the moment of inertia when rotating in i, and Ω_i is the angular velocity in the corresponding coordinate[39]. In the above equation, the first two terms are the mechanical power due to the inertial of the wing mass, and third term is the mechanical power due to the aerodynamic forces.

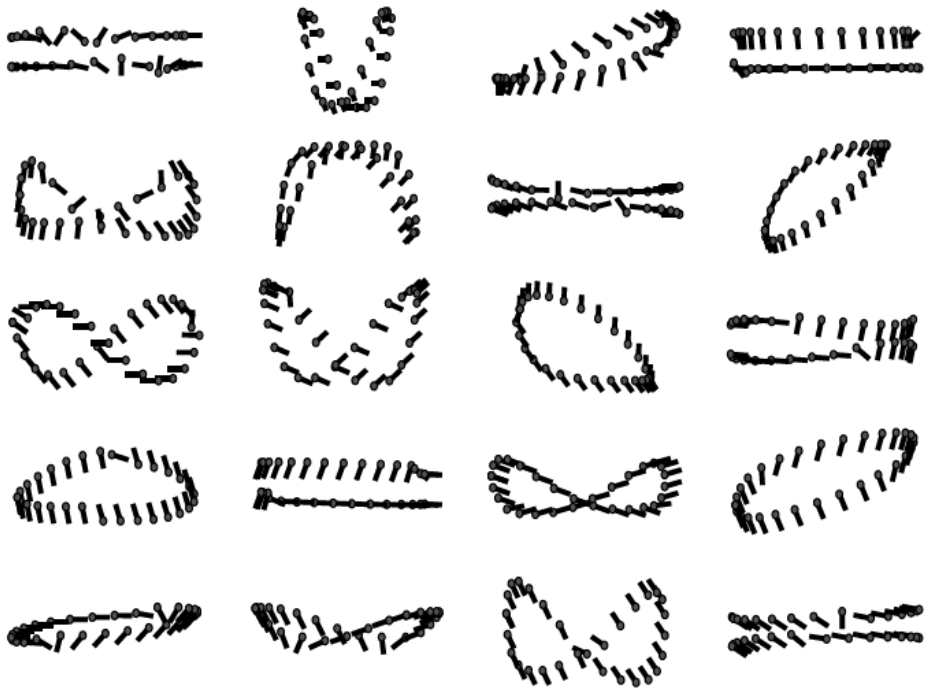

Figure 2-17 Optimization of various kinematics of insect flight. The lines represent a wing chord cross-section, and the dots are placed on the same edge of the wing throughout the stroke (Reproduced from[39]).

Whitney and Wood[42] used a quasi-steady aerodynamic model combined with rigid body dynamics to study the passive rotation of a fabricated flapping insect wing. The quasi-steady model presented in their study has no significant difference compared with those stated above, rather, their work indicates that the quasi-steady aerodynamic model can serve as a first hand tool for the analysis of coupling between structure deformation and aerodynamic forces of flapping wing.

As stated at the beginning of this chapter, the quasi-steady theory for flapping wing aerodynamics is based on conventional steady airfoil theory, and is an approximation to the time-dependent forces of flapping wing, therefore, it fails to account for the unsteady aerodynamic effects, in particular, the Wagner effect, which results in the phase shift of the instantaneous aerodynamic forces[4; 25], and therefore, shall have strong implication on the power consumption (for the instantaneous aerodynamic power equals to the multiplication of the instantaneous velocity and drag of the wing). However, former investigation

shows that at Re~10^3, the Wagner effect appear to exert only a minor influence on force generation[43]. As claimed by Usherwood and Ellington[22] 'The significance of unsteady mechanisms may be more limited to the control and manoeuvrability of flight than recently thought, steady-state coefficients may go much of the way towards accounting for the lift and power requirements of hovering and, while missing unsteady aspects, present the best opportunity for analysing power requirements in those insects, and those flight sequences, in which fine kinematic details are unknown.'.

3 AERODYNAMIC MODELLING OF FWR

3.1 Introduction

The FWR concept combines insect-like flapping wing and the man-made rotary mechanism, which uses the gyration of the wing with respect to the wing root to create the relative velocity to the surrounding air. The air velocity enhances the aerodynamic lift generated by the flapping wings. The kinematics of the FWR wing can be described by a vertical flapping motion and a horizontal rotating motion. While the aerodynamic performance of insect flapping wing and micro rotorcraft have been extensively studied [7; 12; 18; 25; 39]. This FWR MAV is in its infant age and has yet limited understanding in aerodynamic performance and potentials. More specifically, the aerodynamic force variation with the kinematic parameters and the energy efficiency of FWR, in comparison with insects and rotorcraft, are worth studying.

The quasi-steady aerodynamic theory for flapping wing has been elaborately reviewed in the second chapter, and will be used for the current study. In the following chapter, we formulated the quasi-steady aerodynamic model of FWR based on previous studies of insect flapping wing. To correctly seize the aerodynamic force and torque production, we considered the quasi-steady term (due to the LEV), the rotational force term (due to the rotational circulation) and the added mass term (due to added mass inertia) for the aerodynamic force calculation. The dimensionless parameters for the production of the aerodynamic force and power consumption of the FWR are further analysed. As a first step study, the problems addressed in our analyses serve as the basis toward further understanding of the unsteady aerodynamics of the FWR configuration and engineering design of such a MAV.

3.2 Coordinate Definition and Kinematics of the FWR

The coordinate systems that are used to describe the motion of the wing for the FWR are shown in Figure 3-1 A. The body of a FWR is depicted in the figure; the wing is shown detached for clarity. The inertial frame $(\mathrm{x}, \mathrm{y}, \mathrm{z})$ is attached to the body with the origin o at the wing root; the wing-fixed frame $(\mathrm{x_w}, \mathrm{y_w}, \mathrm{z_w})$ is

attached to the wing root with the same origin o (shown on the detached wing for clarity). The rotation plane is assumed to be horizontal. The rotation, flapping, and pitching degree of freedom of the FWR wing are described by the angle ψ, ϕ, and α, respectively (see Figure 3-2, note that ψ and α are depicted negative and ϕ is depicted positive). The motion of the wing is described by successive rotation about the y, x′, and z_w axis with the corresponding Euler angles. The planar view of each dimension describing the corresponding Euler angles is shown in Figure 3-1 B.

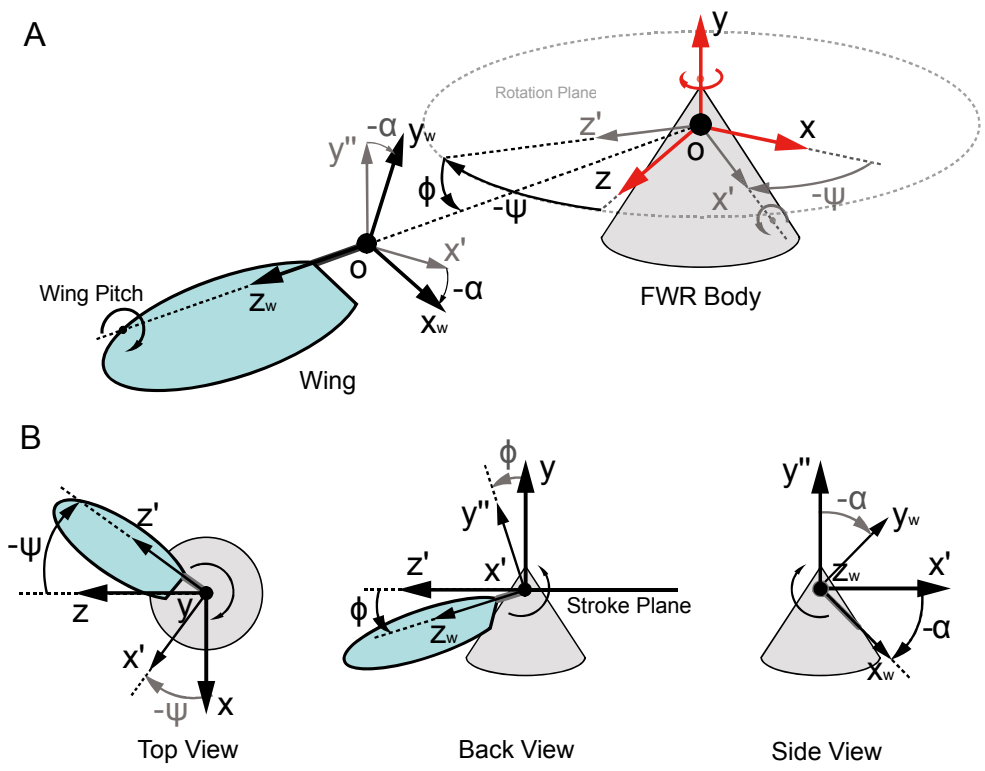

Figure 3-1 (a) Coordinate system definition and Euler angles for specifying the wing motion. (b) The top, back, and side view of the Euler angles for the FWR wing.

In Fig. 3-1(a), the coordinate systems include the inertial frame $(\boldsymbol{x}, \boldsymbol{y}, \boldsymbol{z})$ (red arrow), the wing-fixed frame $(\boldsymbol{x_w}, \boldsymbol{y_w}, \boldsymbol{z_w})$ (black arrows), and the intermediate frame of the Euler rotations $(\boldsymbol{x'}, \boldsymbol{y'}, \boldsymbol{z'})$ and $(\boldsymbol{x''}, \boldsymbol{y''}, \boldsymbol{z''})$ (grey arrows). All of the coordinate systems share the origin $\boldsymbol{O}$ at the wing root. For clarity, the overlapping axes of the intermediate frames ($\boldsymbol{y'}$, $\boldsymbol{x''}$, and $\boldsymbol{z''}$) are omitted. The rotation, flapping, and pitching degree of freedom of the FWR wing are

described by the angle $\boldsymbol{\psi}$, $\boldsymbol{\phi}$, and $\boldsymbol{\alpha}$, respectively. As shown in Fig. 3-1(a), the wing successively rotates about the $\boldsymbol{y}$, $\boldsymbol{x'}$, and $\boldsymbol{z_w}$ axis with the rotation angle $\boldsymbol{\psi}$, the flapping stroke angle $\boldsymbol{\phi}$, and the pitch angle $\boldsymbol{\alpha}$ (positive anticlockwise) to reach the ultimate position, the angular velocity and acceleration of the wing can be specified by giving the rate of change of the above Euler angles.

By the above definition, the angular velocity vector of the FWR wing in the inertial frame can be expressed by the time derivative of the three Euler angles $\dot{\psi}$, $\dot{\phi}$, and $\dot{\alpha}$ and the transformation matrixes:

$$\boldsymbol{\omega_i} = \left(\omega_{i,x}, \omega_{i,y}, \omega_{i,z}\right) = \begin{bmatrix} 0 \\ \dot{\psi} \\ 0 \end{bmatrix} + \mathbf{R}(\psi) \begin{bmatrix} \dot{\phi} \\ 0 \\ 0 \end{bmatrix} + \mathbf{R}(\psi)\mathbf{R}(\phi) \begin{bmatrix} 0 \\ 0 \\ \dot{\alpha} \end{bmatrix} \tag{3-1}$$

In which, $\mathbf{R}(\psi)$ and $\mathbf{R}(\phi)$are the rotation matrices of the corresponding Euler angles. By combining the three elementary rotation matrixes, the transformation matrix from inertial frame to the wing-fixed frame is given as:

$$\mathbf{R_{i\rightarrow w}} = \mathbf{R^T}(\alpha)\mathbf{R^T}(\phi)\mathbf{R^T}(\psi) \tag{3-2}$$

Where the transformation matrices are written as:

$$\mathbf{R}(\psi) = \begin{bmatrix} cos\psi & 0 & -sin\psi \\ 0 & 1 & 0 \\ sin\psi & 0 & cos\psi \end{bmatrix} \tag{3-3}$$

$$\mathbf{R}(\phi) = \begin{bmatrix} 1 & 0 & 0 \\ 0 & cos\phi & sin\phi \\ 0 & -sin\phi & cos\phi \end{bmatrix} \tag{3-4}$$

and

$$\mathbf{R}(\alpha) = \begin{bmatrix} cos\alpha & -sin\alpha & 0 \\ sin\alpha & cos\alpha & 0 \\ 0 & 0 & 1 \end{bmatrix} \tag{3-5}$$

The angular acceleration vector in the inertial frame $\dot{\boldsymbol{\omega}}_\mathbf{i}$ can be derived by directly differentiating the equation (3-1) above. Equation (3-1) can be written down by the explicit form:

$$\boldsymbol{\omega_i} = \left(cos\psi sin\phi\dot{\alpha} - sin\psi\dot{\phi}\right)\mathbf{e_{x,i}} + \left(sin\psi sin\phi\dot{\alpha} + cos\psi\dot{\alpha}\right)\mathbf{e_{y,i}} + \left(cos\phi\dot{\alpha} + \dot{\psi}\right)\mathbf{e_{z,i}} \quad \textbf{(3-6)}$$

Therefore, the corresponding angular acceleration expressed in the inertial frame can be derived by differentiating the above equation, which is written as:

$$\dot{\omega}_{x,i} = -sin\psi sin\phi\dot{\psi}\dot{\alpha} + cos\psi cos\phi\dot{\phi}\dot{\alpha} + cos\psi sin\phi\ddot{\alpha} - cos\psi\dot{\psi}\dot{\phi} - sin\psi\ddot{\phi} \quad \textbf{(3-7)}$$

$$\dot{\omega}_{y,i} = cos\psi sin\phi\dot{\psi}\dot{\alpha} + sin\psi cos\phi\dot{\phi}\dot{\alpha} + sin\psi sin\phi\ddot{\alpha} - sin\psi\dot{\psi}\dot{\phi} + cos\psi\ddot{\phi} \quad \textbf{(3-8)}$$

and

$$\dot{\omega}_{z,i} = -sin\phi\dot{\alpha} + cos\phi\ddot{\alpha} + \ddot{\psi} \quad \textbf{(3-9)}$$

Where the vectors $\mathbf{e_{x,i}}, \mathbf{e_{y,i}}, \mathbf{e_{z,i}}$ represents the basis vector of the inertial coordinate system, and $\omega_{x,i}$, $\omega_{y,i}$, and $\omega_{z,i}$ represents the components of the angular velocity in the inertial frame. The angular velocity and acceleration vector in the wing-fixed frame is obtained by applying the above transformation (see equation (3-2) above). For blade element analysis, it is convenient to write down the velocity and acceleration vector of the wing hinge (z_w axis) at span-wise location r with respect to the wing root O due to the gyration of the wing, since the hinge has no radial velocity and acceleration components, the resultant velocity and acceleration vector in the wing-fixed frame is directly 2D vectors (in the (x_w, y_w) plane):

$$\mathbf{U(r)} = \boldsymbol{\omega} \times \mathbf{r} = \omega_y r\mathbf{e_x} - \omega_x r\mathbf{e_y} = \left(u_x, u_y\right) \quad \textbf{(3-10)}$$

$$\dot{\mathbf{U}}\mathbf{(r)} = \dot{\boldsymbol{\omega}} \times \mathbf{r} + \boldsymbol{\omega} \times (\boldsymbol{\omega} \times \mathbf{r}) = \left(\dot{\omega}_y + \omega_x\omega_z\right)r\mathbf{e_x} + \left(-\dot{\omega}_x + \omega_y\omega_z\right)r\mathbf{e_y} = \left(\dot{u}_x, \dot{u}_y\right) \quad \textbf{(3-11)}$$

where $\mathbf{e_x}$, $\mathbf{e_y}$ represent the basis vector of the wing-fixed coordinate system of the 2D wing section; $\boldsymbol{\omega}$ denote the rotation rate of the wing in the wing-fixed coordinate system, which has ω_x, ω_y and ω_z components in the x_w, y_w and z_w axes, respectively; $\mathbf{U}(\mathbf{r})$ and $\dot{\mathbf{U}}(\mathbf{r})$ refers to the velocity and acceleration vector of the wing hinge at span-wise location r; u_x, u_y, $\dot{u}_x$ and $\dot{u}_y$ is used to represent the components of velocity and acceleration in x_w and y_w axes, respectively (note that $\dot{u}_x$ and $\dot{u}_y$ represent the acceleration components, not the time derivatives of u_x and u_y). Since we used the wing-fixed coordinate system for the velocity and acceleration expression, the effective angle of attack (AoA) of the wing can be easily found by inverse trigonometric function of the velocity components ratio of the wing:

$$\alpha_e = arctan(u_y/u_x) \tag{3-12}$$

The key feature of the FWR wing kinematics is the coupled flapping and rotation motion and the asymmetric pitching at up and downstroke (see Figure 3-2 below). In these degrees of freedom, the definition of a specific function to describe the wing motion varies, however, major properties of the aerodynamic performance can be seized by using simple periodic kinematic functions. In insect flight, simple harmonic function (SHF) is used to describe the flapping motion[44], which is also the kinematic pattern of most mechanical systems at resonant state. Here, we simply use constant rotating speed and sinusoidal flapping and pitching to describe the wing motion of FWR. The kinematics of the wing is specified by giving the variation function of the three Euler angles with respect to time t. The variation of the three Euler angles can be expressed by the following equations:

$$\psi = \psi_0 t \tag{3-13}$$

$$\phi = \Delta\Phi sin(2\pi f t) \tag{3-14}$$

$$\alpha = \Delta\alpha sin\left(2\pi f t + \frac{\pi}{2}\right) + \alpha_0 \tag{3-15}$$

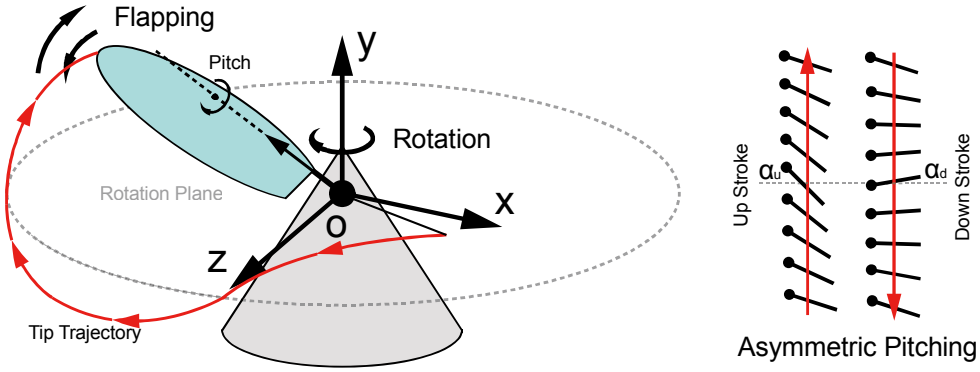

Figure 3-2 Kinematic pattern of the FWR wing. The FWR has rotation, flapping, and pitching degree of freedom, the tip trajectory of the wing shows the coupled flapping and rotation motion (red curves). Similar with dragon fly, the wing has asymmetric pitching at upstroke and downstroke, α_u and α_d represent he geometric AoA of the wing at mid-upstroke, respectively.

where $\psi_0$is the rotation speed, f is the flapping frequency, $\Delta\Phi$ is the flapping amplitude, $\Delta\alpha$ is the pitching amplitude, for modelling the asymmetric pitching, the angle α_0 is introduced. By this definition, the geometric AoA of the wing at mid-upstroke α_u and mid-downstroke α_d is given as:

$$\begin{cases}\alpha_u = \alpha_0 - \Delta\alpha \\ \alpha_d = \alpha_0 + \Delta\alpha\end{cases} \quad \textbf{(3-16)}$$

Thus, the kinematics of the FWR wing can be specified by 5 parameters: the rotation speed ψ_0, the flapping frequency f, the flapping amplitude $\Delta\Phi$, the up and downstroke AoA at mid-stroke α_u and α_d.

3.3 **Wing Geometry**

The geometry of the FWR wing is modelled by keeping the morphological parameters of quasi-static analysis similar with available insect data. Specifically, the wing aspect ratio AR is within 3~5; the shape parameters, including the first, second and third radius of non-dimensional moment of wing area $\hat{\mathrm{r}}_1(\mathrm{S})$, $\hat{\mathrm{r}}_2(\mathrm{S})$ and $\hat{\mathrm{r}}_3(\mathrm{S})$ ($\hat{r}_k^k(\mathrm{S}) = 2\int_0^R cr^k dr/SR^k$, where S is the total area of the wing pair, and R is the wingspan) are within the numbers 0.45~0.55, 0.5~0.6 and 0.55~0.65, respectively[45]. For simplicity, we used a thin flat plate of

elliptical shape, with chord-wise cutting edge near the wing root 0 (origin of gyration). The shape and definition of geometric parameters of the wing are shown in Figure 3-3. The detailed parameters of the wing geometry are calculated and given as follow:

$$AR = 3.6,\ \ \hat{r}_1(S) = 0.55,\ \ \hat{r}_2(S) = 0.59,\ \ \hat{r}_3(S) = 0.63$$

The wing span R is set to keep the required Reynolds number of flight, in accordance with the wing kinematic parameters. For the calculation of the rotational force, added mass force and pitching torque, it is convenient to use the local coordinate of the semi-chord h (see Figure 3-3 below) to specify the location of the pitching axis with respect to leading edge (LE) x_{pitch}:

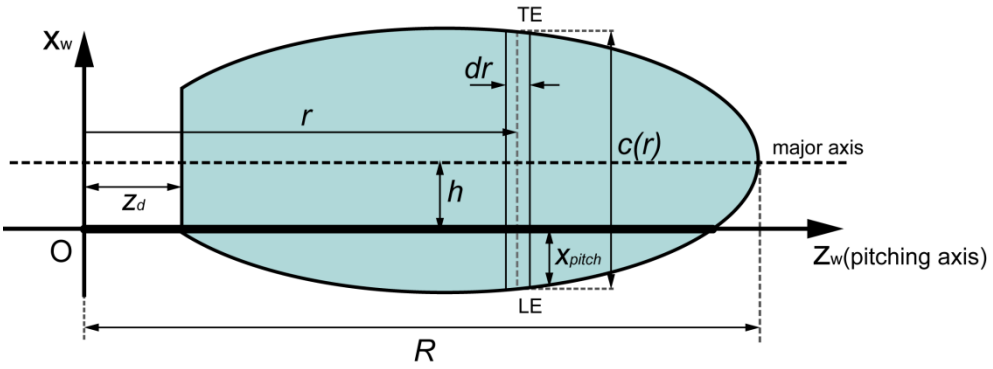

Figure 3-3 Shape and geometric parameters definition of the FWR wing.

The wing has span length $\boldsymbol{R}$ and root cut $\boldsymbol{z_d}$; the pitching axis of the wing ($\boldsymbol{z_w}$) is located near the leading edge; a 2D wing strip with infinite small width $\mathbf{d}\boldsymbol{r}$ and chord length $\boldsymbol{c(r)}$ is shown at span-wise location $\boldsymbol{r}$ (with respect to the wing root $\boldsymbol{O}$); the LE of the 2D wing section has distance $\boldsymbol{x_{pitch}}$ from the pitching axis $\boldsymbol{z_w}$; $\boldsymbol{h}$ refers to the coordinate of the major axis (semi-chord in each 2D wing section) of the ellipse in $\boldsymbol{x_w}$ axis.

$$x_{pitch} = \left(\frac{1}{2} - \hat{h}\right) c(r) \qquad \textbf{(3-17)}$$

where $\hat{h}$ is the non-dimensional local coordinate of the semi-chord: $\hat{h} = \frac{h}{c(r)}$. For insect flapping wing, the pitching axis is usually considered constantly located at around 0.25 chord length along the span[25; 46], corresponding to $\hat{h} = 0.25$. In

our analysis, we also used this constant number for the forces and torque calculation.

3.4 **Aerodynamic Model**

3.4.1 **Two-dimensional section force**

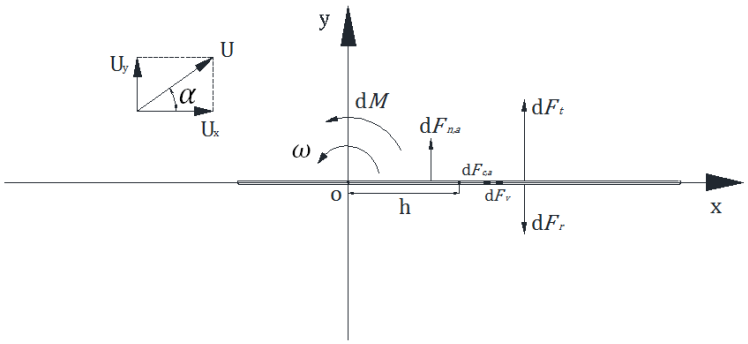

Figure 3-4 Forces and Moments on two-dimensional wing section.

The air velocity vector is $\mathbf{U} = (\boldsymbol{U_x}, \boldsymbol{U_y})$. The 2D plate has angular velocity $\boldsymbol{\omega}$, the rotation-axis locates at origin of the coordinate system $\mathbf{o}$. The semichord of the wing section has coordinate $(\boldsymbol{h}, \mathbf{0})$.

The coordinate system for the two-dimensional wing section is shown in Figure 3-4, which is fixed on the 2D wing section. The standard 2D airfoil theory tells us that the aerodynamic forces acting on a 2D flat plate equals to the dynamic pressure multiply by the force coefficients (lift coefficient and drag coefficient) and the reference length (chord length). In quasi-steady theory of flapping wing, this relationship holds, except that the force vector acts perpendicular to the wing chord[22; 32]. Dickinson et al.[5; 18; 25] divided the quasi-steady force by translational force, rotational force and virtual mass force, and experimentally measured the corresponding coefficients. Here, we will use this definition. The corresponding equations for translational force and rotational force are written as:

$$\mathbf{dF_t} = \frac{1}{2}\rho\|\mathbf{U(r)}\|^2\mathbf{C_t}(\boldsymbol{\alpha_e})c(r)dr \qquad \textbf{(3-18)}$$

and

$$\mathbf{dF_r} = -C_{rot}\rho\|\mathbf{U(r)}\|\omega_z c(r)^2 dr\mathbf{e_y} \tag{3-19}$$

where $\mathbf{e_x}, \mathbf{e_y}$ represents the basis vector of the 2D wing-fixed coordinate system, ρ is the density of the surrounding air, and $c(r)$ represents the (local) chord length. The quasi-steady force coefficient ($\mathbf{C_t}$, for brevity, we omitted the variable α_e) can be treated as a unit force vector acting on the wing, and therefore, its expression is coordinate dependent. Figure 3-5 shows the coordinate systems and the expression of the vector $\mathbf{C_t}$ in the lift and drag frame (x, y) and the wing-fixed frame (x_w, y_w), respectively. In the lift and drag frame, the force coefficients of the airfoil (C_d, C_l) are obtained from empirical fit of the lift and drag forces of previous studies on insect flapping wing, and can be approximated by the following equations[32; 42]:

$$\begin{cases} C_l = C_{Lmax} sin(2\alpha_e) \\ C_d = \left(\frac{C_{Dmax}+C_{D0}}{2}\right) - \left(\frac{C_{Dmax}-C_{D0}}{2}\right) cos(2\alpha_e) \end{cases} \tag{3-20}$$

Where the quasi-steady coefficients C_{Lmax}, C_{Dmax}, C_{D0} together with the rotational force coefficient C_{rot} are obtained from empirical studies at similar Reynolds number[18; 22; 25]. Therefore, the translational force coefficient in the wing-fixed frame $\mathbf{C_t} = (C_H, C_V)$ (see Figure 3-5) can be obtained from the force coefficients in the lift and drag frame by simple rotation:

$$\begin{pmatrix} C_H \\ C_V \end{pmatrix} = \mathbf{R}(\boldsymbol{\alpha_e}) \begin{pmatrix} C_d \\ C_l \end{pmatrix} \tag{3-21}$$

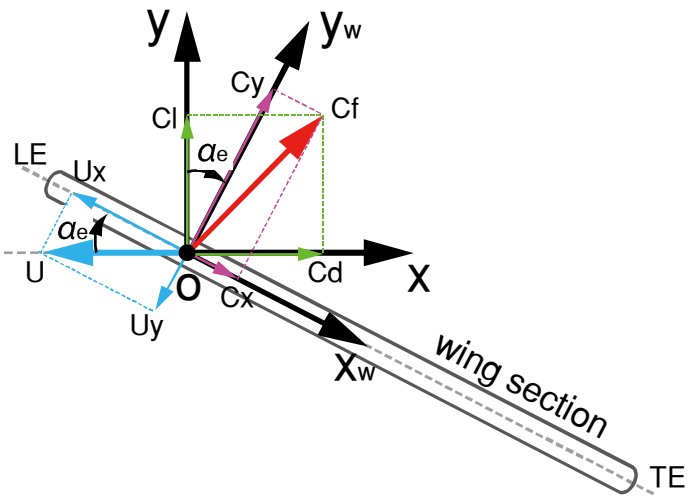

Figure 3-5 Coordinate systems and vector expressions of a 2D wing section.

The 2D lift and drag frame $(\boldsymbol{x}, \boldsymbol{y})$ and wing-fixed frame $(\boldsymbol{x_w}, \boldsymbol{y_w})$ are shown in the figure, with origin $\boldsymbol{O}$ at pitching axis. Blue arrow and Red arrow indicate the velocity vector $(\mathbf{U})$ and unit force vector $(\mathbf{C_t})$ of the 2D wing section, respectively. The components of velocity vector in the wing-fixed frame $\boldsymbol{u_x}$, $\boldsymbol{u_y}$ (blue arrows), the components of aerodynamic force vector in the wing-fixed frame $\boldsymbol{C_H}$, $\boldsymbol{C_V}$ (purple arrows), and the components of aerodynamic force vector in the lift and drag frame $\boldsymbol{C_l}$, $\boldsymbol{C_d}$ (green arrows) are shown in the figure. The wing-fixed frame $(\boldsymbol{x_w}, \boldsymbol{y_w})$ is rotated $\boldsymbol{\alpha_e}$ counter-clockwise from the lift and drag frame $(\boldsymbol{x}, \boldsymbol{y})$.

For the calculation of the aerodynamic torque, we need to know the location of the centre of pressure (CP) on the wing. For blade element analysis, the local CP of the 2D wing section $\mathbf{c_p}(\mathbf{r})$ has span-wise location in the z_w axis (in the wing-fixed frame), which is the span-wise location of the wing section r. The chord-wise location of CP x_{cp} is in the x_w axis. Dickson et al.[47] found that the chord-wise location of centre of pressure x_{cp} varies linearly with the change of the effective AoA α_e, the linear relation can be express by the following equation:

$$x_{cp} = \left(\hat{h} + \frac{0.82}{\pi}|\alpha_e| - 0.45\right) c(r) \tag{3-22}$$

Therefore, the 2D aerodynamic torque of the above two forces can be decided by the following equation:

$$dM_q = x_{cp}\left[\frac{1}{2}\rho\|\mathbf{U}(\mathbf{r})\|^2 C_V(\alpha_e)c(r) - C_{rot}\rho\|\mathbf{U}(\mathbf{r})\|\omega_z c(r)^2\right]dr \quad \textbf{(3-23)}$$

The virtual mass force is calculated using Sedov's formula[18], which is suitable for our coordinate definition:

$$\mathbf{dF_{n,a}} = -\left(\lambda_y \dot{u}_y + \lambda_{y\omega}\dot{\omega}_z\right)dr\mathbf{e_y} \quad \textbf{(3-24)}$$

$$\mathbf{dF_{c,a}} = \omega_z\left(\lambda_y u_y + \lambda_{y\omega}\omega_z\right)dr\mathbf{e_x} \quad \textbf{(3-25)}$$

and the torque,

$$dM_a = -\left[\lambda_y u_x u_y + \lambda_{y\omega}\left(\dot{u}_y + u_x\omega_z\right) + \lambda_\omega\dot{\omega}_z\right]dr \quad \textbf{(3-26)}$$

Where $\mathbf{dF_{n,a}}$ acts perpendicular to the plate, and $\mathbf{dF_{c,a}}$ acts parallel to the plate (as indicated by the basis vectors $\mathbf{e_y}$ and $\mathbf{e_x}$). The virtual mass coefficients for the 2D flat plate in potential flow λ_y, $\lambda_{y\omega}$, and λ_ω is given as:

$$\lambda_y = \frac{\pi}{4}\rho c(r)^2 \quad \textbf{(3-27)}$$

$$\lambda_{y\omega} = -\frac{\pi}{4}\rho\hat{h}c(r)^3 \quad \textbf{(3-28)}$$

$$\lambda_\omega = \frac{\pi}{4}\rho\hat{h}^2 c(r)^4 + \frac{\pi}{128}\rho c(r)^4 \quad \textbf{(3-29)}$$

3.4.2 **Three-dimensional forces and moments for hovering flight**

Having resolved the 2D forces and moments, it is easy to see that the 3D forces and moments acting on the flapping wing (and also FWR) can be derived by simply integration along the wingspan. For the case of hovering flight, since the local velocity of the wing varies linearly along the span, therefore, the 3D forces and moments can be write down explicitly. We first define the following integral:

$$I_{jk} = \int_0^R r^j c(r)^k dr \quad \textbf{(3-30)}$$

Where r is the radius of the spanwise position which varies from 0 to R. The integral I_{jk} is defined only by the geometry of the wing, when $\mathrm{j} = 1{,}2,\ \mathrm{k} = 1$, the above integral refers to the first and second moment of the wing area. The non-dimensional form of the above integral can be written as:

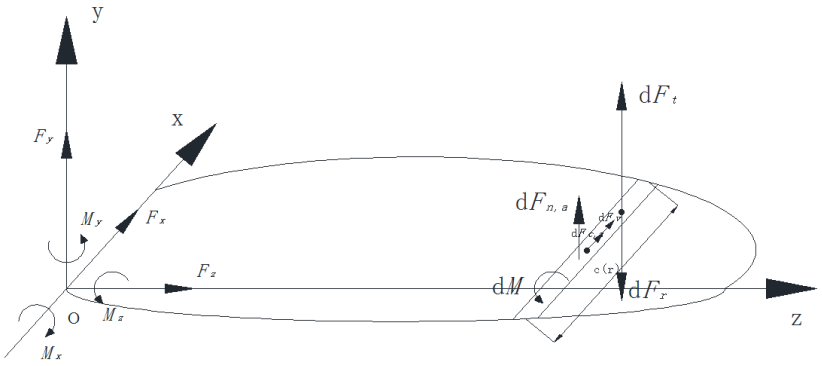

Figure 3-6 Forces and Moments on 3D wing-fixed coordinate system.

The coordinate system definition follows the right-hand-rule. It can be seen that the projection of the force vectors in 3D space onto the 2D $\boldsymbol{x, y}$ plane is identical to the definition shown in Figure 3-4.

$$\hat{I}_{jk} = \frac{1}{R^{j+1}\bar{c}^k}\int_0^R r^j c(r)^k dr \tag{3-31}$$

In the above equation, R refers to the length of the wing span, and $\bar{c}$ refers to the average chord length. If we define the local translational velocity vector of a two-dimensional (2D) wing section at span-wise location r in the wing-fixed coordinate system as $\mathbf{U}(\mathbf{r}) = (u_x, u_y) = \boldsymbol{\Omega} r$, where vector $\boldsymbol{\Omega}$ is used to represent the angular velocity vector (see equation (3-10) above). Applying integration of the 2D forces and moments along the wingspan yields:

Translational force and rotational force:

$$\mathbf{F_{q,x}} = \frac{1}{2}\rho\|\boldsymbol{\Omega}\|^2 R^3 \bar{c} C_H(\alpha_e)\hat{I}_{21}\mathbf{e_x} \tag{3-32}$$

$$\mathbf{F_{q,y}} = \left(\frac{1}{2}\rho\|\boldsymbol{\Omega}\|^2 R^3 \bar{c} C_V(\alpha_e)\hat{I}_{21} - C_{rot}\rho\|\boldsymbol{\Omega}\|\omega_z R^2 \bar{c}^2 \hat{I}_{12}\right)\mathbf{e_y} \tag{3-33}$$

The corresponding moments:

$$\mathbf{M_{q,x}} = -\left(\frac{1}{2}\rho\|\boldsymbol{\Omega}\|^2 R^4 \bar{c} C_V(\alpha_e)\hat{I}_{31} - C_{rot}\rho\|\boldsymbol{\Omega}\|\omega_z R^3 \bar{c}^2 \hat{I}_{22}\right)\mathbf{e_x} \tag{3-34}$$

$$\mathbf{M_{q,y}} = \frac{1}{2}\rho\|\boldsymbol{\Omega}\|^2 R^4 \bar{c} C_H(\alpha_e)\hat{I}_{31}\mathbf{e_y} \tag{3-35}$$

$$\mathbf{M_{q,z}} = \hat{x}_{cp}\left(\frac{1}{2}\rho\|\mathbf{\Omega}\|^2 R^3\bar{c}^2 C_V(\alpha_e)\hat{I}_{22} - C_{rot}\rho\|\mathbf{\Omega}\|\omega_z R^2\bar{c}^3\hat{I}_{13}\right)\mathbf{e_z} \quad \textbf{(3-36)}$$

In which, the chord-wise location of centre of pressure is expressed in non-dimensional form, and can be written as:

$$\hat{x}_{cp} = \frac{x_{cp}}{c(r)} = \hat{h} + \frac{0.82}{\pi}|\alpha_e| - 0.45 \quad \textbf{(3-37)}$$

The virtual mass force:

$$\mathbf{F_{a,x}} = \left(-\hat{\lambda}_y\omega_x\omega_z R^2\bar{c}^2\hat{I}_{12} + \hat{\lambda}_{y\omega}{\omega_z}^2 R\bar{c}^3\hat{I}_{03}\right)\mathbf{e_x} \quad \textbf{(3-38)}$$

$$\mathbf{F_{a,y}} = -\left(\hat{\lambda}_y\left(-\dot{\omega}_x + \omega_y\omega_z\right)R^2\bar{c}^2\hat{I}_{12} + \hat{\lambda}_{y\omega}\dot{\omega}_z R\bar{c}^3\hat{I}_{03}\right)\mathbf{e_y} \quad \textbf{(3-39)}$$

The corresponding moments:

$$\mathbf{M_{a,x}} = \left(\hat{\lambda}_y\left(-\dot{\omega}_x + \omega_y\omega_z\right)R^3\bar{c}^2\hat{I}_{22} + \hat{\lambda}_{y\omega}\dot{\omega}_z R^2\bar{c}^3\hat{I}_{13}\right)\mathbf{e_x} \quad \textbf{(3-40)}$$

$$\mathbf{M_{a,y}} = \left(-\hat{\lambda}_y\omega_x\omega_z R^3\bar{c}^2\hat{I}_{22} + \hat{\lambda}_{y\omega}{\omega_z}^2 R^2\bar{c}^3\hat{I}_{13}\right)\mathbf{e_y} \quad \textbf{(3-41)}$$

$$\mathbf{M_{a,z}} = \left(\hat{\lambda}_y\omega_x\omega_y R^3\bar{c}^2\hat{I}_{22} - \hat{\lambda}_{y\omega}\left(-\dot{\omega}_x + 2\omega_y\omega_z\right)R^2\bar{c}^3\hat{I}_{13} - \hat{\lambda}_\omega\dot{\omega}_z R\bar{c}^4\hat{I}_{04}\right)\mathbf{e_z} \quad \textbf{(3-42)}$$

In which, the virtual mass coefficients are expressed in non-dimensional form, and can be written as:

$$\hat{\lambda}_y = \frac{\lambda_y}{c(r)^2} = \frac{\pi}{4}\rho \quad \textbf{(3-43)}$$

$$\hat{\lambda}_{y\omega} = \frac{\lambda_{y\omega}}{c(r)^3} = -\frac{\pi}{4}\rho\hat{h} \quad \textbf{(3-44)}$$

and

$$\hat{\lambda}_\omega = \frac{\lambda_\omega}{c(r)^4} = \frac{\pi}{4}\rho\hat{h}^2 + \frac{\pi}{128}\rho \quad \textbf{(3-45)}$$

3.4.3 **Modelling power consumption**

The energy cost of the FWR wing can be calculated by the time averaged power output over a stroke period (T). For insect flight, the power input to the system by the wing inertia and aerodynamic force cannot be fully stored[40; 48], therefore, the input power is usually neglected[39; 46; 49]. For a practical MAV

design, elastic storage is desirable for energy efficiency, of which the order is decided by the design property of the mechanical system. In the current study, we consider that the mechanical system of the FWR can fully store the input power.

Since the instantaneous aerodynamic power for hovering flight due to gyration of the wing equals directly the dot product of the angular velocity vector ω with the aerodynamic torque τ^{aero}, we have the time averaged power output given by:

$$P^{aero} = -\frac{1}{T}\int_{t=0}^{t=T}(\boldsymbol{\omega}\cdot\boldsymbol{\tau}^{\boldsymbol{aero}}) \quad \textbf{(3-46)}$$

In the above equation, positive power indicates aerodynamic power consumption, and negative power indicates aerodynamic power input to the system. For fully elastic storage mechanical system, these two terms are directly summed together.

3.5 **Quasi-steadiness of FWR Configuration**

For insect flight at low Reynolds number ($\mathrm{Re}\sim10^3$), the aerodynamic force of the flapping wing manipulates several unsteady aerodynamic mechanisms (stable LEV, rotational contribution, added mass force and wake capture[4; 5]). Sane and Dickinson[18; 25] used a model fruit fly (*Drosophila Melanogaster*) wing to experimentally measure the fluid forces due to the stable LEV, wing rotation and added mass inertia, and calculated the forces of the corresponding terms with quasi-steady model. With the exclusion of the forces due to wake capture, the effects of the unsteady mechanisms are explained in detail. For insect flight, rotational force and added mass force mainly occur at the stroke reversal, while the 'steady' force due to stable LEV dominates the wing translation. On the average scale, wing rotation and added mass inertia have together less effect on mean fluid forces generation, however, rotational force may be significant in control and manoeuvre of flight by altering the rotation timing of the wing [25].

Due to the similarity in wing kinematics, FWR manipulates similar aerodynamic mechanisms as insect flapping wing, with a low Ro (of order 1), the gyration of

the FWR wing will maintain a stabilized LEV and has augmented fluid force (Lentink and Dickinson[12]). As confirmed by the CFD study of Wang et al.[29].

Based on the quasi-steady model, we are able to measure the effects of the corresponding terms due to the stable LEV, wing rotation and added mass inertia for the specific kinematic pattern of FWR. Since the wing of FWR is assumed to have constant rotation speed, and sinusoidal flapping and pitching, we define the ratio of rotation velocity to mean flapping velocity as:

$$\eta = \frac{\psi_0}{4\Delta\phi f} \tag{3-47}$$

This dimensionless parameter describes the velocity ratio of the 'steady' rotation and the reciprocating flapping. As η approaches zero, the rotation velocity has negligibly small magnitude compared with flapping velocity, the wing exhibits nearly pure flapping; and as it approaches infinitely large, the wing acts as nearly pure rotation. The instantaneous lift, rotational torque and power coefficients due to the stable LEV, wing rotation and the added mass inertia at $\eta = 0.5$, 3.5 and 9.5 are shown in Figure 3-7, below.

The power coefficient is defined by $\boldsymbol{C_P = \frac{2p}{\rho {U_t}^3 S}}$, the definition of the reference value ($\boldsymbol{U_t}$ and $\boldsymbol{S}$ are same as lift and torque coefficients of equation (3-55) and (3-56)). The geometric AoA at mid-downstroke and upstroke are given as $\boldsymbol{\alpha_d = -10°}$ and $\boldsymbol{\alpha_u = 45°}$; Reynolds number is around 3000. Red, blue and purple lines in Figure 3-7 indicate the 'steady' force due to stable LEV, rotational contribution and added mass inertia, respectively; black dotted lines indicate the total value of the corresponding coefficients.

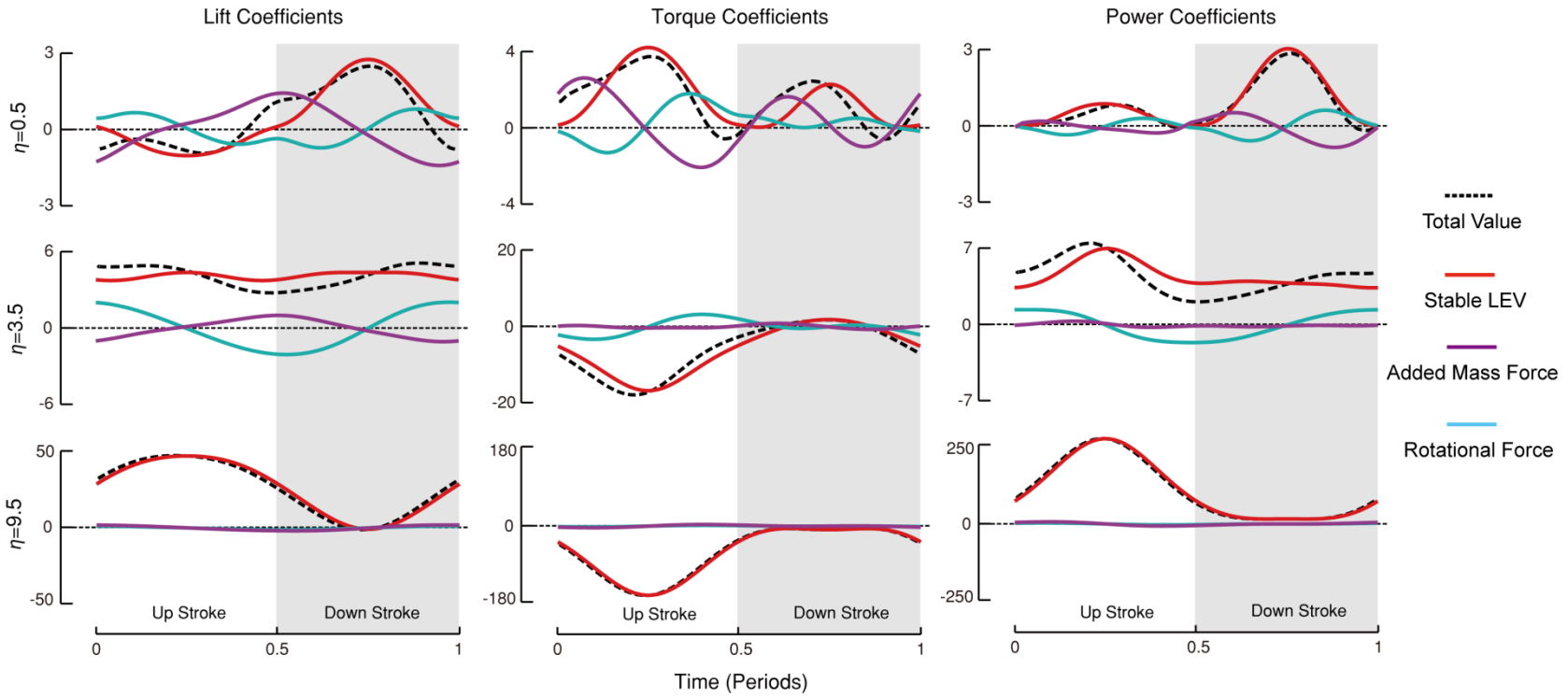

Figure 3-7 Instantaneous lift, rotational torque and power coefficients due to the stable LEV, wing rotation and the added mass inertia at $\eta = 0.5$, 3.5 and 9.5, respectively.

As seen from Figure 3-7, for the given kinematic parameters, the aerodynamic forces and torques of FWR wing is shown to be mostly generated by the 'steady' force and torque due to the stable LEV, the forces and torques due to wing rotation and added mass inertia have together less effect on the instantaneous forces and torques generation.

This unique characteristics of the FWR configuration differs from insect flapping wing, for which wing rotation mainly occurs at the end and beginning of each flapping stroke[4; 5], and exhibits large rotational force and added mass force at stroke reversal[25]. For the kinematic pattern of FWR, the wing exhibits continues rotation over the whole stroke period, therefore, the non-dimensional rotational angular velocity ($\widehat{\omega} = \omega\bar{c}/U_t$) and angular acceleration are much smaller than insect flapping wing, leading to a smaller magnitude of the instantaneous rotational force and added mass force compared to the 'steady' force due to the stable LEV at stroke reversal. Therefore, for the studied kinematic pattern of FWR, the 'steady' force due to the stable LEV dominates the aerodynamic force generation, and the aerodynamic force and torque of the FWR can be sufficiently described through a 'quasi-static' approach.

3.6 **The Effect of Induced Velocity**

To roughly evaluate the effect of induced velocity for the FWR wing, we use a semi-empirical method based on the classical *Rankine-Froude momentum theory*[22; 37]. Due to the coupled flapping and rotation kinematics of the FWR wing, it is convenient to calculate the induced velocity in vector form. The derivation of the vector form equations for the calculation of the induced velocity is presented in Appendix A.

For a differential control surface dS, the induced velocity vector can be calculated by the following equation (see Appendix A, equation (A-11)):

$$\mathbf{dF} = 2\rho(\mathbf{U_{in}} + \mathbf{U_{induced}}) \cdot \hat{\mathbf{n}} \cdot \mathbf{U_{induced}} dS \qquad \textbf{(3-48)}$$

For hovering flight of flapping wing, since the far field velocity $\mathbf{U_{in}}$ equals to zero, and the force generated on dS equals to the lift dL, the equation can be simplified as:

$$dL = 2\rho {U_{induced}}^2 dS \tag{3-49}$$

To decide the induced velocity on a specific wing, we need to consider the distribution of the induced velocity on the stroke plane. Define the distribution function $f(r, \phi)$, the above equation can be written as:

$$dL = 2\rho\left(\overline{U}_{induced}\, f(r, \phi)\right)^2 dS \tag{3-50}$$

Where $\overline{U}_{induced}$ is the average induced velocity on the whole stroke plane S, integration over the stroke plane, we have:

$$L = 2\rho {\overline{U}_{induced}}^2 \int_S f(r, \phi)^2 dS \tag{3-51}$$

Here, a slightly different definition of the area of the 'actuator disc' is defined, compared to Ellington[36]. The area S is approximated by the effective stroke plane area (the definition of Ellington[36], see equation (2-13)) plus twice the wing area, which is a better approximation for the 'area swept by the wing'. This definition helps to solve some complicated kinematics of the wing, a simple example is that when flapping vertically, the projection of the stroke area onto the horizontal plane equals to zero, which will cause singularity when equation (2-13) is used. By the above definition, the effective area of the control surface is written as:

$$S = cos\psi \frac{\Phi}{2} R^2 + 2R\bar{c} = \frac{1}{2}(cos\psi\Phi)R^2 + \frac{1}{2}\left(\frac{4\bar{c}}{R}\right)R^2 = \frac{1}{2}\Phi_e R^2 \tag{3-52}$$

in which, Φ_e refers to the equivalent stroke amplitude, the angle ψ refers to the stroke plane deviation angle. Since $\bar{c}/R$ equals to the inverse of the aspect ratio AR, we have:

$$\Phi_e = cos\psi\Phi + \frac{4}{AR} \tag{3-53}$$

Therefore, we can solve the induced velocity by giving a specific shape of the distribution function $f(r,\phi)$. For a blade element analysis, we simply use a triangular distribution along the span and constant along the stroke position (as shown in Figure A-1). To include the error due to velocity variation and tip losses, the factor k_{ind} is introduced[22; 36; 37], the resultant induced velocity for such distribution can be written as:

$$U_{induced} = k_{ind}\frac{r}{R^2}\sqrt{\frac{2L}{\rho\Phi_e}} \quad \textbf{(3-54)}$$

The induced velocity vector is expressed in the inertial frame and can be transform to the wing-fixed frame by equation (3-2).

In the experimental study of Usherwood and Ellington[22], the force coefficients of a revolving model hawkmoth (*Manduca Sexta*) wing is differentiated to the 'early' (between 60° and 120° from the start of revolution) and 'steady' (between 180° and 450° from the start of revolution) force coefficients. Since the induced downwash of the propeller wake has hardly begun in the 'early' stage, the 'early' coefficients account the 'real' coefficient without the downwash flow[22]. They used a correction factor k_{ind} of 1.2 for the velocity variation and tip losses. This value will be used in our following analyses.

In our study, the effect of the induced downwash velocity is analysed by the quasi-steady model with the induced velocity modelled by the empirically revised momentum theory described above. The results of insect flapping flight are compared with existing literature.

Sun et al.[46] used a computational fluid dynamics (CFD) method to numerically analysis the forces and power of insect flight. The instantaneous force coefficients and power coefficient is used here for our comparison. The kinematics used for the fruit fly wing is simple harmonic function (SHF) of stroke position and pitching (flapping amplitude $\Phi = 150°$, flapping frequency $n = 254\,Hz$, angle of attack at mid-stroke $\alpha = 46°$). The reference velocity U_{ref} is chosen as the average velocity of the wing at r_2 (radius of second moment of wing area) in a stroke period.

The quasi-steady model results are divided by including and excluding the effect of induced velocity. The results of the quasi-steady calculations in comparison with CFD simulations[46] are shown below.

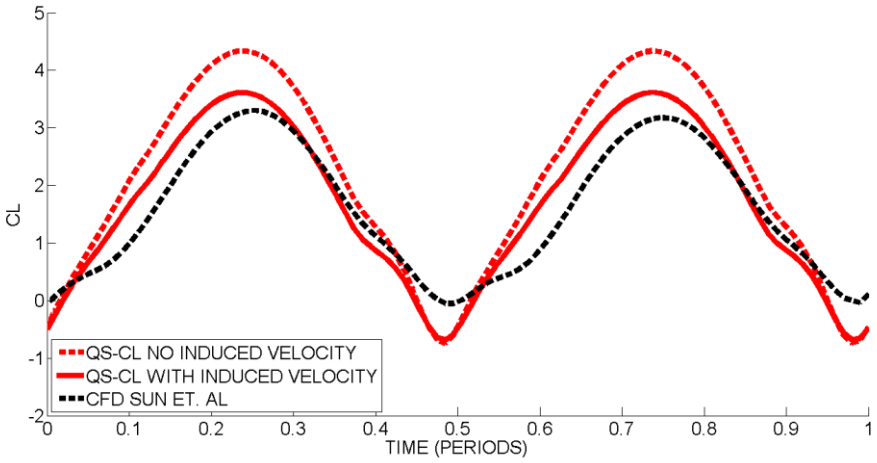

Figure 3-8 Comparison of lift coefficient predicted by quasi-steady aerodynamic model with CFD results (Sun et al.[46]) for fruit fly.

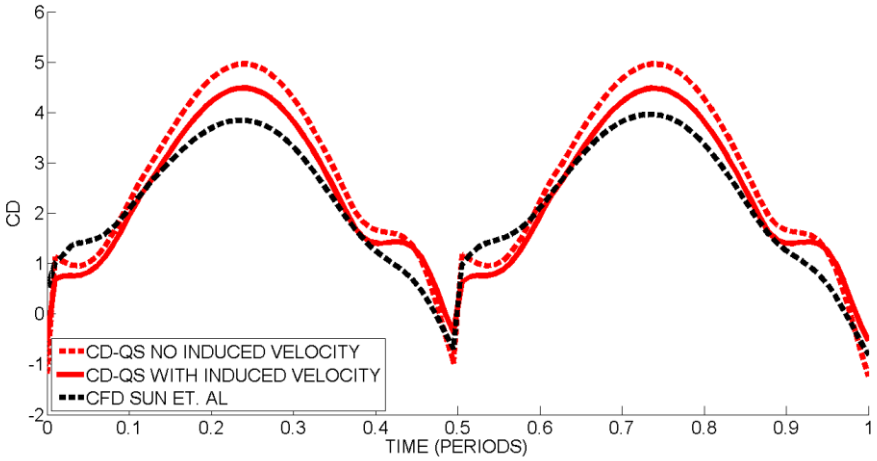

Figure 3-9 Comparison of drag coefficient predicted by quasi-steady aerodynamic model with CFD results (Sun et al.[46]) for fruit fly.

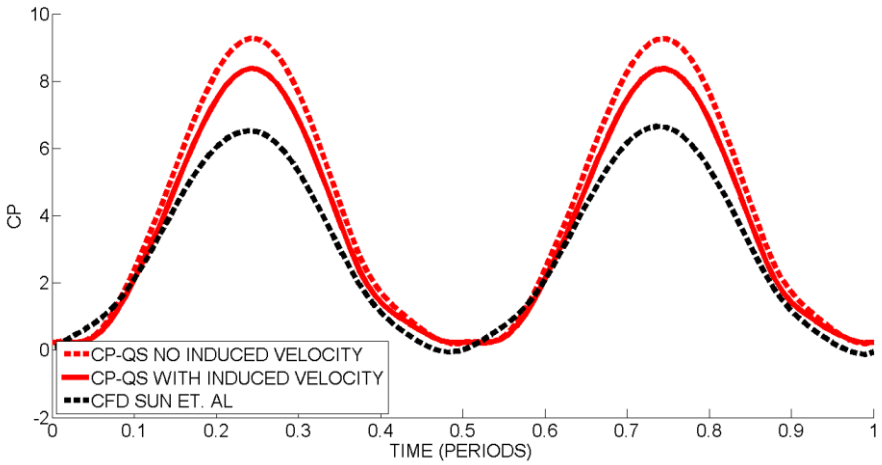

Figure 3-10 Comparison of power coefficient predicted by quasi-steady aerodynamic model with CFD results (Sun et al.[46]) for fruit fly.

In Figure 3-8~Figure 3-10, the red solid line is the coefficients calculated by the quasi-steady aerodynamic model, the induced downwash velocity is cinsidered; the red dotted line is also the calculations of quasi-steady model, but the induced velocity is not considered in aerodynamic force calculation; and the black dotted line is CFD results of Sun et. al[46]. The instantaneous lift coefficient $\boldsymbol{C_L}$, drag coefficient $\boldsymbol{C_D}$ and power coefficient $\boldsymbol{C_P}$ in a stroke period are compared, respectively.

As can be seen from the comparisons, for insect flapping wing, the results of the quasi-steady numerical model show good agreement with the results of CFD simulation. For the case that ignore the induced velocity, the calculated coefficients appear to be slightly overestimated.

For insect flapping wing, the induced downwash velocity of the wing will decrease lift force generated by the wing. This is consistent with theoretical prediction that the downwash flow will reduce the effective AoA of the wing, which reduces the total aerodynamic force coefficient, and causes induced drag on steady airfoil for conventional aircraft. However, unlike conventional aircraft, for which the lift force is perpendicular to the air flow velocity, insect flight at low Reynolds number follows the 'normal force relationship', which states that the fluid force acts perpendicular to the wing[22]. Therefore, a smaller effective

AOA for insect flight also leads to a reduced drag force and power consumption, as predicted by our numerical model (see Figure 3-8~Figure 3-10).

3.7 **Model Validation**

To validate the compatibility of our aerodynamic model, we compared the aerodynamic force (lift) and rotational torque results of our calculation with 3D computational fluid dynamics (CFD) results[29]. The same wing geometry, kinematics and the definitions of the non-dimensional parameters with Wang et al.[29] are used in our comparison. Specifically, 4 different kinematic cases are chosen for comparison, each case changes one of the following parameters of the baseline case: the flapping amplitude $\Delta\Phi$, the mean pitch angle α_0, the pitch amplitude $\Delta\alpha$, and the periodic ratio of flapping to rotation n (defined as the ratio of flapping period $\mathrm{T_f}$ to rotation period $\mathrm{T_r}$, $\mathrm{n} = \frac{\mathrm{T_f}}{\mathrm{T_r}}$); the mean chord length $\bar{\mathrm{c}}$ and the mean flapping velocity at the wing tip $\mathrm{U_t} = 4\Delta\phi\mathrm{fR}$ are defined as the reference length and reference velocity. By this definition, the equations for the calculation of the instantaneous lift and rotational torque coefficients are given as:

$$C_L = \frac{2l}{\rho U_t^2 S} \tag{3-55}$$

$$C_M = \frac{2\tau_r}{\rho U_t^2 S \bar{c}} \tag{3-56}$$

Where l and τ_r are the instantaneous lift and rotational torque of the FWR wing, U_t is the reference velocity, S is the wing area, $\bar{c}$ is the reference length. Of the 4 comparison cases, the Reynold' numbers ($Re = U_t\bar{c}/\upsilon$, where υ is the kinematic viscosity of the fluid) are around 3000. As mentioned before, the force coefficients (C_{Lmax}, C_{Dmax}, C_{D0} and C_{rot}) are obtained from previous empirical studies of insect flapping wing at similar Reynolds number. The coefficients C_{Lmax}, C_{Dmax} and C_{D0} used here are obtained from the experimental study of a hawkmoth (*Manduca Sexta*) wing by Usherwood and Ellington[22]; the rotational force coefficient C_{rot} is obtained from Sane and Dickinson[25]. The comparison of the instantaneous and time averaged forces and torques of the

quasi-steady aerodynamic model with CFD results are shown in Figure 3-11 and Table 3-1.

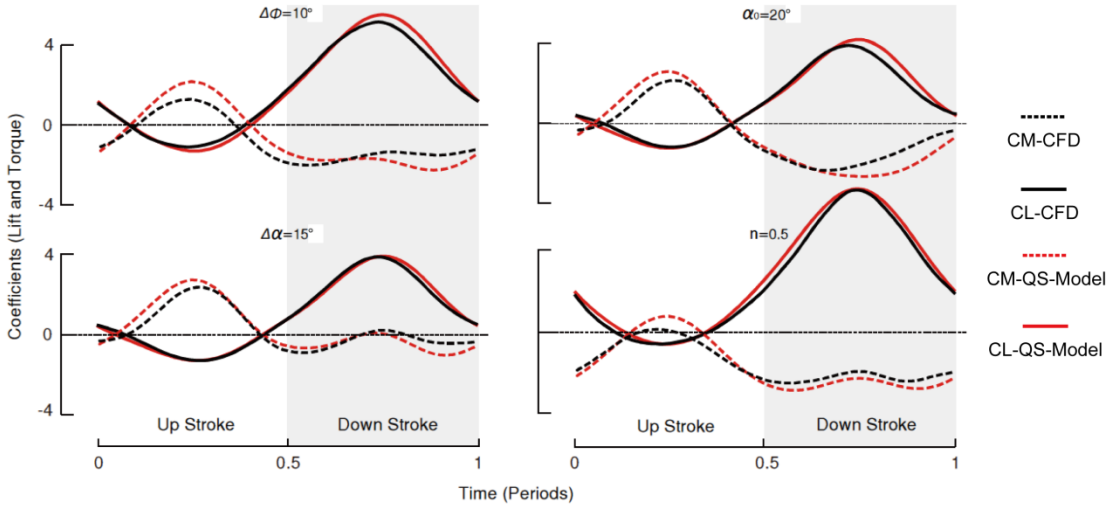

Figure 3-11 Comparison of instantaneous force and rotational torque coefficients (C_L and C_M) with CFD results from Ref.[29].

The quasi-steady prediction and CFD results of $\boldsymbol{C_L}$ are indicated by red and black solid curves; the quasi-steady prediction and CFD results of $\boldsymbol{C_M}$ are indicated by red and black dotted curves. The kinematic parameters of the baseline case are: $\boldsymbol{\Delta\Phi = 15°}$, $\boldsymbol{\alpha_0 = 15°}$, $\boldsymbol{\Delta\alpha = 10°}$ and $\boldsymbol{n = 0.25}$. Each of the 4 cases changes one of the above parameters, the corresponding changed parameters are: $\boldsymbol{\Delta\Phi = 10°}$, $\boldsymbol{\alpha_0 = 20°}$, $\boldsymbol{\Delta\alpha = 15°}$ and $\boldsymbol{n = 0.5}$, respectively. The Reynolds numbers of the 4 cases are around 3000. The coefficients of the aerodynamic model obtained from Usherwood and Ellington[22] and Sane and Dickinson[25] are given as: $\boldsymbol{C_{Lmax} = 1.8}$, $\boldsymbol{C_{Dmax} = 3.4}$, $\boldsymbol{C_{D0} = 0.07}$, $\boldsymbol{C_{rot} = 1.6}$.

Table 3-1 Comparison of time averaged force and torque coefficients ($\overline{C}_L$ and $\overline{C}_M$) with CFD results[29].

Cases(changed parameter)	Quasi-steady Results	CFD Results
$\boldsymbol{\Delta\Phi = 10^\circ}$	$\bar{C}_L = 1.76$ $\bar{C}_M = -0.63$	$\bar{C}_L = 1.73$ $\bar{C}_M = -0.71$
$\boldsymbol{\alpha_0 = 20^\circ}$	$\bar{C}_L = 1.16$ $\bar{C}_M = -0.59$	$\bar{C}_L = 1.1$ $\bar{C}_M = -0.51$
$\boldsymbol{\Delta\alpha = 15^\circ}$	$\bar{C}_L = 0.94$ $\bar{C}_M = 0.32$	$\bar{C}_L = 0.97$ $\bar{C}_M = 0.28$
$\boldsymbol{n = 0.5}$	$\bar{C}_L = 2.83$ $\bar{C}_M = -1.59$	$\bar{C}_L = 2.62$ $\bar{C}_M = -1.51$

As seen in Figure 3-11 and Table 3-1, the instantaneous and time averaged force and torque coefficients of the quasi-steady model agree well with the CFD results. For the instantaneous lift coefficient of the 4 cases, the quasi-steady model predicted almost exactly, but the instantaneous torque coefficient appears to be slightly larger in the upstroke and smaller in the downstroke, which is likely due to the variation of the location of the centre of pressure on the wing at up and downstroke. The time averaged lift and rotational torque coefficients of the 4 cases compared with the CFD results are within 5% and 15% accuracy, respectively.

4 OPTIMAL KINEMATICS AND EFFICIENCY OF FWR

4.1 Introduction

The flapping FWR generates aerodynamic forces including a propulsive force that drives the wing to rotate by itself. Therefore, the FWR MAV is normally operated in a steady state when the rotational speed reaches an 'equilibrium state'. In such condition, the FWR propelling force equals to the drag so that the rotating speed remains constant.

For a practical FWR MAV design, it is desirable to find the optimal kinematics of the wing under the given kinematic pattern. Based on the aerodynamic model discussed in chapter 3, we calculated the lift and power efficiency of the FWR at equilibrium rotational speed, and identified the optimal wing kinematics. The maximum aerodynamic efficiency of the FWR is further compared with insect flapping wing and the man-made rotary wing.

4.2 Equilibrium of FWR

For a thin flat plate airfoil with minimal thickness, due to the flow separation at the leading edge and the loss of leading edge suction, the aerodynamic force is dominated by the pressure difference between the upper and lower surface. If the viscous drag is relatively small, the resultant aerodynamic force follows a 'normal force relationship' that is perpendicular to the wing [22; 32].

For a wing moving at low Ro (of order 1), the leading edge separation forms into the leading edge vortex and stably attach on the upper surface of the wing, with stabilized LEV, a translating wing exhibits aerodynamic performance much like steady case, therefore, the fluid force can be largely described by quasi-steady aerodynamic model [5; 18; 22]. In quasi-steady analysis, for a given Reynolds number and wing geometry, the lift and rotational torque coefficients ($\mathrm{C_L}$ and $\mathrm{C_M}$) of FWR wing varies only with the change of the effective AoA α_e and the ratio of rotational velocity to the mean flapping velocity η. The effective AoA α_e decides the aerodynamic force coefficients of the airfiol, and the ratio η decides the resultant velocity of the wing, i.e., the dynamic pressure. This simple

relationship can be largely explained by writing down the lift coefficient due to the 'steady' LEV (i.e., ignore the rotational force and added mass force[18; 30]):

$$C_{L,steady} = \frac{1}{4}\pi^2 \left(\hat{\dot{\phi}}^2 + \left(\frac{2\eta}{\pi}\right)^2\right) C_V(\alpha_e) \int_0^R \hat{r}^2 \hat{c}(\hat{r}) d\hat{r} \quad \textbf{(4-1)}$$

where $\hat{\dot{\phi}}$ is the variation function of the non-dimensional flapping angular velocity, which is standard sinusoidal function, $\hat{r}$ and $\hat{c}(\hat{r})$ is the non-dimensional span-wise location and the chord length of the wing element, which is decided by the wing geometry. From the above equation, the force coefficient $C_{L,steady}$ varies only with η and α_e, it can be proved that this relationship also applies for the rotational torque coefficient C_M.

For the kinematic pattern of FWR, the effective AoA of the wing α_e can be decided by the geometric AoA (or pitch angle) α, the angle of velocity deflection due to vertical flapping motion β, and the angle due to induced downwash α_i, among which, the latter is considered negligibly small ($\alpha_i \ll \beta$). Therefore, the effective AoA can be evaluated by the summation of the geometric AoA α and the deflection angle due to vertical flapping velocity β. Due to the sinusoidal variation of the wing motion, a simple way to analysis the forces and torque generation is to look at the wing at mid-upstroke and mid-downstroke, where the velocity of the wing reaches its maximum, and therefore, the effective AoA of these two states has the largest influence on the aerodynamic forces production. The aerodynamic forces and the geometric angles of the FWR wing of a typical kinematic pattern are shown in Figure 4-1.

In Figure 4-1a, the lift and rotational torque coefficients ($\boldsymbol{C_L}$ and $\boldsymbol{C_M}$) in a stroke period of typical kinematic pattern (kinematic parameters chosen as: $\boldsymbol{\psi_0 = 5\,r/s}$, $\boldsymbol{f = 22\,Hz}$, $\boldsymbol{\Delta\Phi = 15°}$, $\boldsymbol{\alpha_d = -10°}$ and $\boldsymbol{\alpha_u = 50°}$, the Reynolds number is 3000) are shown as red and black curves. On the lower side shows the corresponding angles, velocities and forces vectors of the FWR wing at mid-up and downstroke. The angles $\boldsymbol{\alpha_e}$, $\boldsymbol{\alpha}$ and $\boldsymbol{\beta}$ refer to the effective AoA, the geometric AoA and the angle of velocity deflection due to vertical flapping motion, respectively. The rotational velocity, the flapping velocity and the

resultant velocity of the wing are indicated by blue arrows. The aerodynamic forces vectors at mid-stroke are shown as purple arrows.

Figure 4-1b shows the wing sections at mid-up and downstroke. Based on the kinematic parameters shown in Figure 4-1a, when changing the AoA of the wing (at mid-upstroke or downstroke), the resultant aerodynamic forces vectors are shown and indicated by purple arrows. **a**. and **b**. changes the upstroke AoA, and keeps the down-stroke AoA the same with Figure 4-1a. **c**. and **d**. changes the downstroke AoA , and keeps the upstroke AoA the same with Figure 4-1a.

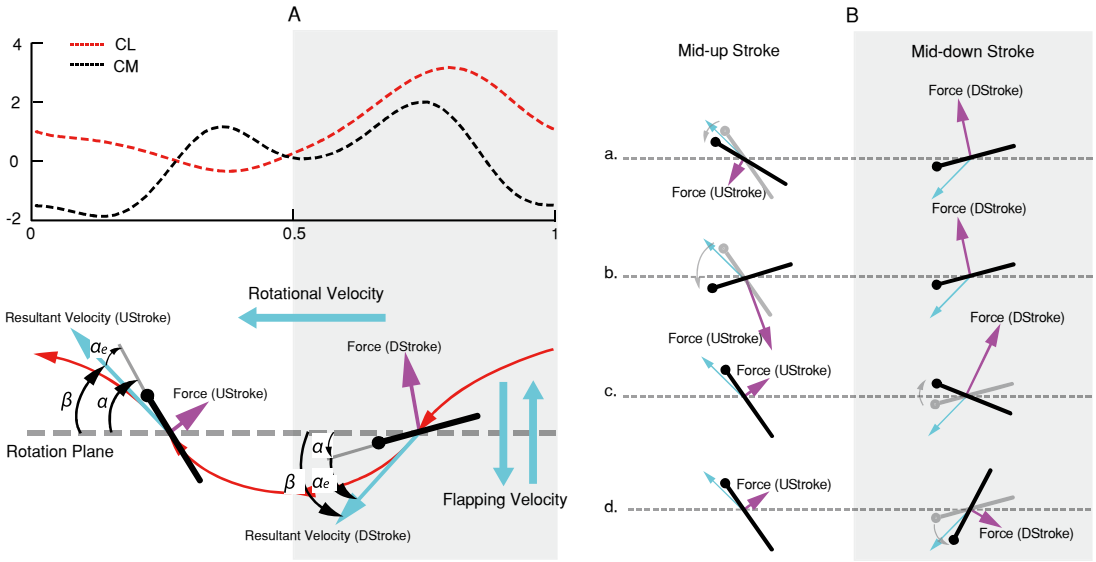

Figure 4-1 (A) Aerodynamic forces and geometric angles of FWR wing at mid-stroke. (B) The variation of aerodynamic forces with the change of AoA at mid-up and downstroke.

For the given kinematic pattern, due to the asymmetric pitching of the wing, at downstroke, the wing has small negative geometric AoA α and positive effective AoA α_e which creates a high lift force and propulsive torque; at upstroke, the wing has positive geometric AoA α and small (positive) effective AoA α_e, which generates a small lift force and anti-rotational torque. The rotational torque reverses its direction at upstroke and downstroke, if they cancel each other out, the FWR reaches the equilibrium state. Figure 4-1b shows some typical cases of how the change of the geometric angles changes the force and torque production. In a., c. and d., the rotational torque at upstroke and downstroke has the same direction, propulsive in a. and anti-rotational in c. and d., therefore, the

FWR does not reach the equilibrium state, a. tends to rotate faster and c. and d. tend to rotate slower, however, the wing can reach the equilibrium state by altering the rotation speed ψ_0 or the ratio η (faster for a. and slower for c. and d.), which changes the resultant velocity and therefore changes the effective AoA α_e; in b., although the rotational torque reverses its direction, it generates large negative lift at upstroke, therefore, the resultant lift is largely reduced (possibly negative).

4.3 **Lift and Power of FWR at Equilibrium State**

For the design concept of FWR MAV, the equilibrium state is the operating condition, at which the rotation of the wing is generated by its own propulsive force due to wing flapping. At equilibrium state, the rotational torque in the downstroke and upstroke cancels each other out, therefore, the rotational torque vanishes in a stroke period ($\bar{\tau}_r = 0$).

As has been discussed above, for a given geometric AoA (α_u and α_d), there exists a only η, at which the FWR reaches its equilibrium state. At this state, the lift coefficient (C_L and $\bar{C}_L$) can be calculated. Unlike horizontal flapping wing or rotary wing, at equilibrium state, the rotational torque of the FWR equals to zero in a stroke period, therefore, the majority of the power consumption is to overcome the vertical force or the lift and the pitching torque of the wing.

To assess the power efficiency, we used the power factor: $P_f = C_L^{3/2}/C_P$, which describes the required power for a certain amount of lift[10; 12; 50]. The dimensionless parameters (ratio of rotational velocity to the mean flapping velocity η, mean lift coefficient $\bar{C}_L$, mean power coefficient $\bar{C}_P$ and power factor P_f) of FWR at equilibrium state under different geometric AoA (α_u and α_d, each ranging from $-90°\sim90°$) are calculated using our quasi-steady model, and shown in Figure 4-2~Figure 4-5.

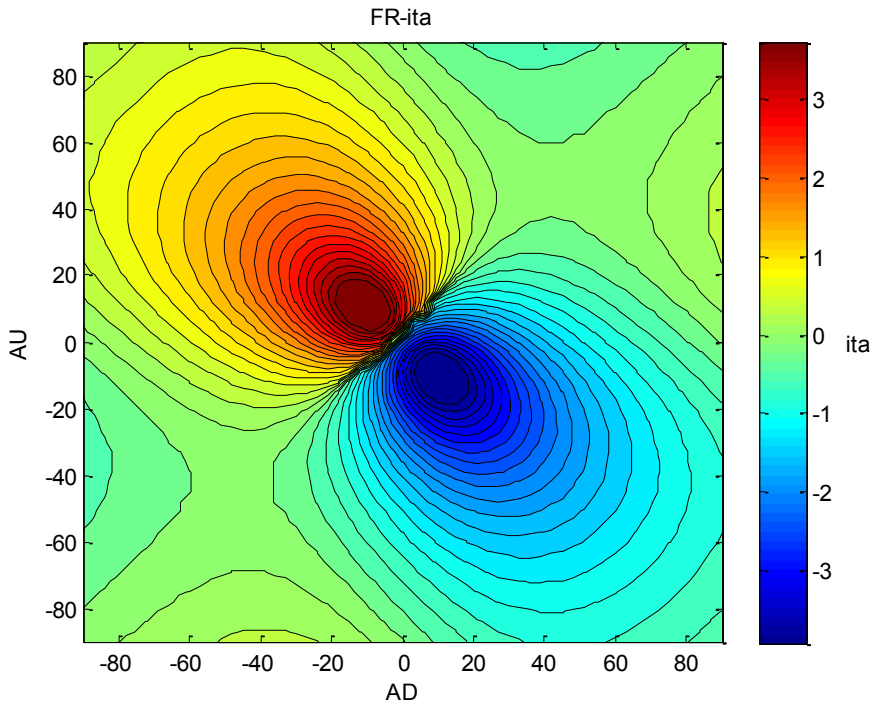

Figure 4-2 The dimensionless parameter η of FWR at equilibrium state under different geometric AoA (ranging from $-90°\sim90°$).

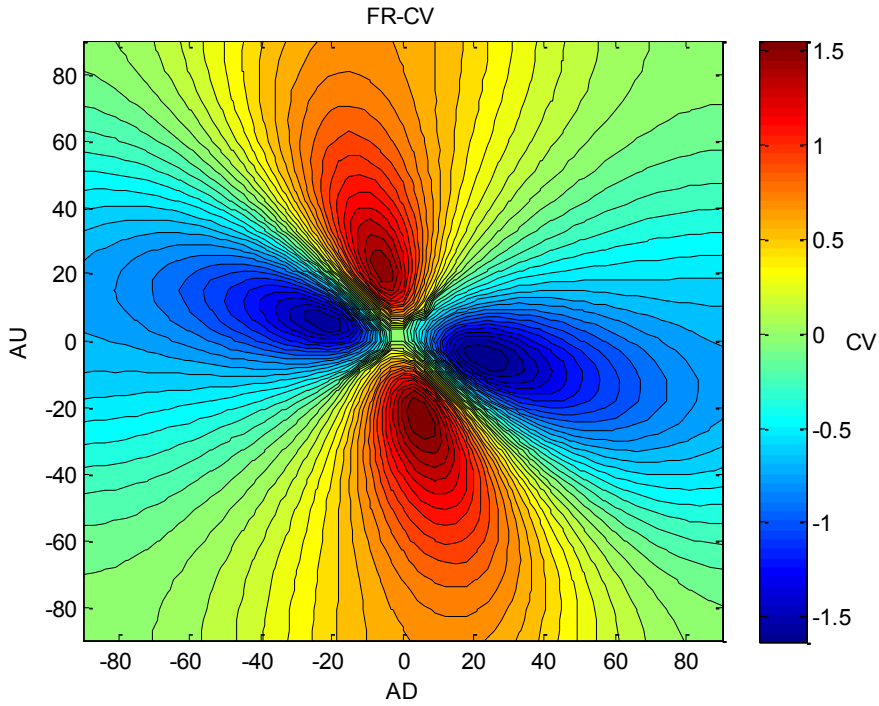

Figure 4-3 The dimensionless parameter $\overline{C}_L$ of FWR at equilibrium state under different geometric AoA (ranging from $-90°\sim90°$).

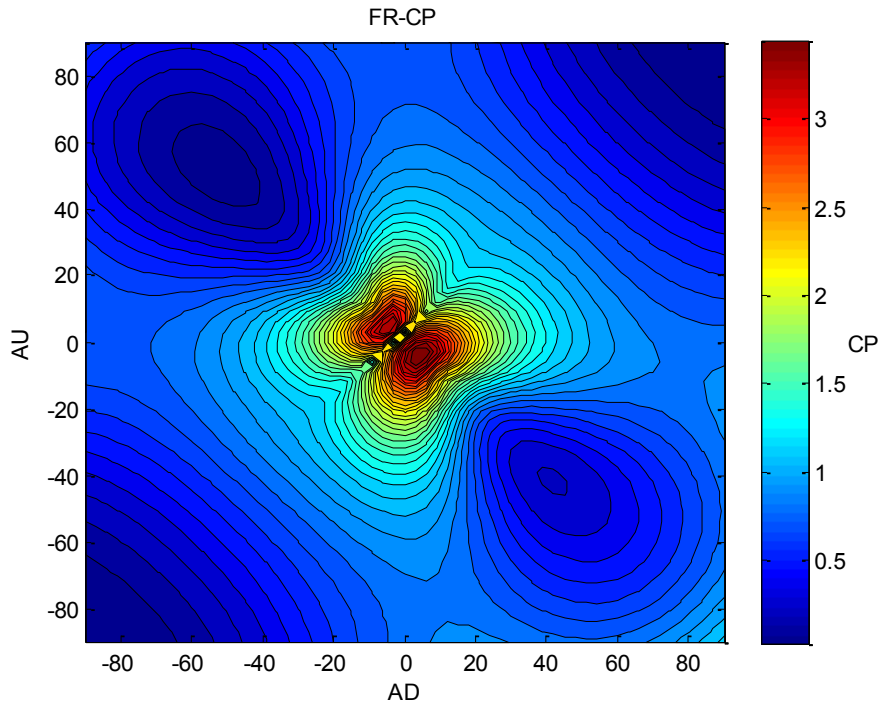

Figure 4-4 The dimensionless parameters $\overline{C}_P$ of FWR at equilibrium state under different geometric AoA (ranging from $-90°\sim90°$).

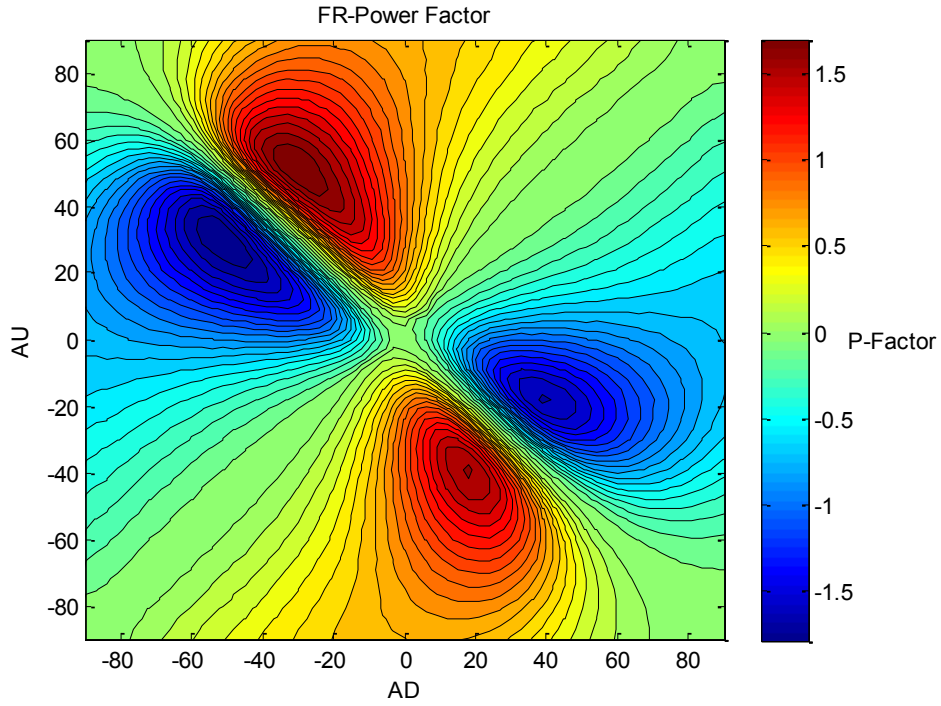

Figure 4-5 The dimensionless parameters P_f of FWR at equilibrium state under different geometric AoA (ranging from $-90°\sim90°$).

In Figure 4-2~Figure 4-5, AD and AU indicates the geometric AoA at mid-downstroke and mid-upstroke, respectively. The pseudocolor represents the magnitude of the corresponding dimensionless parameter.

As seen from the above figures, the dimensionless parameters (ratio of rotational velocity to the mean flapping velocity η, mean lift coefficient $\bar{C}_L$, mean power coefficient $\bar{C}_P$ and power factor P_f) of the FWR show approximately symmetric distribution with respect to the lines $\alpha_d = \alpha_u$ and $\alpha_d = -\alpha_u$.

On the line $\alpha_d = \alpha_u$, since the upstroke AoA and downstroke AoA has the same value, no net force and torque are generated over a stroke period, therefore, the rotational speed (or η) remains zero and no mean lift ($\bar{C}_L$) is generated. The power cost, however, is high near the origin ($\alpha_d = \alpha_u = 0$), since the flapping motion at this point creates a $90°$ deflection angle β, making the effective AoA of the wing $\alpha_e = 90°$, and generates a high drag force to the airfoil.

The peak values of η appear in the line $\alpha_d = -\alpha_u$ (maximum 4.2 at $\alpha_d = -10°$ and $\alpha_u = 10°$), where both the upstroke and downstroke of the flapping motion generate propulsive torques (corresponding to Figure 4-1 B case a.), and therefore, also no net lift ($\bar{C}_L$) is generated.

The rotation of the wing reverses its direction with respect to the line $\alpha_d = \alpha_u$, which is due to the opposite symmetric generation of the rotational torque. For the reversed rotation, the lift generation is similar with the original, which can be treated as an inverted set of the FWR wing, the upstroke becomes downstroke, and downstroke becomes upstroke, therefore, the generated lift reverses its sign.

From the quasi-steady calculations, the mean lift coefficient $\bar{C}_L$ has peak value 1.5 at $\alpha_d = -5$ and $\alpha_u = 23$; the mean power coefficient $\bar{C}_P$ has peak value 3.6 at $\alpha_d = 6$, $\alpha_u = -8$; the power factor P_f has peak value 1.6 at $\alpha_d = -35$, $\alpha_u = 52$.

4.4 **Comparison with Insect Flapping Wing and Micro Rotorcraft**

The energy efficiency of flight is one of the most important feature for a typical air vehicle design, which decides the duration of operations, payload carrying and power implantation. Due to the VSTOL operation requirements, the energy efficiency of hovering flight, as opposed to forward flight, is especially important for MAVs. Therefore, it is desireble to compare the energy efficiency of the new FWR configuration with conventional MAVs concept.

In this analysis, we calculated the hover flight power factor (P_f, see last chapter) of the FWR and previously proposed MAVs (conventional rotory wing and insect-like flapping wings) with the quasi-steady aerodynamic model described in chapter 3.4 (the variations of the corresponding dimensionless parameters $\bar{C}_L$, P_f, $\bar{C}_P$ and $\bar{C}_D$ with respect to the geometric AoA of typical kinematic patterns of insect flapping wing: fruit fly-like horizontal flapping and dragonfly-like vertical flapping are given in Appendix B).

The calculations of the three configurations are under the same size and shape of the wing, and with the same emprical coefficients of the aerodynamic model (except the drag coefficient of the airfoil at zero AoA $\mathrm{C_{D0}}$).

Among the emprical coefficients in the quasi-steady model, the one that is most sensitive to Re is $\mathrm{C_{D0}}$, $\mathrm{C_{D0}} \sim 1/\sqrt{\mathrm{Re}}$. In our calculations, this parameter is given as 0.4 and 0.07 to model the flight conditions at different Reynolds number (Re), e.g. the fruit fly (*Drosophila Melanogaster*) and hawkmoth (*Manduca Sexta*) with $\mathrm{Re} \sim 100$ and $\mathrm{Re} \sim 7000$, respectively (Sane and Dickinson[18] and Usherwood and Ellington[22]). The resultant power factors $\mathrm{P_f}$ versus the mean lift coefficient $\bar{\mathrm{C}}_\mathrm{L}$ at these two Reynolds number are shown in Figure 4-6.

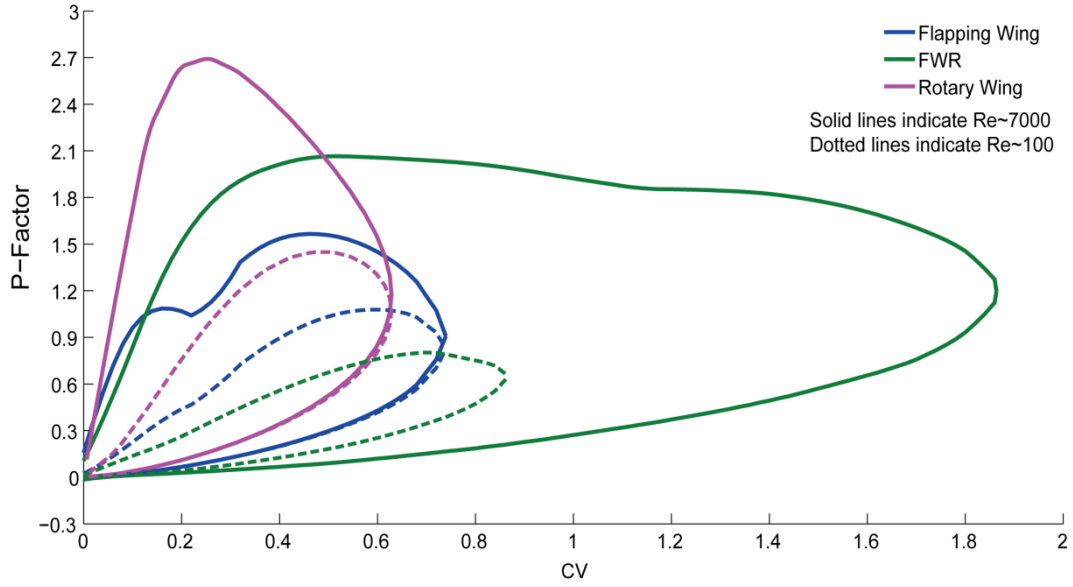

Figure 4-6 The comparison of power factors P_f versus the mean lift coefficient $\overline{C}_L$ of insect-like flapping wing, conventional rotory wing and FWR. The calculations are based on $\mathbf{Re{\sim}100}$ and $\mathbf{Re{\sim}7000}$, respectively.

In Figure 4-6, for each lift coefficient in horizontal axis, the plotted lines gives the efficiency limits of each configuration.

As seen from the above figure, the FWR configuration has the highest lift coefficients compared with conventional rotory wing and insect-like flapping wing at both Reynold'd numbers ($\mathrm{Re{\sim}100}$ and $\mathrm{Re{\sim}7000}$), which implies that the FWR has higher manoeuvrability and payload carrying ability than the other two configurations.

At high Reynolds number ($\mathrm{Re{\sim}7000}$), the aerodynamic efficiency of the FWR configuration is higher than insect-like flapping wing, and slightly lower than rotory wing; at very low Reynolds number ($\mathrm{Re{\sim}100}$), the aerodynamic efficiency of FWR configuration drop dramatically and is lowest among the three configurations.

5 EXPERIMENT-I: FWR STRUCTURES FOR OPTIMAL WING MOTION

5.1 Introduction

As discussed in chapter 3 and 4, the aerodynamic performance of the FWR is largely determined by the variation of the geometric AoA at upstroke and downstroke. In order to generate a positive lift force, the FWR wing is required to pitch asymmetrically at upstroke and downstroke.

For most insect flight, the pitching kinematics of the wing can be controlled actively for the alteration of the aerodynamic force to perform manoeuvre. However, there is also direct evidence that insects can manipulate passive pitching dynamics (Ennos[51] observed that torsional waves of *Diptera* wings begin at the tip rather than the base), which is beneficial for energy efficiency, since no pitching torque is required from the musculature of the insects. For a mechanical device, passive pitching is also desirable for the simplicity and energy efficiency. Therefore, the structure of the wing and the pitching dynamics are especially important for the design of such a MAV.

In this chapter, the wing structure that is able to achieve the asymmetric and passive pitching motion is designed and manufactured. A mechanical FWR device is used to experimentally investigate the lift production of the FWR wing design. In order to find the optimal pitching rigidity for the desired motion. Three FWR wings with the same geometry but different pitching rigidities are tested, the forces against input powers are measured and compared. This study serves as the first step for the understanding of the passive pitching aeromechanics of the asymmetric pitching FWR wing and the design of a practical FWR MAV.

5.2 Design of Test Wing

5.2.1 Geometry and structure layout

The design concept of the test wing is shown in Figure 5-1. The geometric parameters of the wing were selected in order to keep morphological similarity with available insect data (including the aspect ratio AR and the first, second

and third radius of non-dimensional moment of wing area, $\hat{r}_1(S)$, $\hat{r}_2(S)$ and $\hat{r}_3(S)$).

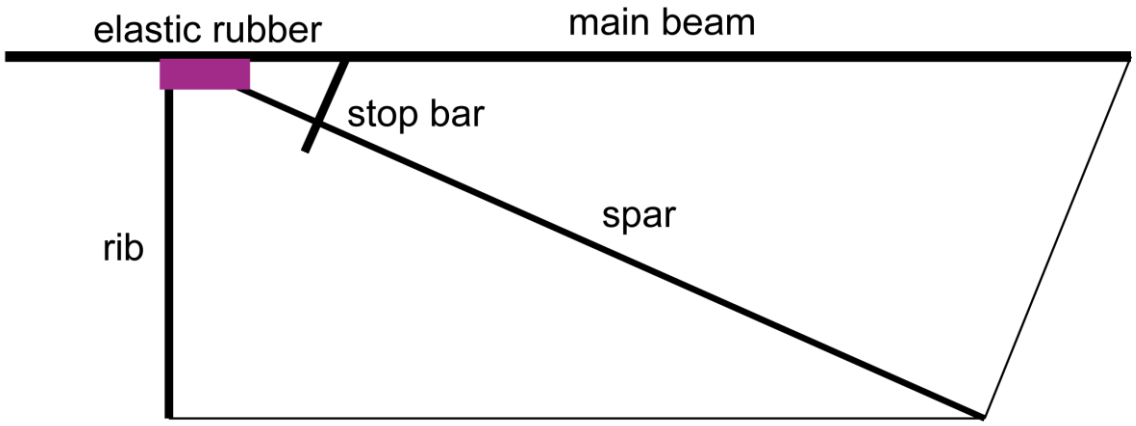

Figure 5-1 Geometry and structure layout of the test wing

The wing is supported by a main beam, a spar and a rib. The elastic rubber is used to attach the spar and rib onto the main beam; an alternative stop bar is mounted on the main beam to creat the asymmetric pitching rigidity at upstroke and downstroke.

For the purpose of easy manufacturing, simple rectangular wing with sharp edges are used. At the wing root, the wing is terminated at the rib in order to be mounted on the mechanical device. The wing weighs approximately 0.3g. The shape and geometric parameters are given in Table 5-1 below:

Table 5-1 Shape and geometric parameters of the wing design.

Shape and Geometric Parameters	
Wing Span **R** (mm)	105
Mean Chord Length $\bar{\mathbf{c}}$ (mm)	33
Aspect Ratio **AR**	3.2
$\hat{\mathbf{r}}_1(\mathbf{S})$	0.51
$\hat{\mathbf{r}}_2(\mathbf{S})$	0.56
$\hat{\mathbf{r}}_3(\mathbf{S})$	0.61

5.2.2 **Wing materials**

The main beam, the spar and the rib of the aeroelastic wing are made of carbon/epoxy rods, which serve as the frame and support the shape and contour of the wing. The plastic membrane is glued onto the carbon/epoxy frame.

5.2.3 **Elastic joint and stopper for asymmetric pitching**

We used a main beam with large bending and torsional rigidity. The spar and the rid of the wing is attached to the main beam through an elastic rubber. Therefore, the pitching of the wing is obtained by the elastic deformation of the rubber. By changing the elasticity of the rubber, the pitching rigidity of the wing can be modified. The same wing with 3 different pitching rigidities are used for our experiments: the most rigid one (where the geometric AoA at mid-upstroke: $\alpha_u = 21°\sim36°$), the medium rigid one ($\alpha_u = 33°\sim45°$) and the flexible one ($\alpha_u = 54°\sim78°$).

A stop bar is mounted on the main beam of the wing. At downstroke flapping, the stop bar stops the wing from pitching upwards, forming a large effective AoA, and at upstroke, the wing is free pitching downwards, only small negative lift is generated, thus, creating an asymmetric pitching rigidity at upstroke and downstroke.

The resultant pitching motion of the wing is captured by high speed camera sequences. Figure 5-2 shows the typical pitching of the wing at up and downstroke, respectivelly.

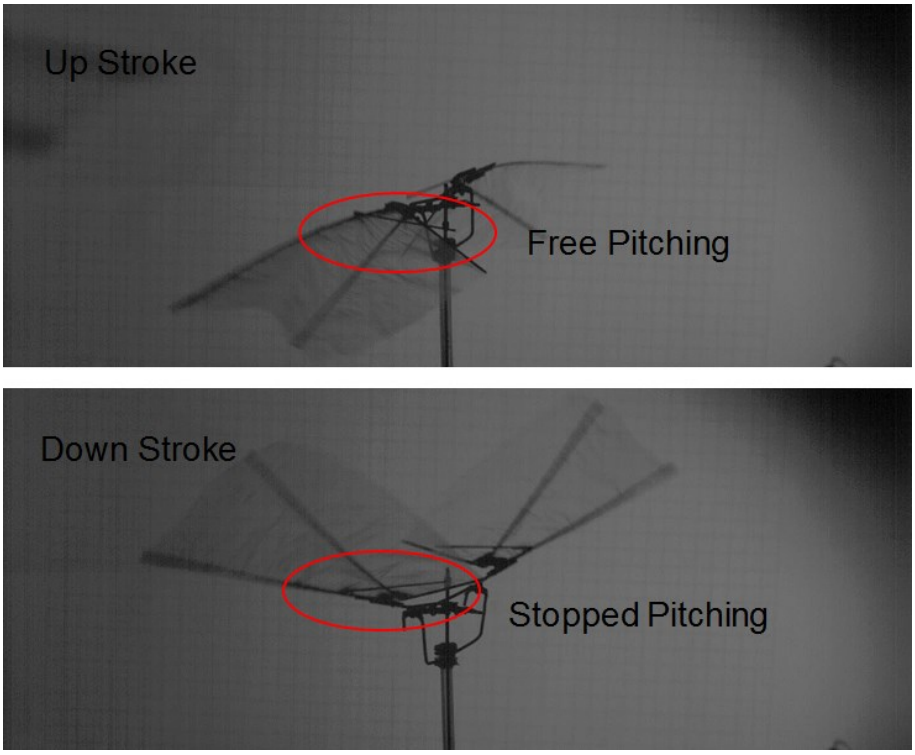

Figure 5-2 The resultant pitching motion of the test wing.

5.3 **Experimental Setup and Work-flow**

We used a simple mechanical device to model the FWR wing motion. The FWR device is shown in Figure 5-3 below.

The mechanical device uses a crank-slider mechanism to transmit the rotary motion of the DC motor into reciprocating up and down motion. A pair of flapping wings is free to rotate around the rotation bearing. DC motor is connected to a constant-current power source to provide electric power. By vertically flapping, the wings start to rotate due to the flapping propulsive force, and finally reach the equilibrium rotational speed.

The kinematics of the FWR wing is captured by a high speed camera. The captured motion is further analysed for the flapping frequency, the rotational speed, the flapping amplitude and the geometric AoA measurements.

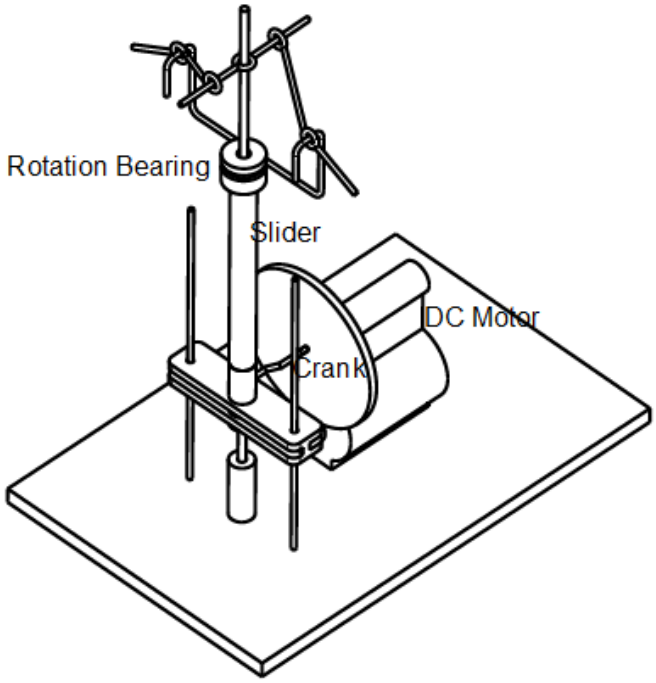

Figure 5-3 The mechanical FWR device for modelling wing motion.

The experimental setup and work-flow for the forces and motions measurements are shown in Figure 5-4 and Figure 5-5. The model FWR is mounted on a load cell for the instantaneous lift measurement; the electric signal is transmitted to PC through a signal amplifier; simultaneously, a high speed camera is used to capture the wing motion of the FWR device.

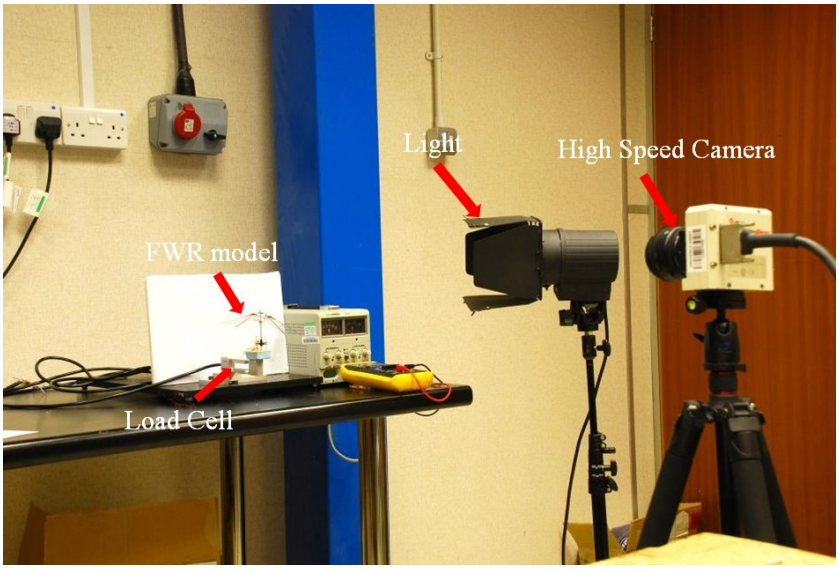

Figure 5-4 Experimental setup of the experiments.

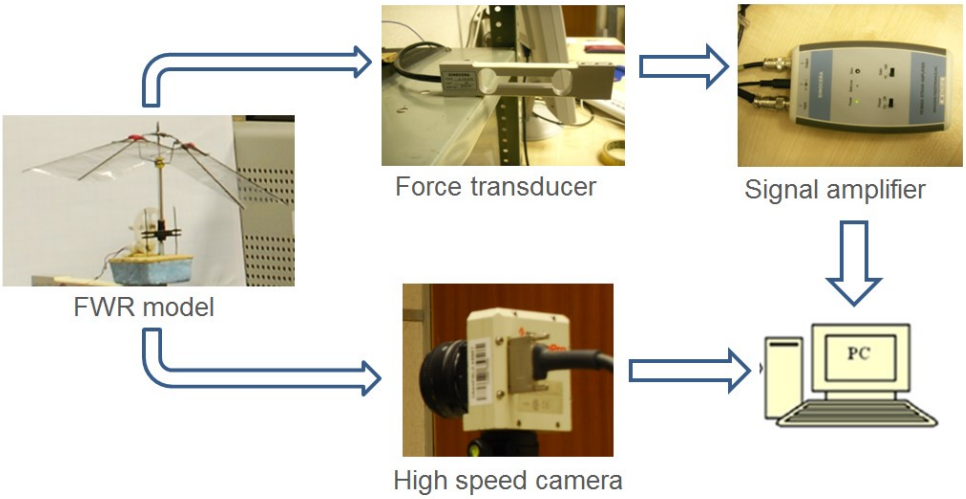

Figure 5-5 Experimental work-flow of the experiments.

The lift and kinematics of FWR wing at different pitching rigidities are measured. The asymmetric pitching motion of the wing is realised by the design of the wing with asymmetric pitching rigidity at upstroke and downstroke (described in the previous chapter). For all the experimental cases, the downstroke geometric AoA are restricted to $\alpha_d < 25°$, and the upstroke geometric AoA changes with the elasticity of the rubber. We measured the lift force of the same wing with 3 different pitching rigidities: the most rigid one, the medium rigid one and the flexible one. For each wing, we measured the lift and wing motion at equilibrium (where the rotational speed reaches equilibrium) of 4 different input electric current for the motor: $I = 0.2, 0.25, 0.3$ and 0.35 A. To reduced the random error of measurements, for each experimental case, we measured the lift twice, each covers 150~300 flapping periods. The Reynolds numbers for our experiments were calculated to be approximately within 3000~5000 using the equation:

$$Re = \frac{U_t \bar{c}}{\upsilon} \quad \textbf{(5-1)}$$

Where U_t is the mean flapping velocity at the wing tip, $\bar{c}$ is the mean chord length and υ is the kinematic viscosity of the fluid.

5.4 **Lift and Kinematics Measurements**

The aerodynamic force is measured only in vertical direction, i.e., only lift force is measured. We used a sampling rate of 3000 Hz for the load cell (SINOSERA, CL-YB-8/5N, accuracy 0.2%) and 1000 Hz for the high speed camera to simutaneously measure the lift force and the wing motion. The sampling time lasts for 10s. To ensure the force were measured at equilibrium rotational speed, data recording starts 10s after the input current is stablized.

Since the force due to the wing inertia is difficult to be substracted from the total lift, the instantaneous value of the pure aerodynamic lift is also difficult to obtain. However, the inertia force of the wing mass can be considered as internal force, and on average scale, has no effect on the mean lift production. Therefore, for the current study, we measured the average force in the vertical direction, which assumed to be only the aerodynamic lift generated by the wing.

The captured high speed camera sequences are used for the kinematics measurements. The flapping frequency *f* and rotational speed *n* is determined by counting the number of frames over 10 flapping circles and rotational circles (N_f and N_n), and calculated as:

$$f = \frac{10\times1000}{N_f} \quad \textbf{(5-2)}$$

$$n = \frac{10\times1000}{N_n} \quad \textbf{(5-3)}$$

Since we used the same mechanical device and wing (with different pitching rigidity) for all the experimental cases, the flapping amplitudes change only slightly at different experimental cases (due to the bending response of the main beam). In our analysis, we assume the flapping amplitudes for all the cases remain constant, and is approximately $27°$ (see Figure 5-6 below).

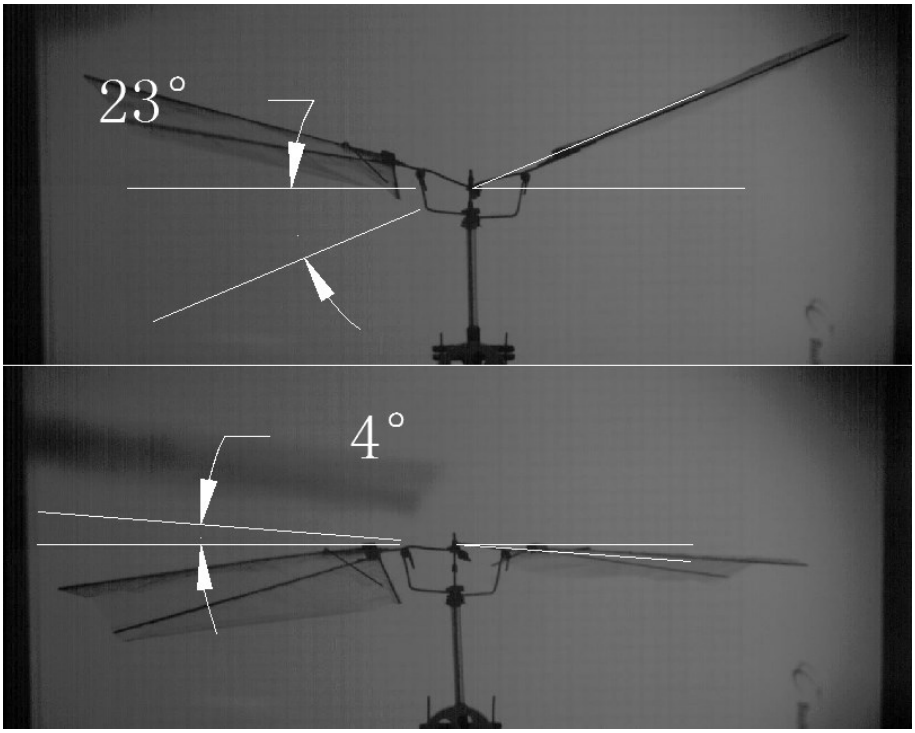

Figure 5-6 The flapping amplitude Φ of the FWR device.

After the lift, the flapping frequency and the flapping amplitude are measured, the lift force is further converted to the dimensionless lift coefficient:

$$\bar{C_L} = \frac{L}{4\rho\Phi^2 f^2 R^3 \bar{c}} \quad \textbf{(5-4)}$$

Where L is the mean lift force, Φ is the flapping amplitude, f is the flapping frequency, R is the wing span length, $\bar{c}$ is the mean chord length of the wing. The geometric parameters are obtained from Table 5-1.

The pitching angle of the wing is measured at the position $\hat{r}_2(S)$ (the radius of the non-dimensional second moment of wing area), which, according to blade element theory, is the critical element which decides the fluid force of the wing. For our wing shape, the value of $\hat{r}_2(S)$ is approximately 0.6 (see Table 5-1 above).

5.5 **Results**

5.5.1 **Lift production of the most rigid wing ($\alpha_u = 21°\sim36°$)**

Table 5-2 Lift production of the most rigid wing, input current $I = 0.2, 0.25, 0.3$ and 0.35 A.

Input current	I(A)	0.20	0.25	0.30	0.35
Input power	P(W)	0.35	0.53	0.76	1.07
Mid-upstroke AoA	α_u(deg)	21	25	32	36
Mid-downstroke AoA	α_d(deg)	-9	-11	-14	-16
Flapping frequency	f(Hz)	16.08	18.34	22.60	27.49
Rotation speed	n(R/s)	3.83	6.67	7.52	8.20
Average lift	L(g)	1.13	1.68	1.95	2.67
Mean lift coefficient	$\bar{C}_L$	1.03	1.18	0.90	0.83

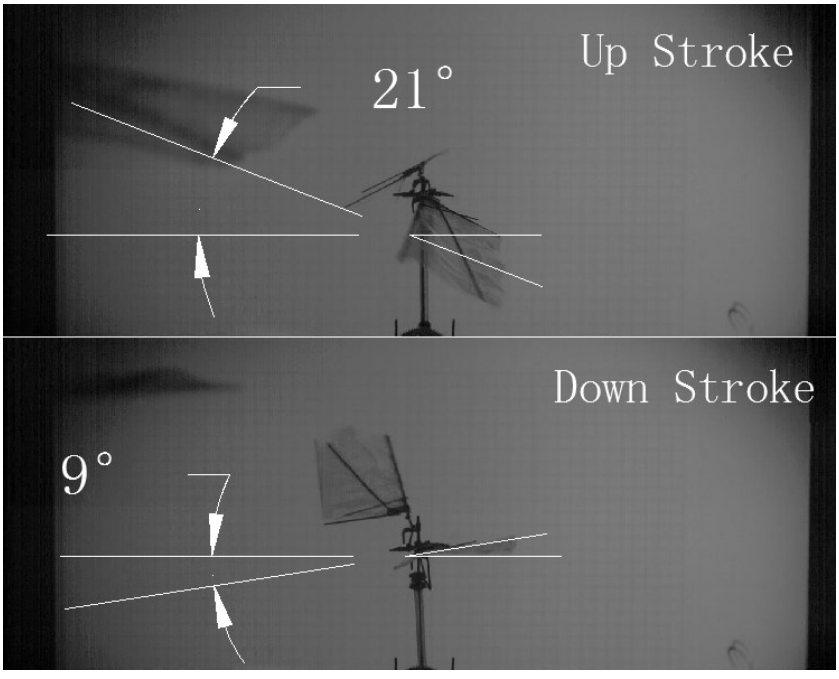

Figure 5-7 Geometric AoA at mid-upstroke (α_u) and mid-downstroke (α_d) of the most rigid wing at input current $I = 0.2$.

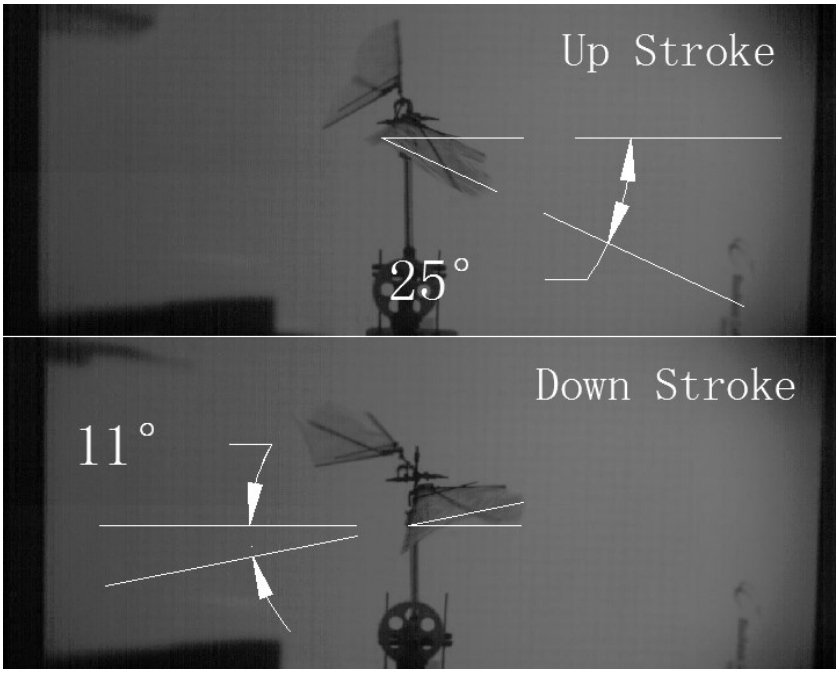

Figure 5-8 Geometric AoA at mid-upstroke (α_u) and mid-downstroke (α_d) of the most rigid wing at input current $\mathbf{I = 0.25}$.

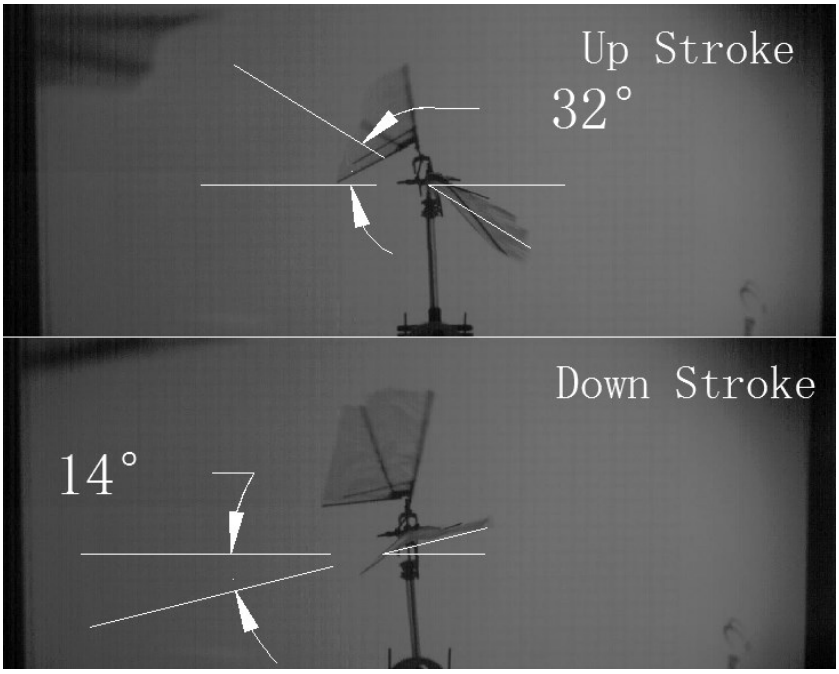

Figure 5-9 Geometric AoA at mid-upstroke (α_u) and mid-downstroke (α_d) of the most rigid wing at input current $\mathbf{I = 0.3}$.

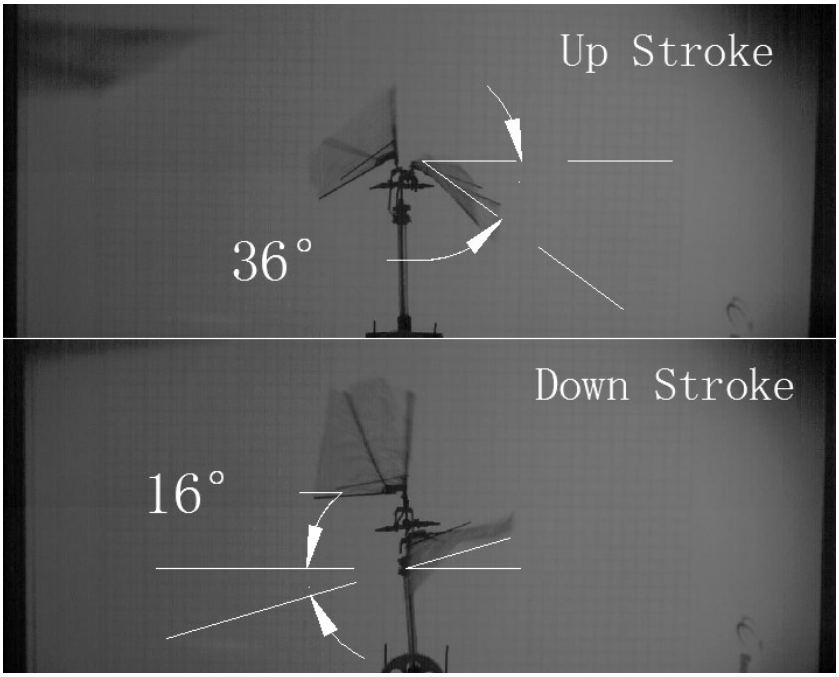

Figure 5-10 Geometric AoA at mid-upstroke (α_u) and mid-downstroke (α_d) of the most rigid wing at input current $\mathbf{I = 0.35}$.

5.5.2 Lift production of the medium rigid wing ($\alpha_u = 33°\sim45°$)

Table 5-3 Lift production of the medium rigid wing, input current $\mathbf{I = 0.2}$, $\mathbf{0.25}$, $\mathbf{0.3}$ and $\mathbf{0.35}$ A.

Input current	I(A)	0.20	0.25	0.30	0.35
Input power	P(W)	0.35	0.53	0.79	1.05
Mid-upstroke AoA	α_u(deg)	33	34	37	45
Mid-downstroke AoA	α_d(deg)	-9	-13	-17	-23
Flapping frequency	f(Hz)	16.63	19.43	24.69	27.96
Rotation speed	n(R/s)	5.75	7.04	7.63	7.69
Average lift	L(g)	1.95	2.45	3.10	3.47
Mean lift coefficient	$\bar{C}_L$	1.66	1.53	1.20	1.05

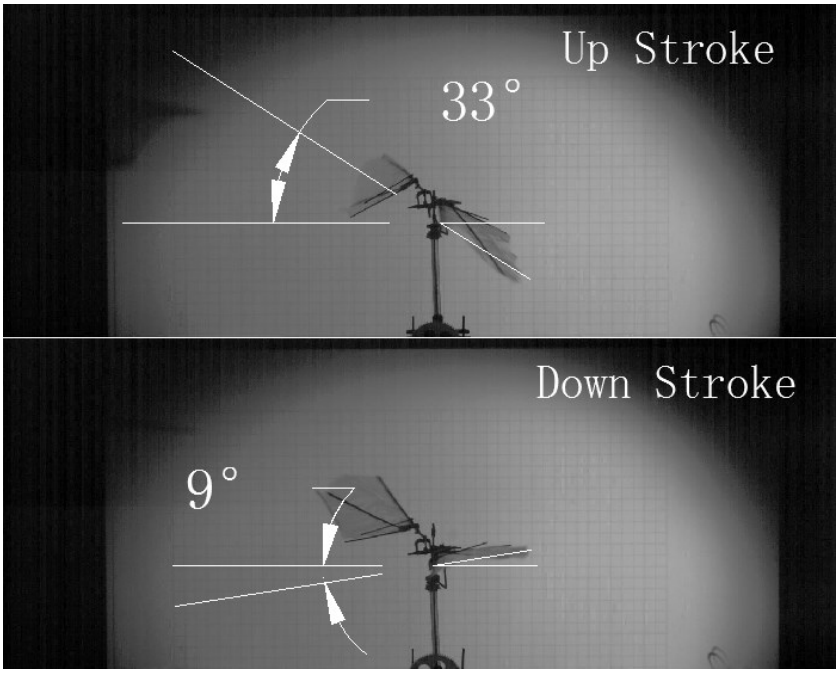

Figure 5-11 Geometric AoA at mid-upstroke (α_u) and mid-downstroke (α_d) of the medium rigid wing at input current $\mathbf{I = 0.2}$.

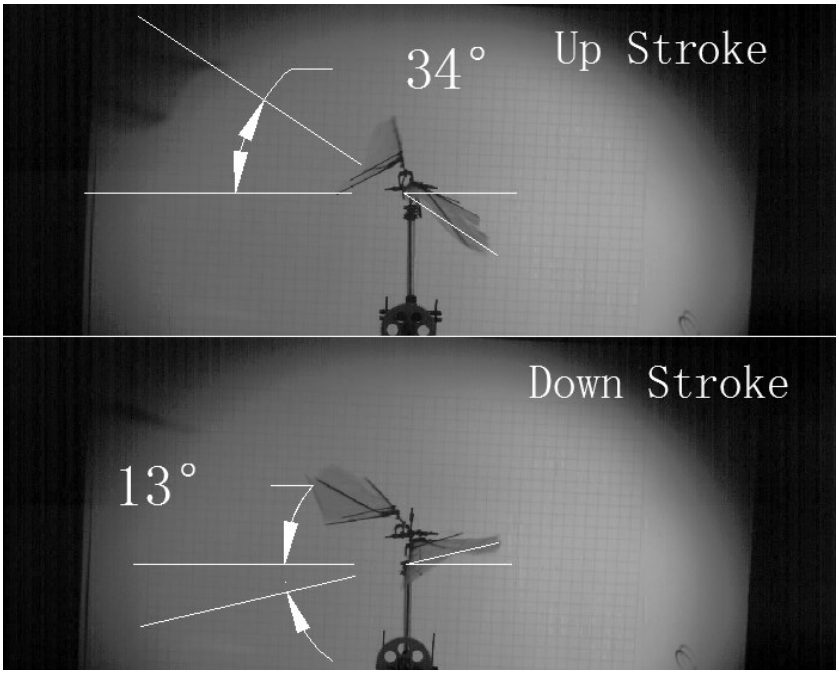

Figure 5-12 Geometric AoA at mid-upstroke (α_u) and mid-downstroke (α_d) of the medium rigid wing at input current $\mathbf{I = 0.25}$.

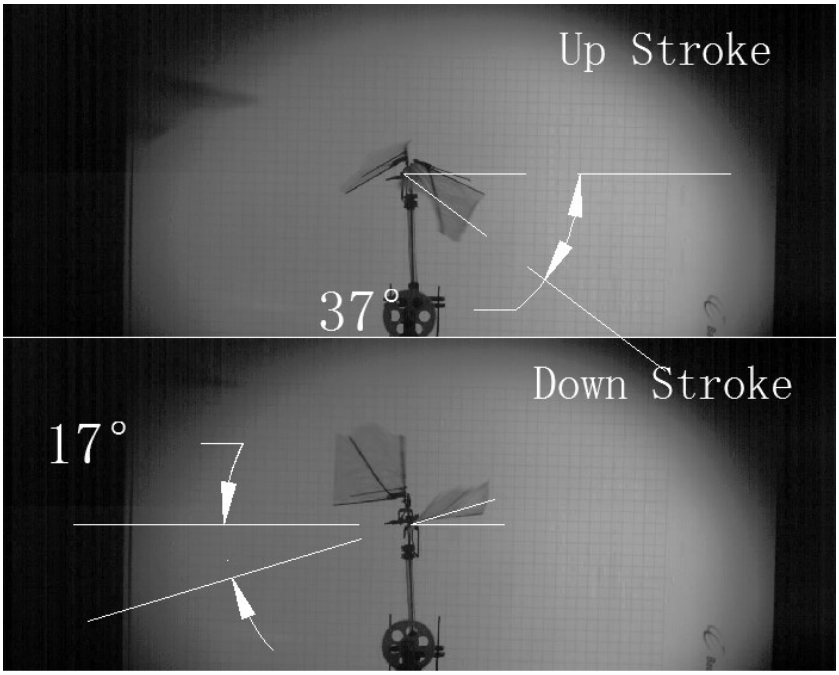

Figure 5-13 Geometric AoA at mid-upstroke (α_u) and mid-downstroke (α_d) of the medium rigid wing at input current $I = 0.3$.

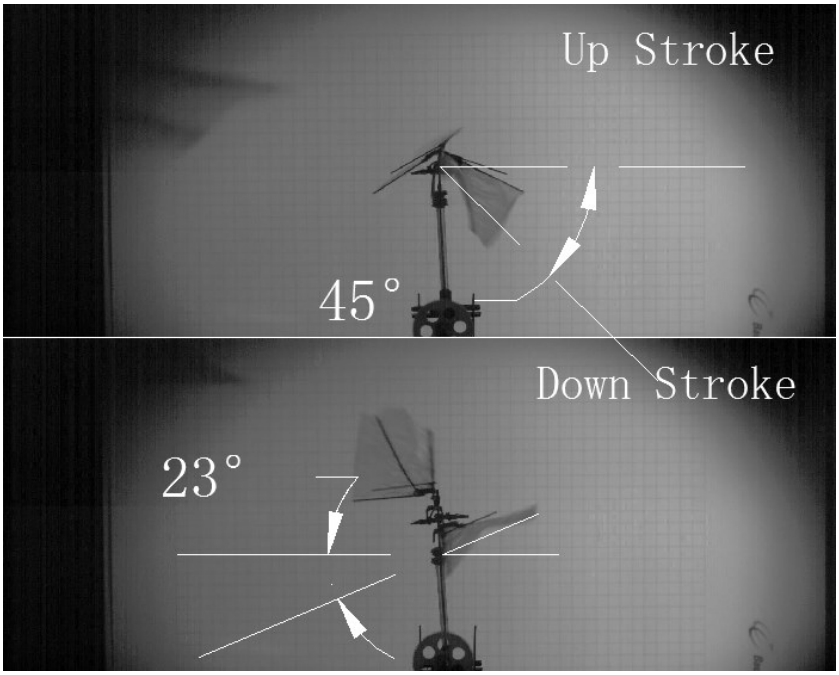

Figure 5-14 Geometric AoA at mid-upstroke (α_u) and mid-downstroke (α_d) of the medium rigid wing at input current $I = 0.35$.

5.5.3 **Lift production of the flexible wing ($\alpha_u = 54°\sim78°$)**

Table 5-4 Lift production of the flexible wing, input current $I = 0.2$, 0.25, 0.3 and 0.35 A.

Input current	I(A)	0.20	0.25	0.30	0.35
Input power	P(W)	0.35	0.53	0.77	1.02
Mid-upstroke AoA	α_u(deg)	54	59	69	78
Mid-downstroke AoA	α_d(deg)	-11	-22	-23	-27
Flapping frequency	f(Hz)	16.95	20.19	22.69	24.62
Rotation speed	n(R/s)	3.25	4.02	4.88	5.26
Average lift	L(g)	1.27	1.97	2.22	2.45
Mean lift coefficient	$\bar{C}_L$	1.05	1.14	1.02	0.95

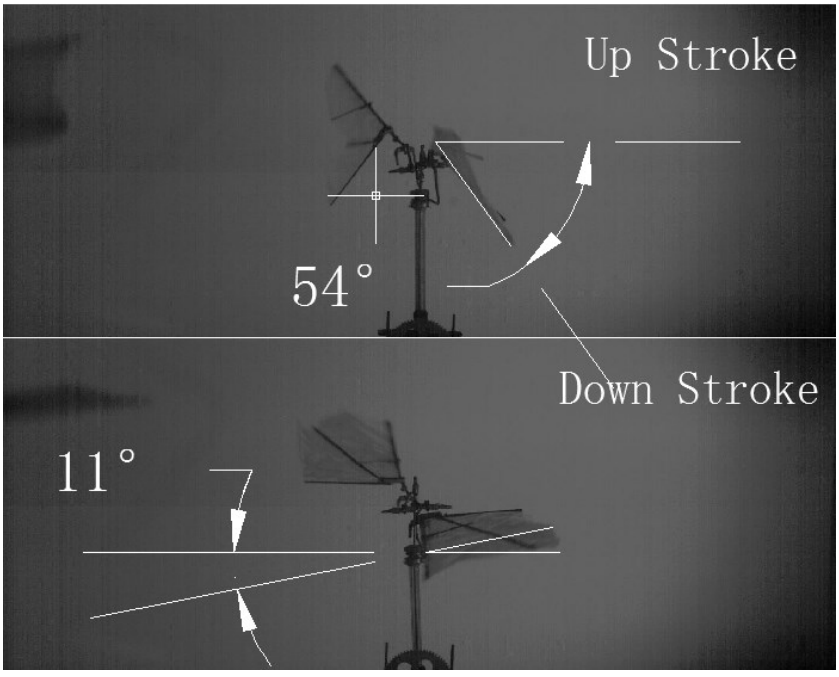

Figure 5-15 Geometric AoA at mid-upstroke (α_u) and mid-downstroke (α_d) of the flexible wing at input current $I = 0.2$.

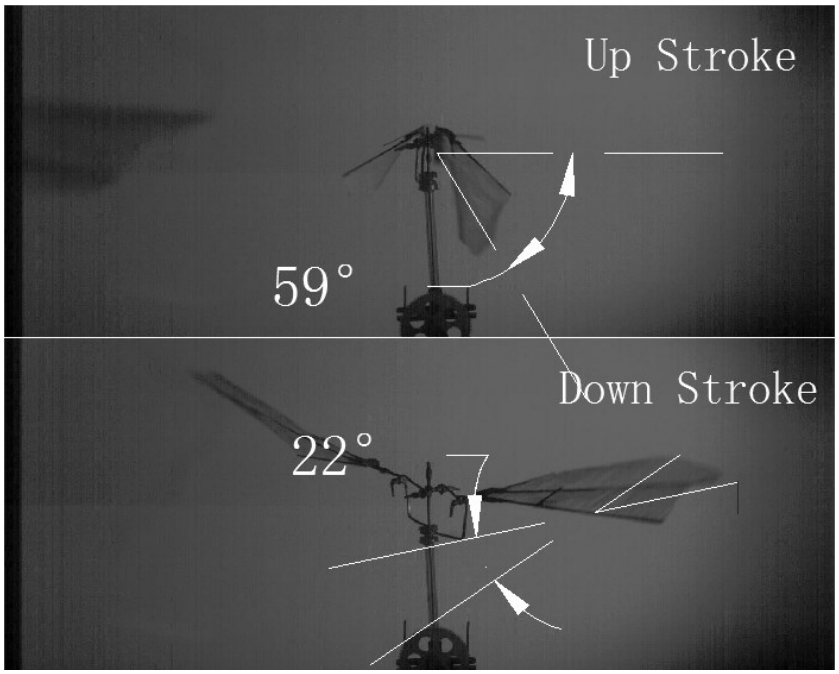

Figure 5-16 Geometric AoA at mid-upstroke (α_u) and mid-downstroke (α_d) of the flexible wing at input current $I = 0.25$.

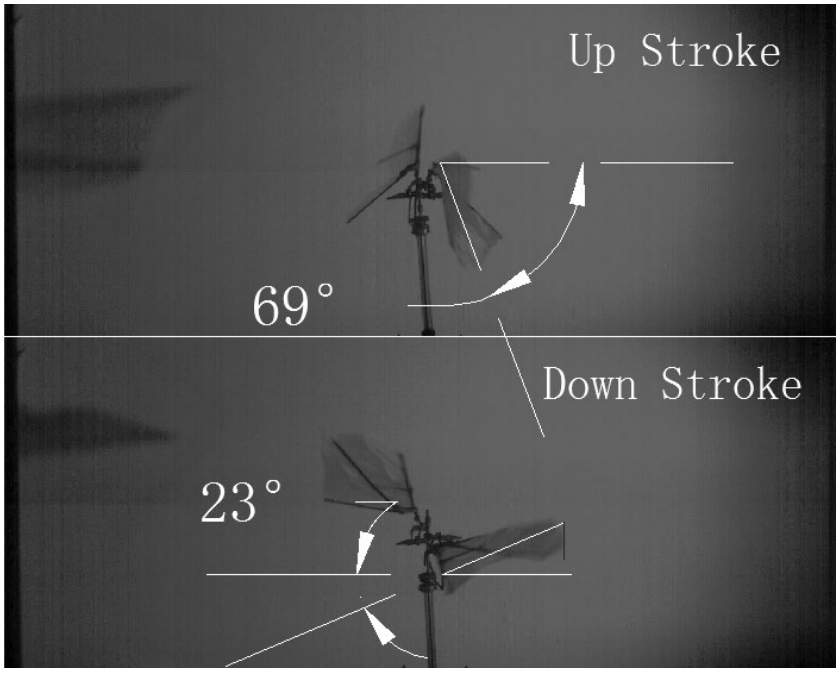

Figure 5-17 Geometric AoA at mid-upstroke (α_u) and mid-downstroke (α_d) of the flexible wing at input current $I = 0.3$.

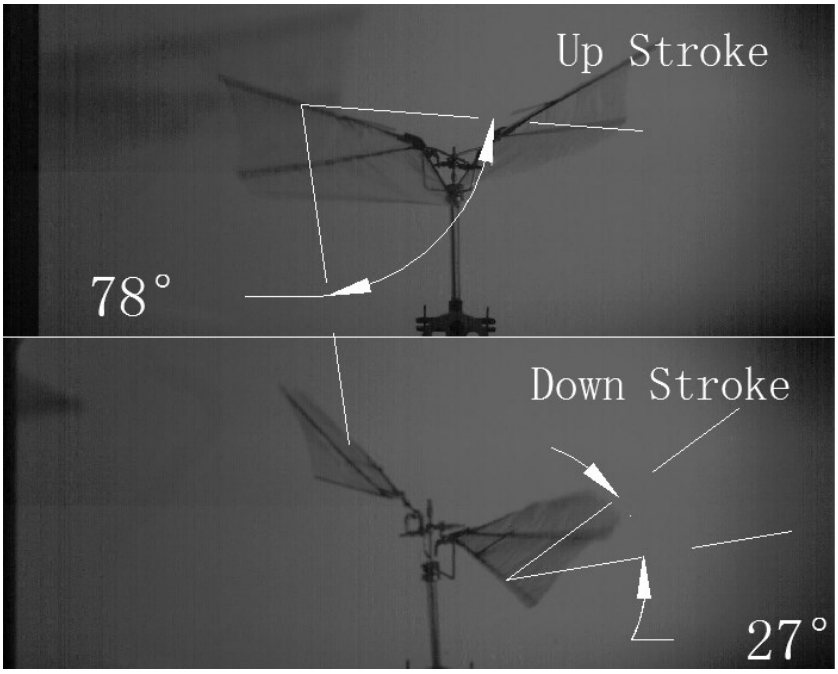

Figure 5-18 Geometric AoA at mid-upstroke (α_u) and mid-downstroke (α_d) of the flexible wing at input current $\mathbf{I = 0.35}$.

5.6 **Discussions**

5.6.1 **Kinematics of wings with different pitching rigidity**

The wing is designed to pitch passively at stroke reversal, with different pitching rigidity, the wing exhibits different pitching kinematics. Therefore, the geometric AoA at upstroke and downstroke changes with this parameter. Since the rotational speed is determined by the flapping frequency and the geometric AoA at upstroke and downstroke (as discussed in chapter 4, at equilibrium state, the dimensionless parameter η, which is the ratio of rotation velocity to mean flapping velocity, see equation (3-47), varies only with the geometric AoA). Therefore, the rotational speed is also determined by the pitching rigidity of the wing. According to the experimental results of the 3 wing with different rigidity, we are able to find the relationship of the output lift and kinematic motion of the FWR wing with respect to the input power. The resultant kinematics of the wing (geometric AoA at mid-upstroke (α_u) and mid-downstroke (α_d), flapping frequency and rotational speed) of different pitching rigidities with respect to the input electric power are shown in Figure 5-19 and Figure 5-20 below.

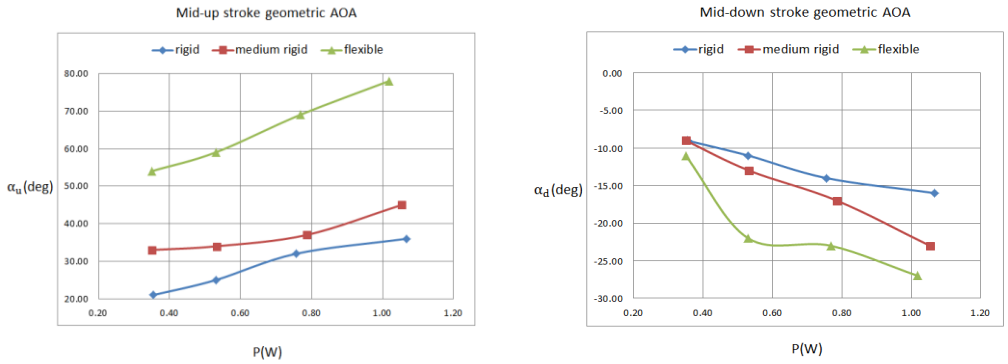

Figure 5-19 The resultant geometric AoA at mid-upstroke (α_u) and mid-downstroke (α_d) of the wings with different pitching rigidities with respect to the input electric power P.

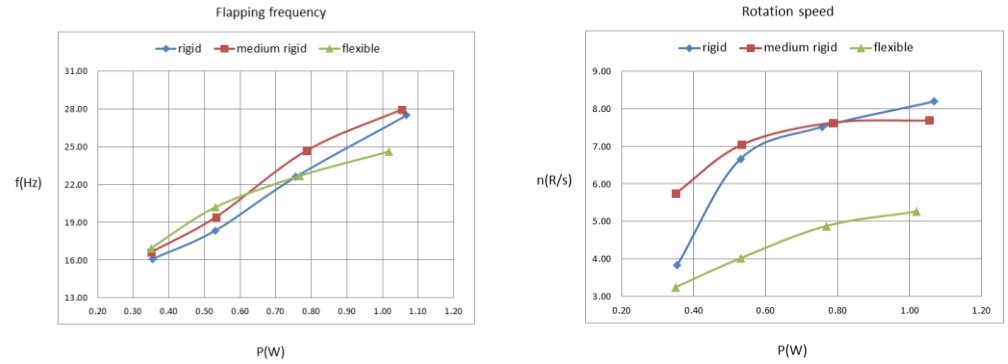

Figure 5-20 The resultant flapping frequency and rotational speed of the wings with different pitching rigidities with respect to the input electric power P.

The magnitude of the geometric AoA increases with the flexibility of the wing, and in the experimental range, has approximately linear relationship with the increase of the input power (except the discrepancy of the most flexible wing at mid-downstroke).

From the experimental results, the flapping frequency is less affected by the variation of the pitching rigidity of the wing. At all 3 cases, the flapping frequency increases linearly with the input power. For rotational speed, the flexible wing has the lowest value at the given experimental cases. The medium rigid wing has higher rotational speed at low input power and lower rotational speed at high input power compared with the rigid wing. This result is consistent with quasi-steady predictions where large upstroke geometric AoA produces

large counter-rotation torque and reduces the rotational speed (see Figure 4-1 and Figure 4-2).

As indicated in chapter 5.4, for the FWR device we used in this experiment, the inertia of the wing and the mechanical device has significant influence on the force measurements and power consumption. We calculated the power consumption of pure aerodynamic force of the wing by giving the measured kinematics with quasi-steady model (described in chapter 3.4), which results in an approximately 2~5% of the aerodynamic power with respect to the total power, and the peak value of the total instantaneous force has much larger value in magnitude than the aerodynamic force, which reduces the accuracy of the measured lift. Since the measured kinematics and forces are dominated by the inertia of the wing and the mechanical system, the accuracy of the measured values are hardly sufficient to be applied for the detailed analysis of the aerodynamic production. However, the general trend of these initial experiments can still give implications on the effect of wing pitching rigidity for lift production. For further studies, it is desirable to use lighter materials for the design of the FWR device for experiments.

5.6.2 **General effect of pitching rigidity for lift production**

For analysing the general effect of the pitching rigidity of the passive pitching wing, the measured mean lift force of wings of different pitching rigidities with respect to the input electric power are shown in Figure 5-21.

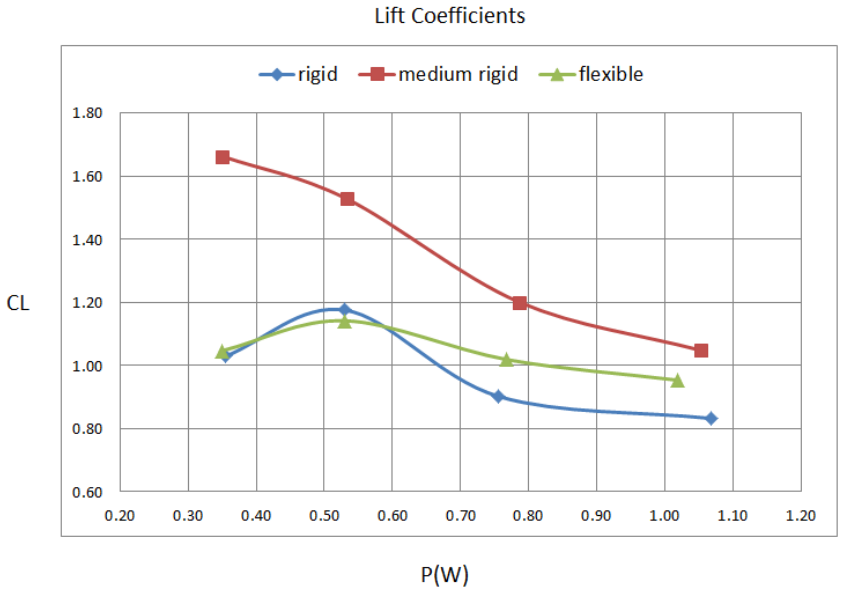

Figure 5-21 The resultant mean lift coefficients of the wings with different pitching rigidities with respect to the input electric power P.

The measured lift force shows that the wing with medium pitching rigidity has the maximum lift force, where the geometric AoA at mid-upstroke is between $33° \sim 45°$, and the geometric AoA at mid-downstroke is between $-9° \sim -23°$ for all the experimental cases, which agree with the quasi-steady predictions (see Figure 4-3).

The passive pitching wing experiments show that the wing can achieve the desired asymmetric pitching motion purely by the interplay of the inertial force of the wing mass and the aerodynamic force. This leads to a simple and integrative design of the wing structure for the FWR MAV.

6 EXPERIMENT-II: A FLYABLE MICRO FWR MAV

6.1 Introduction

In order to demonstrate the FWR design and performance, and also measure the aerodynamic forces and the flight dynamic behaviour, it is desirable to build a flyable FWR model.

Based on the quasi-steady calculations and the experimental results, the lift force can be maximised at medium pitching rigidity and small negative geometric AoA at downstroke and medium geometric AoA at upstroke. Therefore, the pitching dynamics of the model wing is designed to pitch asymmetrically as described above. The first flyable FWR test model (FWR-EX1), is built in our laboratory and performed vertical take off and short time flight. The instantaneous lift force is measured and the dynamic motion of the free flight tests are captured by high speed camera, and presented below.

6.2 Design and Manufacture of the Flyable FWR

A photo of the FWR-EX1 is shown in Figure 6-1. The wings have three degrees of freedom (flapping, rotating about the centroid shaft and passive rotation). To incorporate rotating degree of freedom, a pair of flapping wings is connected in axial symmetry about the centroid shaft through a bearing. An elastic plate is used to connect the bearing and the wings to gain more flapping degree of freedom. The airframe and aeroelastic wings are made of carbon/epoxy composite. A pair of push bars is mounted on the lower bearing which is connected to a DC motor through stiffened carbon/epoxy composite material. The push bars are free rotation about the bearing; the centroid shaft is free to slide vertically about the bearing. The reciprocating wing strokes are realized through a crank-slider mechanism connected to the shaft.

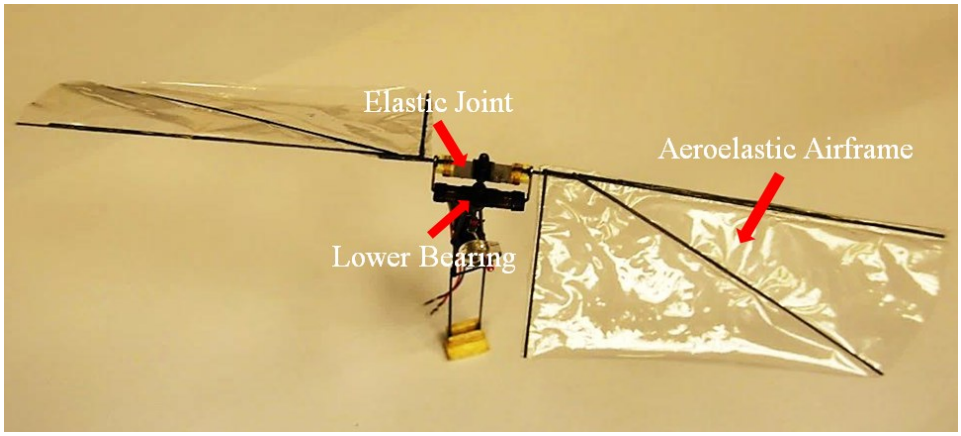

Figure 6-1 The flyable model FWR micro air vehicle (FWR-EX1).

The parameters of FWR-EX1 is shown in Table 6-1 below. The flapping amplitude Φ of FWR-EX1 is acquired from images of high speed camera sequences. The flyable flapping and rotation frequency is decided by the critical frequency that the lift generated is larger than the total weight of the model (from experimental data).

Table 6-1 The parameters of FWR-EX1.

Parameters of FWR-EX1	
Wingspan(cm)	21
Total weight(gm)	2.6
Flapping amplitude(degree)	33~42
Flyable flapping frequency(Hz)	19~24
Flyable rotation frequency(Hz)	6~9

6.2.1 **General sizing and mass breakdown**

The general design of the FWR model is shown in Figure 6-2 below. The FWR model can be decomposed to 4 parts: Wing, Body, DC Motor and Support Bar. The sizing and weight of each of the parts are shown in Table 6-2 below.

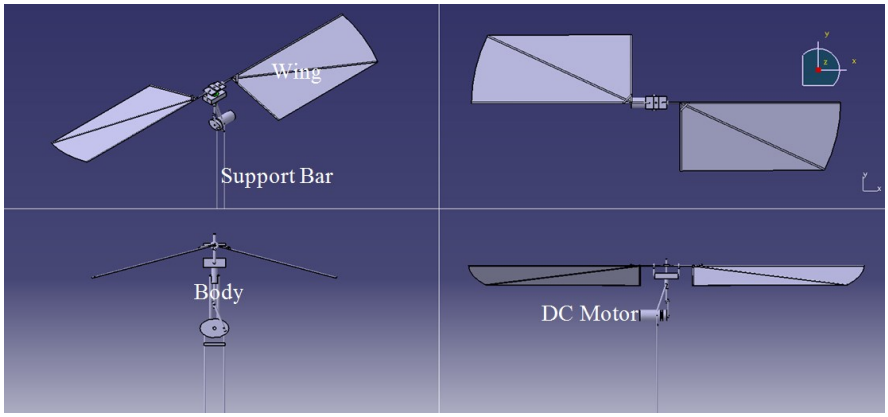

Figure 6-2 The isometric, top, side and front view of the general design of FWR-EX1.

Table 6-2 Sizing and weight of FWR EX1 by parts.

Parts of FWR EX1	Sizing (mm)	Weight (g)
Wing (Single)	105×33	0.15
Body	$25 \times 14 \times 7$	0.95
DC Motor	14 (Radius 3)	1.15
Support Bar (Single)	50 (Radius 0.25)	0.1

The general sizing and mass distribution of the FWR model is decided by material property and the power capability of the DC motor. The main target for the design is to keep the model in the range of micro scale and able to provide enough lift for flight, therefore, the minimum weight of the whole model is desirable. For consideration of the motor power, the simplest mechanical system is required in order to reduce the friction consumption of hinges. Also,

the wing should be as light as possible, since the inertia of the wing mass will also cost extra power to the motor.

6.2.2 **Mechanical system design**

The mechanical system design of the FWR model is shown in Figure 6-3. The mechanical system of the FWR model uses a simple crank-slider mechanism. The rotation of the crank is transformed to the up and down flapping motion of the wing beam.

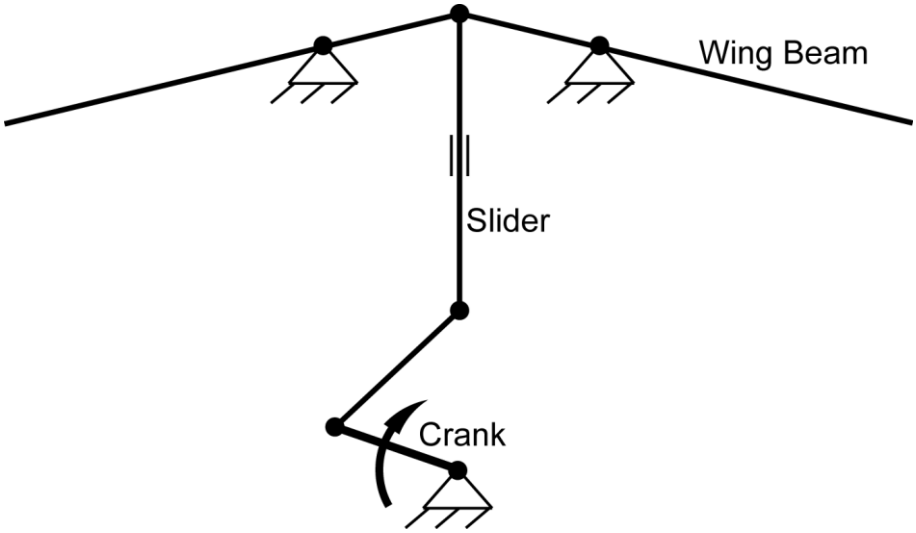

Figure 6-3 Mechanical system design of the FWR model. Slider moves only up and downdard, the DC Motor provides the rotation of the crank.

The chosed mechanical system is based on the principle of simplest and integrative design to transmit the circular motion of the DC motor to the horizontal up and down motion of the wing beam.

6.2.3 **Wing design**

The wing is designed with the same shape parameters with the wing for passive pitching experiments (see Figure 5-1 and Table 5-1). For the flyable model, the pitching rigidity of the wing is fixed to medium rigidity, which is best for the lift production according to the experiments in chapter 5. Therefore, the elastic rubber which is used for ajusting pitching rigidity is removed. The spar and rib are directly attached on the main beam. Since the magnitude of the aerodynamic force is generated at the outer wing location, where the wing has

larger translational velocity, therefore, the rigidity of the spar has largest effect on the pitching of the wing.

In order to reduce weight, we also removed the stop bar, and used an alternative way to create the asymmetric pitching motion. When mounted on the model, the wing is pre-set to a positive geometric AoA, since the wing has same pitching rigidity at upstroke and downstroke, the wing is free to pitch upwards and downwards at either upstroke or downstroke. Due to the pre-set geometric AoA, the resultant pitching motion become asymmetric at each stroke.

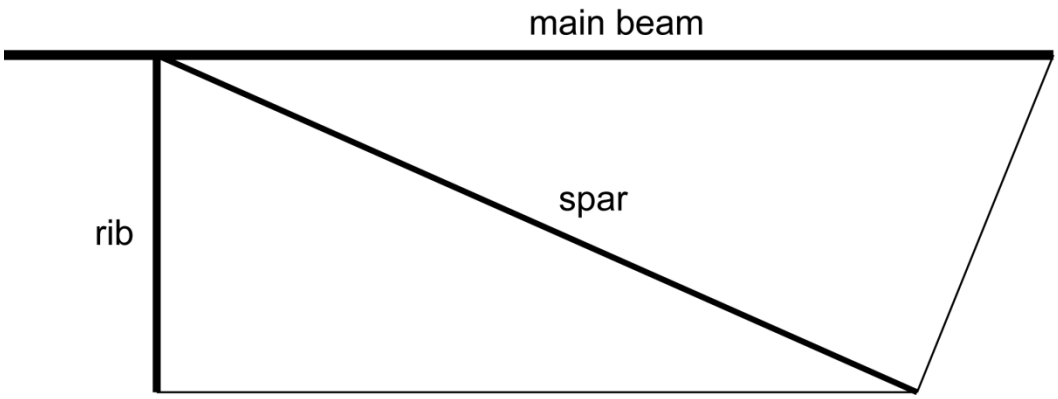

Figure 6-4 Design concepts of the flyable FWR wing.

The wing is supported by a main beam, a spar and a rib. The asymmetric pitching motion is realised by pre-setting a positive geometric AoA when mounted on the FWR model.

The resultant pitching motion of the wing is captured by high speed camera sequences. Figure 6-5 shows the typical pitching of the wing at up and downstroke, respectivelly.

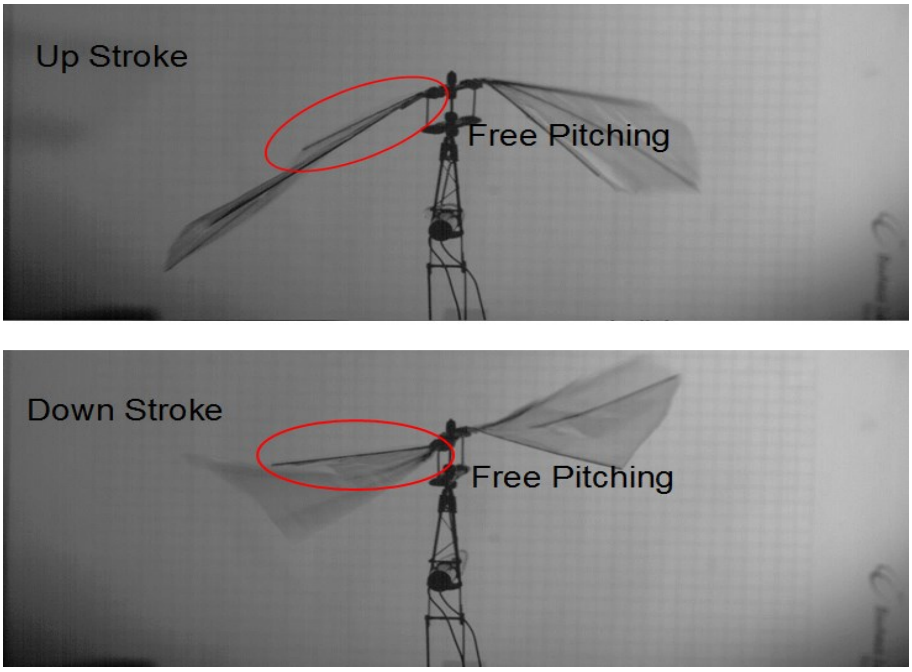

Figure 6-5 The resultant pitching motion of the flyable FWR wing.

6.2.4 **Materials of components**

The materials of the FWR EX1 used mainly include: carbon/epoxy composite, plastic and metal. The airframe and aeroelastic wings are made of carbon/epoxy rods and thin plastic films; the cnetre shaft of the body and the push bars are made of metallic rods; the elastically deformable jionts at the wing roots are made of thin plastic chips; the support bars are also made of carbon/epoxy rods. The Materials of components are shown in Figure 6-6 below. The thin plastic film, deformable plastic chip, metallic rods, DC motor and carbon/epoxy composite rods are shown for the corresponding components of the FWR model.

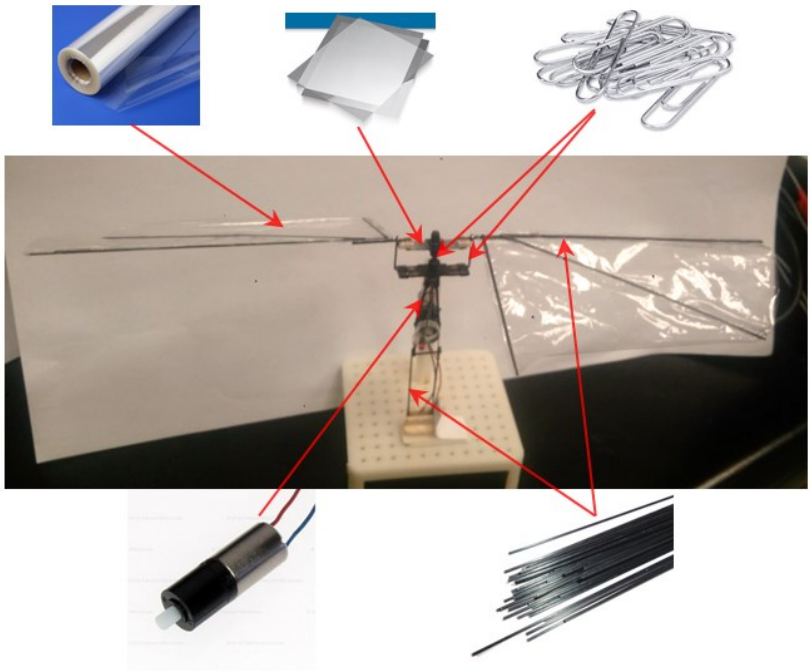

Figure 6-6 Materials of components of FWR EX1.

6.3 Model Tests and Experiments

6.3.1 Static tests of lift production

The instantaneous lift and wing kinematics of the flyable model are measured by static tests. The experimental setup and methods are the same as the passive pitching experiments in chapter 5 (see 5.3 and 5.4). We measured the lift production of the flyable model at different applied voltage of 1.99V, 2.5V, 2.99V, 3.5V, 3.99V and 4.49V, respectively.

6.3.2 Initial flight tests of FWR-EX1

To demonstrate the FWR concept feasibility and for further analyses of the flight dynamics behaviour of this configuration, the vertical take-off and short time hovering flight of the FWR-EX1 is performed and the dynamic motions of the initial flight are captured by high speed camera.

6.4 **Results**

6.4.1 **Lift production**

Table 6-3 Lift production of the flyable FWR model (FWR-EX1), input voltage $\mathbf{U = 1.99, 2.5, 2.99, 3.5}$, $\mathbf{3.99}$ and $\mathbf{4.59}$ V.

Input voltage	U(V)	1.99	2.50	2.99	3.50	3.99	4.49
Input power	P(W)	0.08	0.13	0.18	0.23	0.28	0.34
Flapping amplitude	Φ(deg.)	37.00	35.00	39.00	36.00	41.00	35.00
Mid-upstroke AoA	α_u(deg)	35.00	38.00	40.00	39.00	40.00	41.00
Mid-downstroke AoA	α_d(deg)	9.00	7.00	-4.00	-10.00	-18.00	-22.00
Flapping frequency	f(Hz)	10.00	11.42	14.01	19.31	21.79	24.10
Rotation speed	n(R/s)	1.97	2.78	4.57	6.21	7.81	8.93
Average lift	L(g)	0.80	1.17	1.74	2.40	2.72	2.97
Mean lift coefficient	$\bar{C}_L$	1.00	1.26	1.00	0.86	0.59	0.72

The kinematic parameters and instantaneous lift force from high speed camera sequences of each experimental case are presented below.

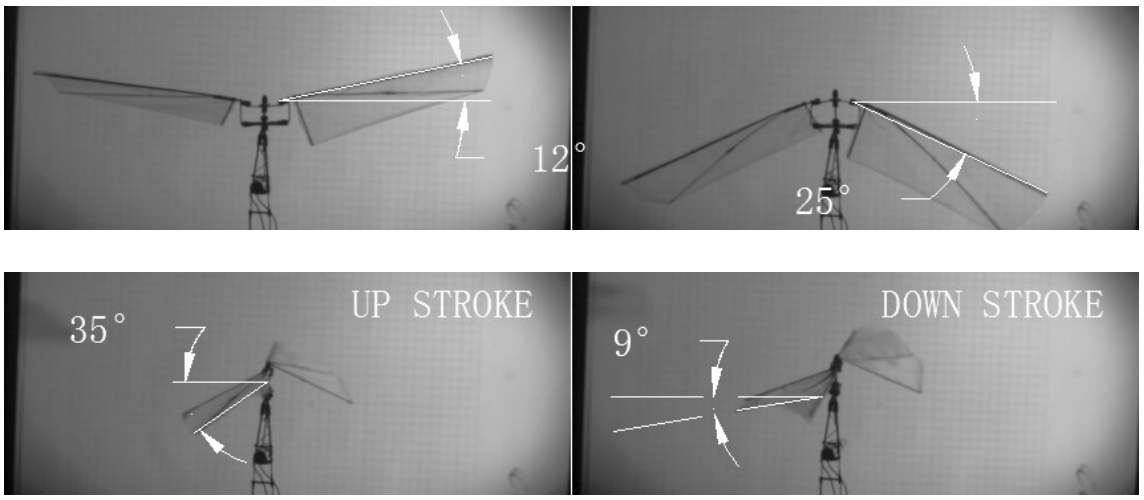

Figure 6-7 Flapping amplitude Φ and geometric AoA at mid-upstroke (α_u) and mid-downstroke (α_d) of FWR-EX1 at input voltage $U = 1.99$ V.

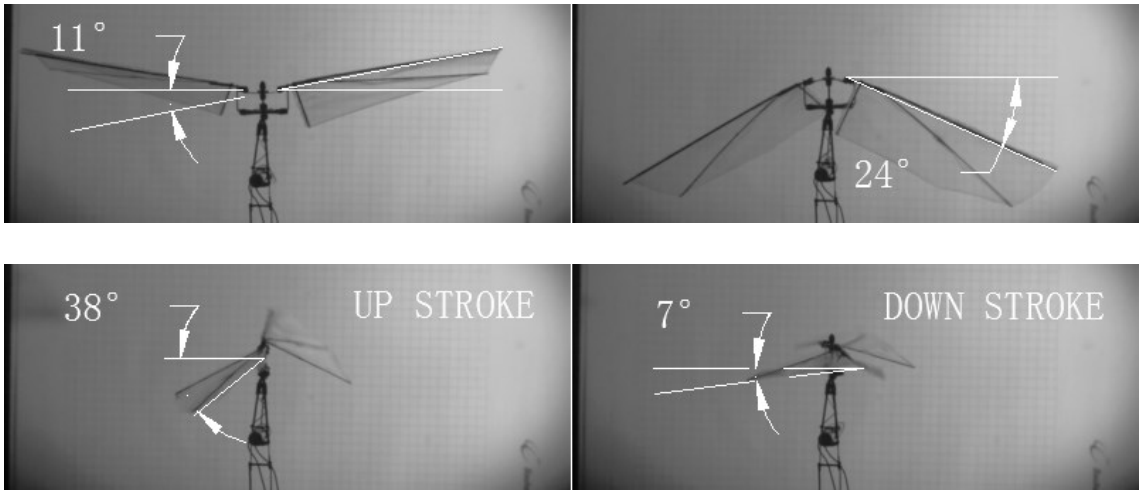

Figure 6-8 Flapping amplitude Φ and geometric AoA at mid-upstroke (α_u) and mid-downstroke (α_d) of FWR-EX1 at input voltage $U = 2.5$ V.

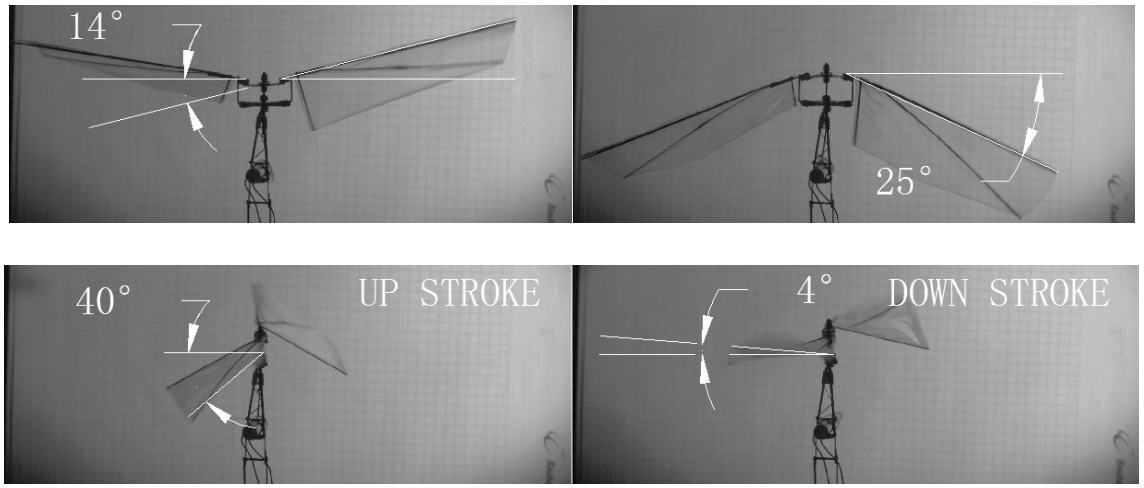

Figure 6-9 Flapping amplitude Φ and geometric AoA at mid-upstroke (α_u) and mid-downstroke (α_d) of FWR-EX1 at input voltage $U = 2.99$ V.

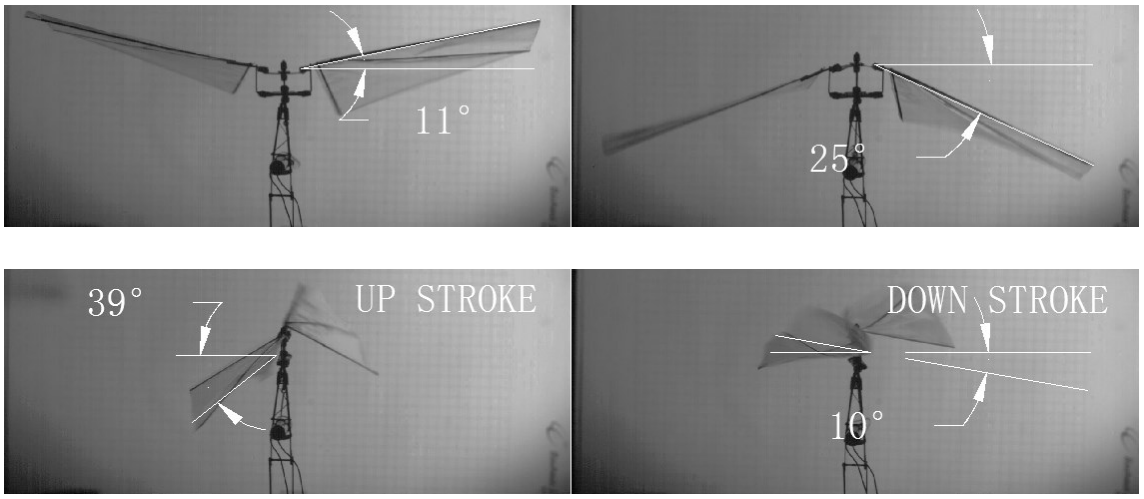

Figure 6-10 Flapping amplitude Φ and geometric AoA at mid-upstroke (α_u) and mid-downstroke (α_d) of FWR-EX1 at input voltage $U = 3.5$ V.

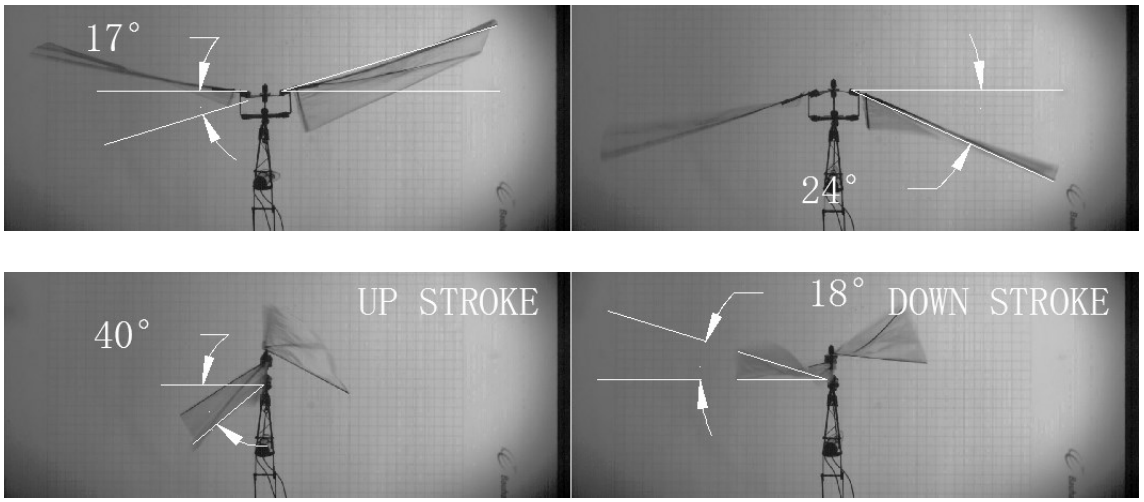

Figure 6-11 Flapping amplitude Φ and geometric AoA at mid-upstroke (α_u) and mid-downstroke (α_d) of FWR-EX1 at input voltage $U = 3.99$ V.

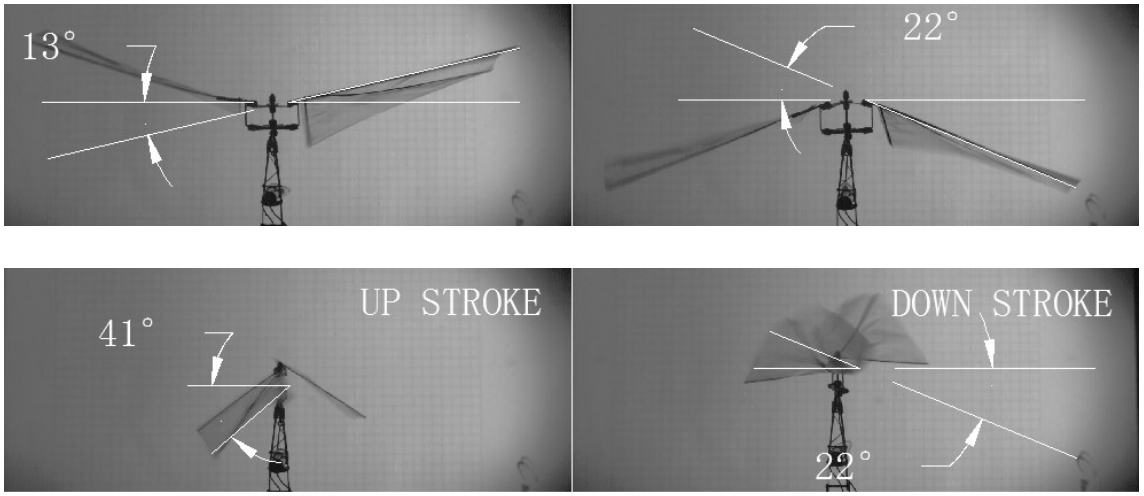

Figure 6-12 Flapping amplitude Φ and geometric AoA at mid-upstroke (α_u) and mid-downstroke (α_d) of FWR-EX1 at input voltage $U = 4.49$ V.

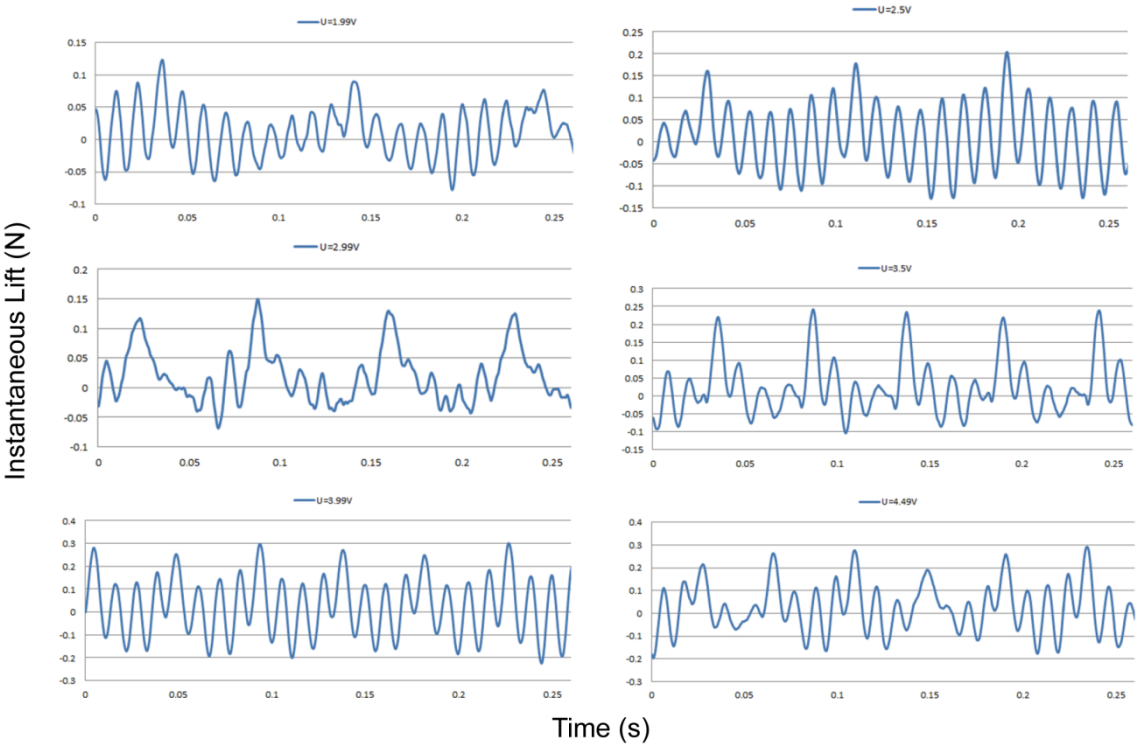

Figure 6-13 Instantaneous lift force of FWR-EX1 at input voltage $\mathbf{U = 1.99,\ 2.5,\ 2.99,\ 3.5,\ 3.99,\ 4.49}$ V, respectively.

6.4.2 **Initial flight of FWR MAV**

We captured the dynamic motion of the take-off and short time hovering of the flyable model (FWR-EX1) using high speed camera. The flight sequences (see Figure 6-14 below) of FWR-EX1 show a self-balanced rotating motion, which contributes to a stabilized flight due to the gyroscopic effect of this configuration (further studies are needed on this topic).

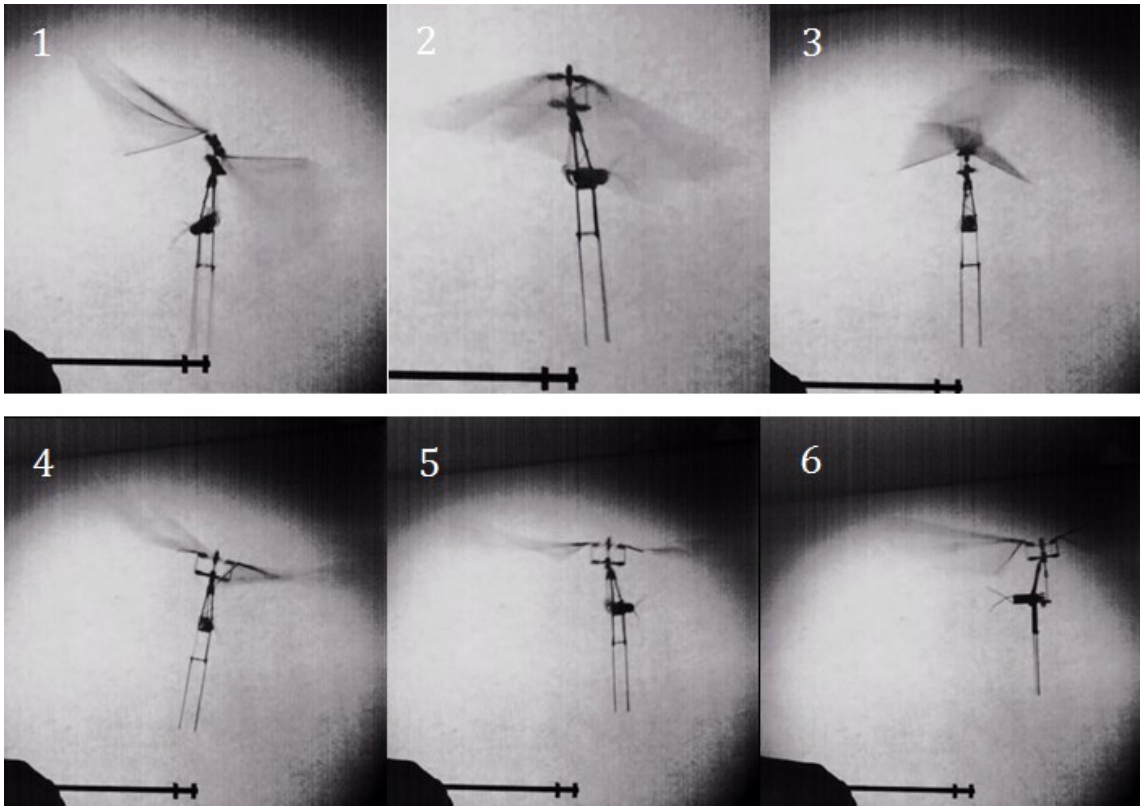

Figure 6-14 Initial free flight sequences of the model FWR micro air vehicle (FWR-EX1) shot by high speed camera. A self-balanced stabilized rotating motion is observed. (See video: http://youtu.be/BhUenPdMtm8).

6.5 **Discussions**

6.5.1 **Quasi-steady VS experimental results**

We compared the experimental results of the mean lift forces and coefficients at different input power with the quasi-steady estimations, the results are shown in Figure 6-15 below.

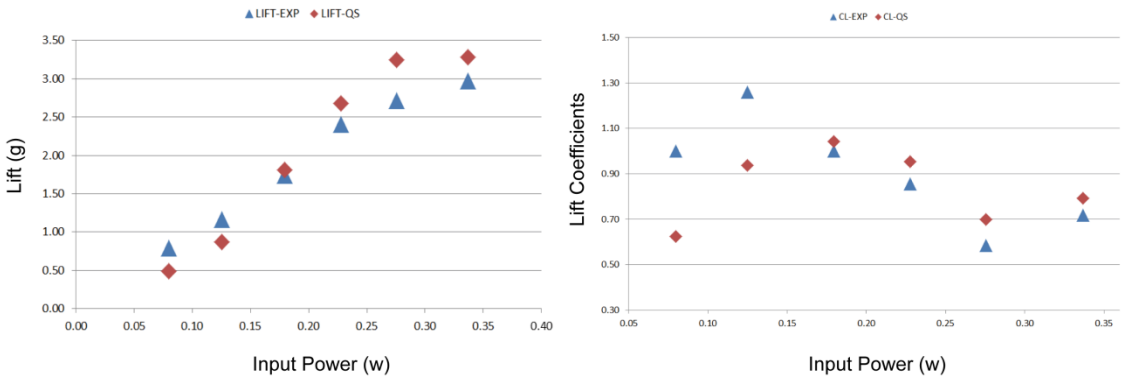

Figure 6-15 Quasi-steady estimations (red diamonds) VS experimental results (blue triangles) of the mean lift forces (left) and coefficients (right).

For the comparisons of the mean lift force, the predictions of the quasi-steady aerodynamic model show very good agreement with experimental results; for the comparisons of the mean lift coefficients, the predicted value of the quasi-steady aerodynamic model show good agreement with experimental results at input power P>0.18. The discrepancies occur at input power P<0.18, where quasi-steady predictions are smaller in magnitude than experimental results. This may be due to the inadequate accuracies of the measured kinematics of the wing. For the flapping amplitudes and the geometric AoAs are all obtained by measuring the planar angles captured by one high speed camera, which are approximations of the 'real' angles defined by 3D Euler angles.

Also, the power consumption due to the aerodynamic force is calculated using the quasi-steady model. The portions of the pure aerodynamic power to the total power at different flapping frequencies are shown in Figure 6-16 below.

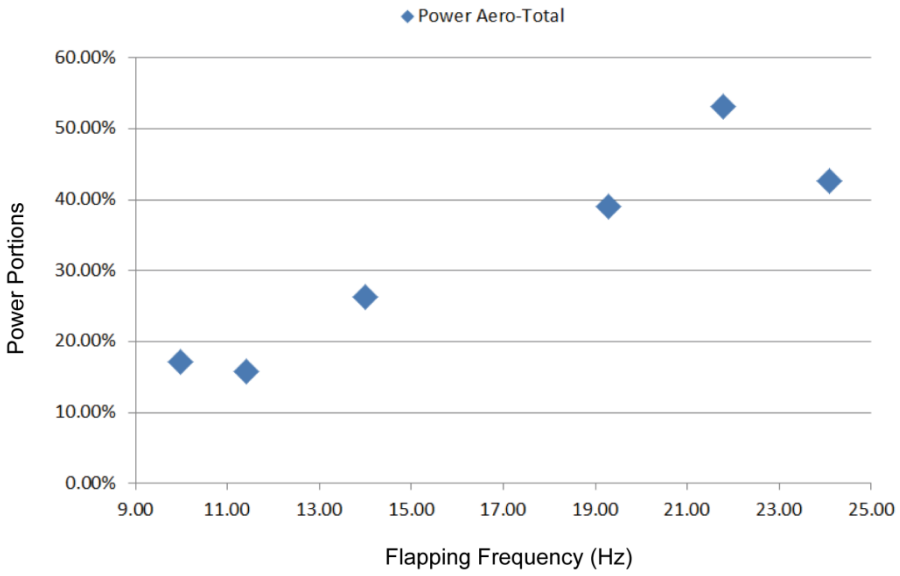

Figure 6-16 The portions of the pure aerodynamic power to the total power at different flapping frequencies.

In Fig. 6-21, horizontal axis indicates the flapping frequencies f, vertical axis indicates the percentage of the pure aerodynamic power to the total power.

The portions of the pure aerodynamic power to the total power increases as the flapping frequency increases, and range between 16%~53% at the given experimental cases. This result shows good energy transformation of the input electric power to the output aerodynamic power of the mechanical system.

It shall be noted that the lift coefficients and the aerodynamic power calculated by the quasi-steady model is by the assumption that the wings are rigid flat plates, and no deformation is taken into account. Since the flexibility of the wing will change the aerodynamic force production and power consumption, the validity of the above comparisons will depend on the effect of wing flexibility. However, for the purpose of initial analysing and evaluation, they serve as good approximations. The effect of flexibility of the FWR wing is discussed in the next chapter.

6.5.2 **The general effect of flexibility of FWR wing**

The aerodynamic force production of a MAV depends on several physical factors, which mainly include the wing kinematics, the wing mophology and the

fluid enviroument around the wing. For micro FWR and insect-like flapping wing, the wing exhibits large acceleration for the reciprocating flapping motion, the flow around the wing has strong time-dependent unsteady mechanism. Also, the large acceleration causes a deformation of the wing due to wing inertia and the fluid force, which changes the mophological properties of the wing, and therefore, changes the fluid force generation. The problem is interpreted as the solid-fluid interaction, which has been widely studied for insect flight[42; 52-55].

The effect of the flexibility of FWR wing can be analysed numerically. For the numerical investigation, the problem is computationally intensive since the numerical model must ensure the solution converges at every time step for both structure and fluid[54]. However, the general effect of wing flexibility can be studied analylitically.

Compared with rigid wing, the flexible wing under inertia and aerodynamic loading will deform, therefore, the geometric relationship of the force vector will change with the deformation of the wing. This can be shown in Figure 6-17 below.

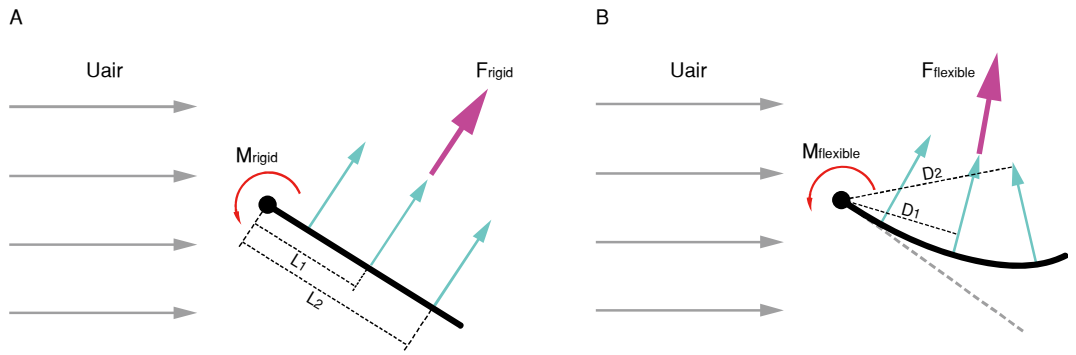

Figure 6-17 The geometric relationship of the force vectors and moments on a 2D wing chord of the rigid wing (a) and flexible wing (b).

In Figure 6-18, the typical fluid force vectors at different chord-wise location (L1 and L2) are indicated by blue arrows; total fluid force vectors are indicated by purple arrows; the pitching moments of the 2D wing chords are indicated by red

arrows. D1 and D2 in Fig. 6-22b indicate the moment arms of the corresponding force vectors on the deformed wing chord.

According to the 'normal force relationship' (see chapter 4, references[22; 32]), the local fluid force vector acts perpendicular to the tangent of the local curvature of the 2D wing chord (as shown in Figure 6-17 above). Due to the flexibility of the wing, the 2D wing chord is deformed as a negative camber. Therefore, the directions of the local force vectors at L1 and L2 are changed counter-clockwisely, which reduce the moment arms of the force vectors to D1 and D2 (see Figure 6-17 B). Therefore, the resultant pitching moment is reduced. Also, the direction of the total fluid force vector is changed counter-clockwisely as shown in Figure 6-17 B. For the span-wise deformation, the above analyses also applies, which indicates that span-wise deformation will reduce the required moment for driving the flapping motion, and change the direction of the resultant force vector compared with rigid wing.

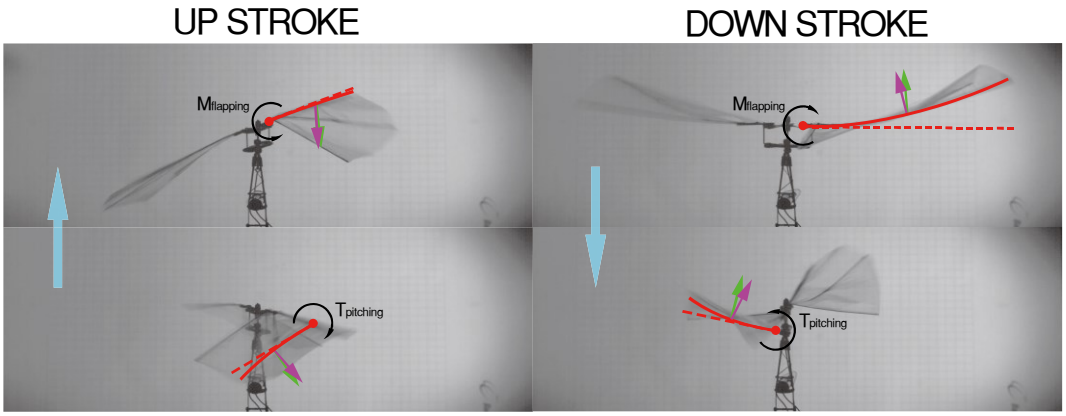

Figure 6-19 The span-wise and chord-wise deformations of the wing at upstroke and downstroke.

In the Figure, the wing camber and chord shape are highlighted by red lines; the undeformed shape (assume the wing is rigid) is indicated by red dotted lines; the resultant force vectors of the deformed wing and undeformed wing are indicated by purple arrows and green arrows, respectively; the flapping drive moments ($M_{flapping}$) and reaction torques ($T_{pitching}$) of the passive pitching wing are shown as black arrows.

As shown in Figure 6-19 above, at downstroke, the large aerodynamic force causes the wing bending and twist upward, which reduces the drive moment for flapping and the reaction troque of the passive pitching of the wing. At upstroke, since the aerodynamic force is small in magnitude due to the small effective AoA α_e (see Figure 4-1), the bending and twist deformations of the wing are small. The reduced drive moment reduces the required power for the flapping motion, which is beneficial for energy efficiency. Also, since the deformation of the wing is sensitive to the force production (a larger generated force will cause larger deformation, thus, further reduces the drive moment), therefore, the flexible wing will 'smooth' the peak of the drive moment and power profile, which is beneficial for the actuator and power system.

For more detailed effects of the flexibility of the wing on the aerodynamic force and wing kinematics, numerical analyses that couple both the fluid dynamics and structure dynamics should be applied.

7 INITIAL DESIGN & TESTS OF A RESONANT THORAX MECHANISM

7.1 Introduction

The thorax of an insect during flight is an oscillating system with high elasticity. At the end of each stroke, the kinetic energy of the wings is stored as elastic potential energy in the walls of the thorax, which is released during the subsequent stroke[48]. Both thorax and wings are resonant structures, storing energy elastically, and tuned to deform appropriately at their operating frequencies[56]. For biomimetic micro flying robots, this cyclic energy storage is desirable for energy efficiency. Sitti[57] proposed a simple piezoelectrically actuated four-bar mechanism for flying robots design (see Figure 7-1 below). It is shown that beneficial mechanical efficiency and large flapping amplitude can be reached at resonant state of the mechanism.

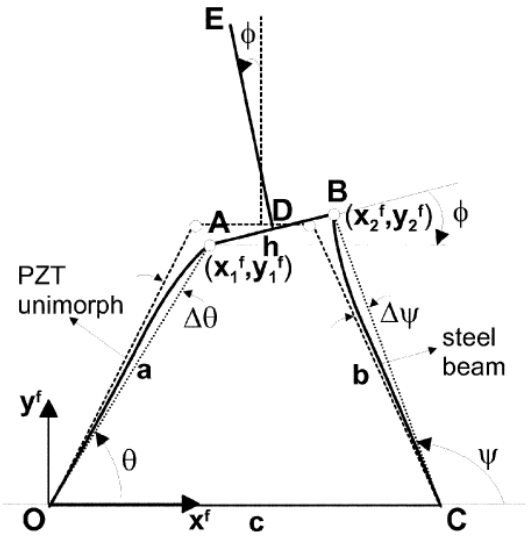

Figure 7-1 Four-bar mechanism with two elastic beams (Reproduced from[57]).

The current design of the flyable model (FWR-EX1, described in chapter 6) uses DC motor as actuator, and the mechanical system was designed to transform the rotation motion of the motor into linear motion. The transformation mechanism thus causes extra power consumption and increases weight. Therefore, alternative design concept that uses linear actuator and resonant

oscillating mechanisms of the mechanical system needs to be further investigated.

This chapter presents the initial design and demonstration of a simple resonant amplification mechanism for FWR that is suitable for small linear actuator assemblage. This light weight and simple mechanism serves as an alternative biomimetically efficient solution for further designs and investigations of micro robotic flyers.

7.2 **A 5-bar Mechanical Thorax Design**

For the application of the FWR MAV, we designed a 5-bar mechanical thorax with two elastically deformable bars in the centre (see Figure 7-2).

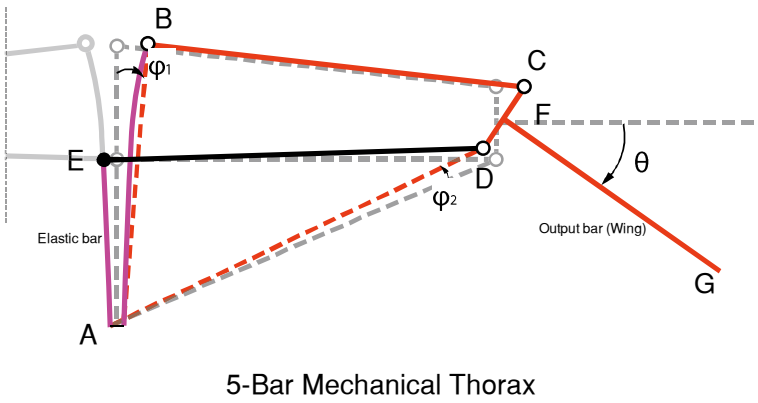

Figure 7-2 The 5-bar amplification mechanical thorax.

In the figure, Bar AB and AE are the actuator bars and are elastically deformable. Point B, C and D are connected by hinge joints; point E is solid joint. The design can be simplified by a 5-bar linkage mechanism (shown in red colour). For given small input displacements $\boldsymbol{\varphi_1}$ and $\boldsymbol{\varphi_2}$, the output motion is amplified to $\boldsymbol{\theta}$.

The mechanical thorax has symmetric structure layout for left and right wing; two actuator bars are in the centre, which is especially suitable for the FWR configuration to be mounted on the rotational shaft. Compared with the previously proposed 4-bar mechanism[57] (see Figure 7-1), the symmetric

layout of the current design allows the motion of the two actuator bars to be transmitted to both left and right wings. Therefore, with the same number of actuators (two for two wings) and input displacements, the current mechanism design will yield much larger output motion.

The 5-bar mechanism is designed to amplify the input motion with large amplification ratio, and is suitable for linear actuator with small input displacement (such as piezoelectric actuator). The elastic actuator bars serve as energy storage for the kinetic energy of the mechanical system. At resonant oscillation, this mechanism provides large amplitude flapping motion with maximized energy efficiency.

7.2.1 **Geometric relation**

The 5-bar mechanism can be simplified by a rigid linkage system for analysing the geometric relation of the input motion and output motion. The simplified rigid linkage system is shown in Figure 7-3 below.

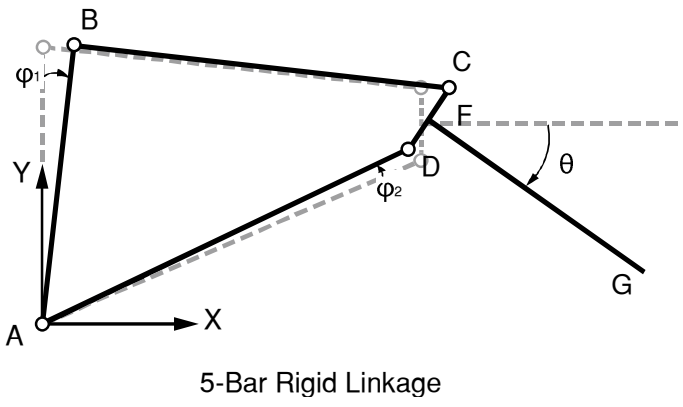

Figure 7-3 Simplified five-bar rigid linkage and planar coordinate system.

In the planar coordinate system, the geometric relation of the rigid linkage can be expressed by the following vectorial equation:

$$\mathbf{AB} + \mathbf{BC} + \mathbf{CD} + \mathbf{DA} = \mathbf{0} \qquad \textbf{(7-1)}$$

If we assume the initial position ($\mathrm{t} = 0$) of the above vectors are r_1, r_2, r_3 and r_4, respectively. At time t, the actuator bars AB and DA are rotated by angles φ_1

and φ_2, and the link BC and CD are therefore rotated by angles θ_1 and θ_2, respectively. Since the output bar DG is solidly connected to the link CD, therefore, the output angle θ equals to the angle that link CD is rotated (θ_2). By the above definitions, the geometric relation can be expressed by the following equation:

$$\mathbf{R}[\boldsymbol{\varphi_1}(\mathbf{t})] \cdot \mathbf{r_1} + \mathbf{R}[\boldsymbol{\theta_1}(\mathbf{t})] \cdot \mathbf{r_2} + \mathbf{R}[\boldsymbol{\theta_2}(\mathbf{t})] \cdot \mathbf{r_3} + \mathbf{R}[\boldsymbol{\varphi_2}(\mathbf{t})] \cdot \mathbf{r_4} = \mathbf{0} \quad \textbf{(7-2)}$$

Where the rotation matrix for bar AB at time t is written as (same for BC, CD and DA):

$$\mathbf{R}[\boldsymbol{\varphi_1}(\mathbf{t})] = \begin{bmatrix} cos[\varphi_1(t)] & -sin[\varphi_1(t)] \\ sin[\varphi_1(t)] & cos[\varphi_1(t)] \end{bmatrix} \quad \textbf{(7-3)}$$

Thus, by giving the initial vectors r_1, r_2, r_3 and r_4 and the input angles at a given time t ($\varphi_1(t)$ and $\varphi_2(t)$), the unknowns in the vectorial equation (7-2) is only $\theta_1(\mathrm{t})$ and $\theta_2(\mathrm{t})$, the output angle $\theta(\mathrm{t}) = \theta_2(\mathrm{t})$ can then be solved.

7.2.2 **Optimization of amplification ratio**

The amplification ratio of the mechanism λ is defined as the ratio of output angle to the input angular displacements, which can be written as:

$$\lambda = {}^{\theta}/_{\sum_{i=0}^{n} \varphi_i} \quad \textbf{(7-4)}$$

Where the angle φ_i refers to the ith input of the system. For the current design, the total number of input motion n equals to 2.

7.2.2.1 **Optimization method**

To find the maximum amplification ratio of the mechanism, multi-dimensional optimization procedure regarding the initial vectors r_1, r_2, r_3 and r_4 is needed. Each vector carries 2 geometric properties, the length and the direction (initial angle of the link). The basic constraint condition is the compliant linkage of the system at initial state ($\mathrm{t} = 0$):

$$\mathbf{r_1} + \mathbf{r_2} + \mathbf{r_3} + \mathbf{r_4} = \mathbf{0} \quad \textbf{(7-5)}$$

From the above equation, for any given vectors r_1, r_2 and r_3, the vector r_4 is a known vector. Therefore, the optimization space has together 6-dimensions.

In order to simplify the calculation, at the current stage, we fix some of the variables according to the sizing and dimension of the FWR. Specifically, the length and the initial angle of the actuator bar AB, the length of the link BC and the length of the link CD. These extra constraints are given as:

$$\begin{cases} \mathbf{r_1} = (0{,}100) \\ \|\mathbf{r_2}\| = 30 \\ \|\mathbf{r_3}\| = 10 \end{cases} \tag{7-6}$$

By applying the above constraints, the optimization space becomes 2-dimensional: the initial angles of $\mathbf{r_2}$ and $\mathbf{r_3}$. Here, we express these two parameters as ε and ϵ, respectively (positive anticlockwise, see Figure 7-4 below).

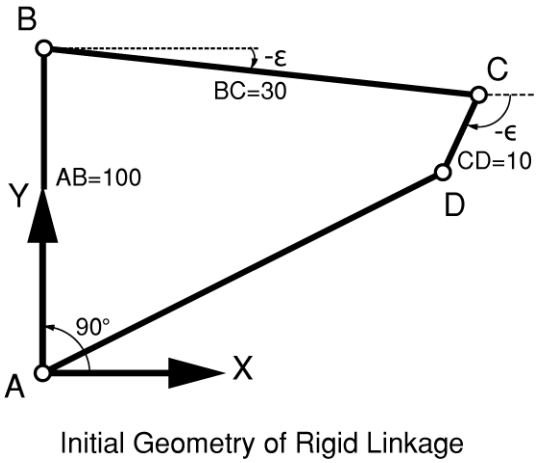

Figure 7-4 Initial geometry of the rigid linkage system under given constraints.

The function (7-2) can therefore be treated as an implicit function:

$$f(\mathbf{x}, \theta) = 0 \tag{7-7}$$

Where the variable $\mathbf{x} = (\varepsilon, \epsilon)$ represents the initial angles of link BC and link CD, and $\theta = \theta_2$ is the output angle. Since f is continuously differentiable, by the implicit function theorem, for any point that satisfies the condition: $\frac{\partial f}{\partial \theta} \neq 0$, there exists an equivalent function g that maps the vector $\mathbf{x}$ to θ:

$$g: \mathbf{x} \rightarrow \theta \tag{7-8}$$

Therefore, the optimization target is to find the local maxima of the function $g(\mathbf{x})$ for given φ_1 and φ_2. We used a simple gradient method to find the optimized output angle θ, the convergence sequence is then written as:

$$\mathbf{x_{n+1}} = \mathbf{x_n} + \gamma_n \mathbf{J_g}(\mathbf{x_n}),\ n \geq 0 \tag{7-9}$$

Where $\mathbf{J_g}(\mathbf{x})$ is the Jacobian matrix of the function $g(\mathbf{x})$:

$$\mathbf{J_g}(\mathbf{x}) = \frac{\partial g(\mathbf{x})}{\partial \mathbf{x}} = \left[\frac{\partial \theta}{\partial \varepsilon}, \frac{\partial \theta}{\partial \epsilon}\right] \tag{7-10}$$

The Jacobian matrix is solved numerically. To assure convergence of the numerical optimization, the initial value of the factor γ_n is chosen as unity at each time step n, and decreases as $\gamma_{n,k} = \frac{1}{2^{k-1}}\ (k = 1, 2, 3 \ldots)$ until $\mathbf{F}(\mathbf{x_{n+1}})|_k > \mathbf{F}(\mathbf{x_n})|_k$ for each time step.

7.2.2.2 **Optimization results**

For the initial optimization, we consider the motion of the left wing and the right wing of the FWR is symmetric. Therefore, the input motion of bar AB and DA is also symmetric ($\varphi_1 = -\varphi_2$, see Figure 7-2). The optimized initial geometries and amplification ratios at different input angular displacements are shown in Table 7-1 below.

Table 7-1 The optimized initial geometries (ε and ϵ) and amplification ratios (λ) at different input angular displacement ($\varphi = |\varphi_1| + |\varphi_2|$).

Input angular displacement	φ (deg.)	2.00	3.00	4.00	5.00	6.00	7.00
Optimized initial angle link BC	ε (deg.)	4.07	3.48	3.10	2.83	2.33	0.20
Optimized initial angle link CD	ϵ(deg.)	-133.0	-123.0	-113.8	-105.0	-96.55	-90.14
Optimized output angle	θ(deg.)	55.92	69.37	81.27	92.34	103.01	113.54
Optimized amplification ratio	λ	27.96	23.12	20.32	18.47	17.17	16.22

The optimized amplification ratio decreases as the input angular displacement increases. Based on the above calculation, the thorax mechanism can then be designed to suit a specific actuator with different inputs and yield desirable output angles with maximum value ranging from $55°$ ~$113°$.

7.3 **Test and Demonstration of a Resonant Oscillating Thorax**

7.3.1 **Design of the demonstration thorax system**

To manufacture the 5-bar linkage mechanism, special treatments shall be used regarding the hinge joints and the materials, since the geometry of the structure, the rigidities of the links and the friction forces at the hinges are all important factors for the dynamic behaviour of the oscillating system.

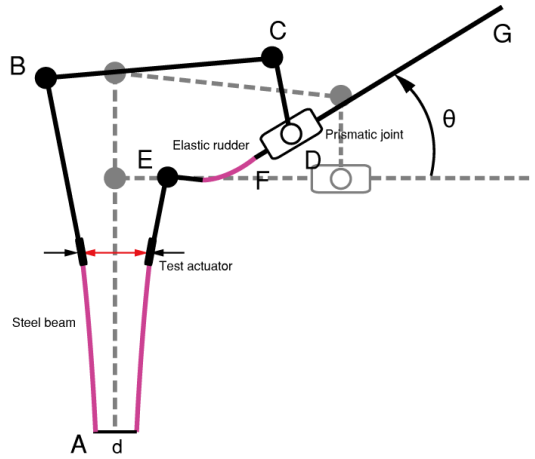

Demontration Mechanism for Resonant Oscillating Thorax

Figure 7-5 Demonstration mechanism for resonant oscillating thorax.

In the above figure, the joint at point B, C and E are solid joints; at point D, a prismatic joint is used that allows 2 degree of freedom (sliding and rotation); an elastic rubber serves as elastic joint at point F allows 1 degree of freedom (rotation). The base of the actuator bars AB and AE are made of steel beams.

For the initial demonstration of the feasibility of the resonant oscillating mechanism for micro mechanical flapper, we designed an alternative resonant oscillation thorax that is easy to be manufactured at small scale. This demonstration mechanism uses rigid joints and prismatic joint instead of hinge joints of the original system (see Figure 7-5 above).

The demonstration system has similar geometric layout with the 5-bar linkage system described in chapter 7.2. The difference here is that we used a prismatic joint (at point D), and an elastic joint (at point F), instead of three hinge joints (at point B, C and D, see Figure 7-2) of the 5-bar linkage system, which is easier for manufacturing at this scale. For the assemblage of the test actuator, the base of the mechanism (point A) is separated with width d.

The dynamic system has together three elastic components: two elastic beams at the base and the elastic joint at point F. We used steel material for the elastic beams and rubber for the elastic joint. Since the rigidity of the steel beams is much larger than the rubber, therefore, the natural frequency of the elastic

beams are much higher than the elastic joint, and the dynamic behaviour of the oscillating system is mainly decided by the elasticity of the rubber at relatively low frequency excitation.

7.3.2 **Manufacture and initial test of the mechanical thorax system**

7.3.2.1 **Manufacture of the test model**

Based on the design described in the previous chapter, we made a test model of the micro oscillating thorax system. The overall structure and materials of the model is shown in Figure 7-6 below.

The manufactured demonstration micro thorax system has a weight of less than 1 gram, and sizing of a coin. We used a geared DC motor and cam system as the linear actuator for the input motion. The test actuator (DC motor) is attached to the bottom of the linkage mechanism. A plastic cam is located in the middle of the two steel beams, and connected with the geared motor with a metal shaft. When the motor rotates, the cam cyclically pushing the two steel beams and therefore excites oscillation of the mechanism.

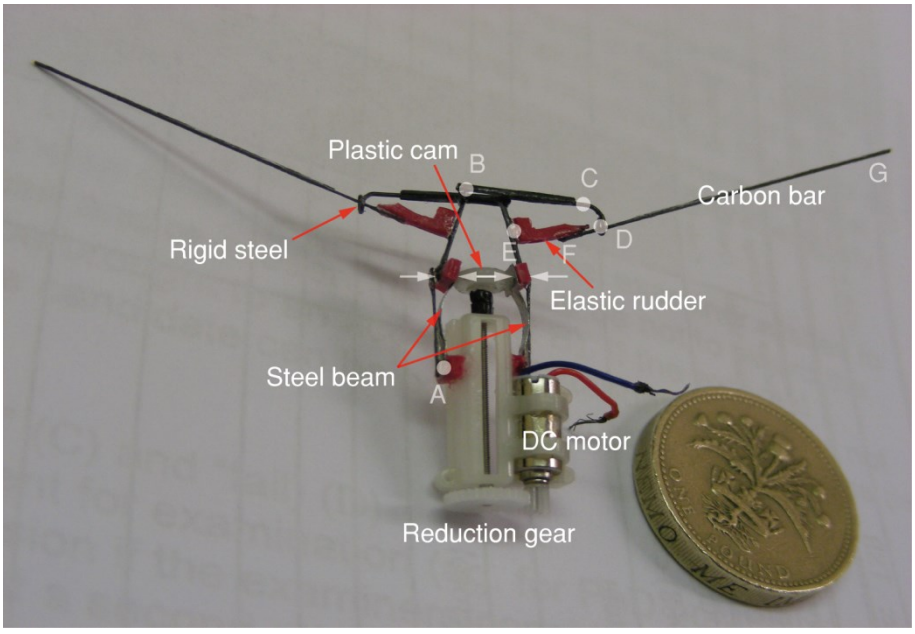

Figure 7-6 Test model of the demonstration micro oscillating thorax system.

The size of the manufactured thorax system has dimension slightly larger than a coin. The transmission links are made of carbon fibre materials; the prismatic

joint is made of rigid steel; and the elastic beams of the actuator bars are made of steel beams; the elastic joint at point F is made of elastic rubber. A DC motor with reduction gear system is attached to the actuator bars, and the plastic cam is used to transmit the rotation motion of the motor into linear motion.

7.3.2.2 **Initial tests of the resonant thorax system**

For the initial test of the dynamic behaviour of the mechanical thorax system, the DC motor is connected to an adjustable power source for different input electric power to the actuator. The excitation frequency f (rotation speed of the cam) increases with the increase of the input electric power.

The motions of the mechanical system under different inputs are captured by a high speed camera. We used a sampling rate of 1000 frames per second for the motion capturing. The amplitude and frequency of the system is further analysed by post-processing of the captured photographs. Specifically, the dynamic behaviour of the system at small input power but resonant excitation frequency f ($58.8\,Hz$) and large input power with non-resonant oscillation ($200\,Hz$) are tested. The initial results of the tests for the mechanical system are presented below.

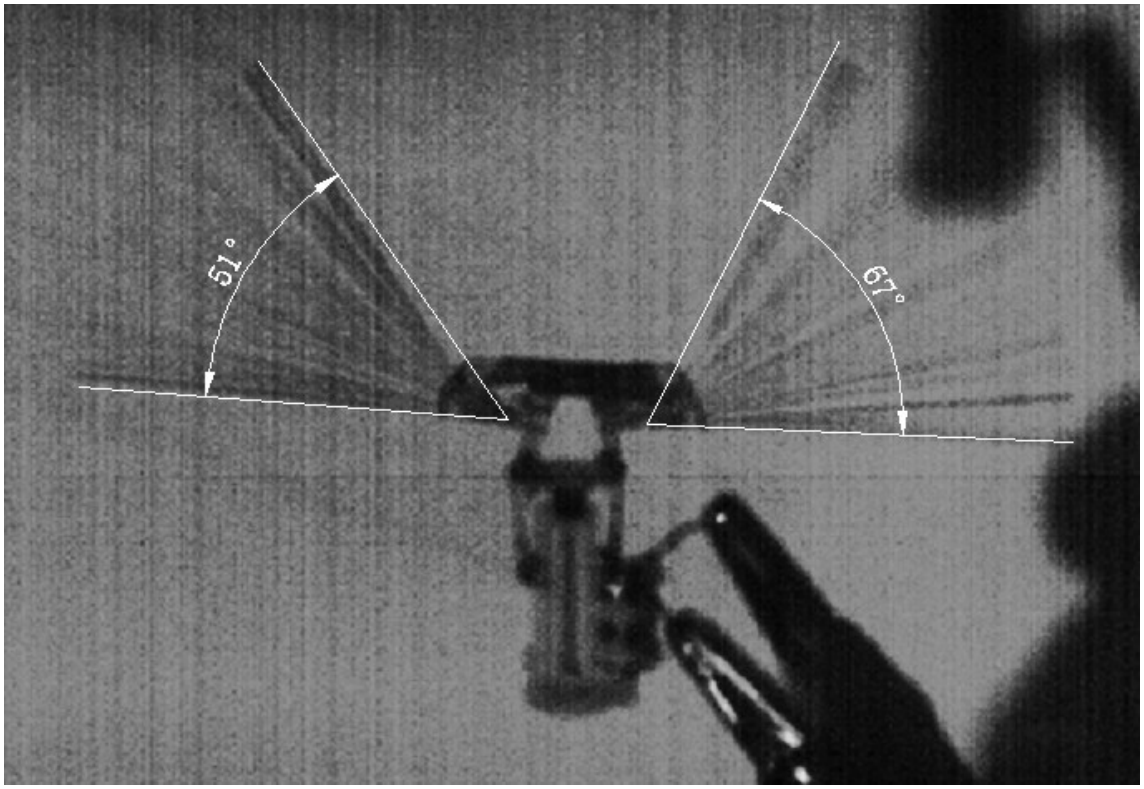

Figure 7-7 Subtractive graphical reconstruction of the captured flapping amplitude of the mechanical thorax at resonant oscillation (input excitation frequency f set to $58.8\ Hz$). Flapping amplitude reaches approximately $50°\sim70°$.

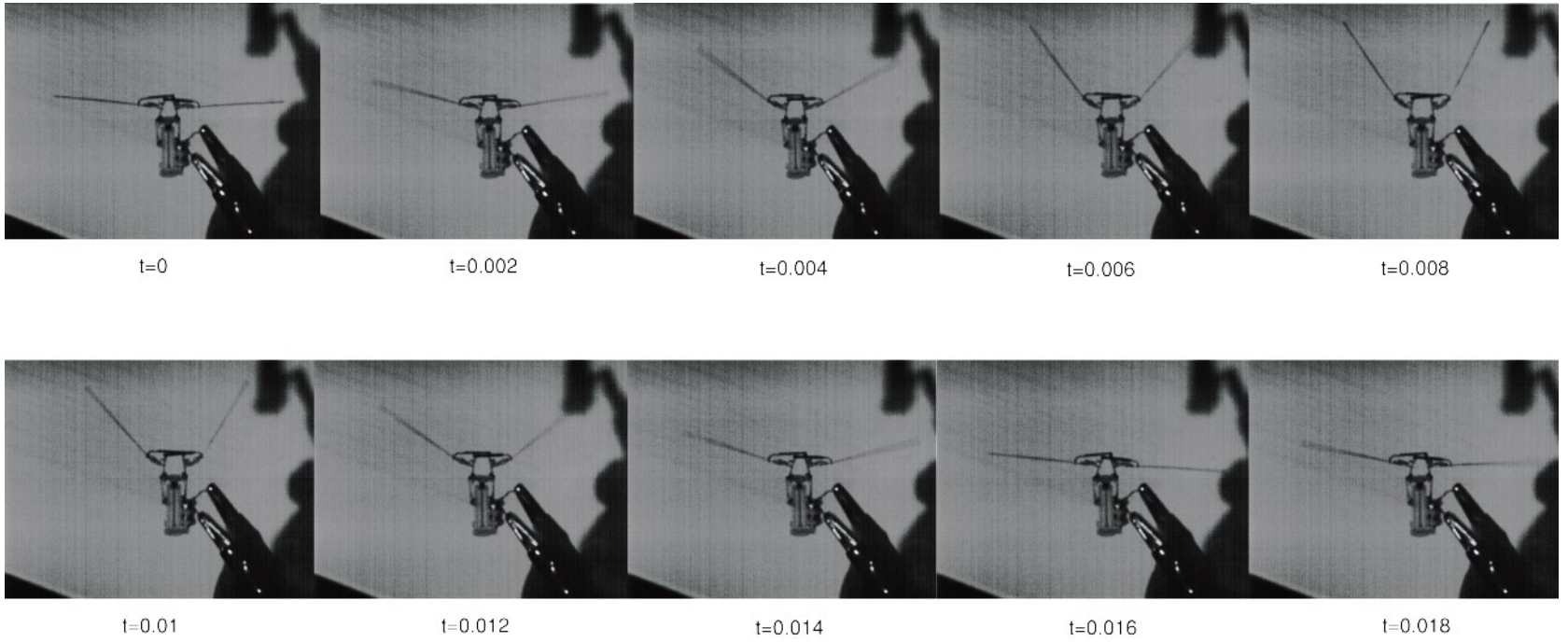

Figure 7-8 Captured motion sequences at resonant oscillation (input excitation frequency f set to $58.8\,Hz$). The time shown is actual time (unit in seconds).

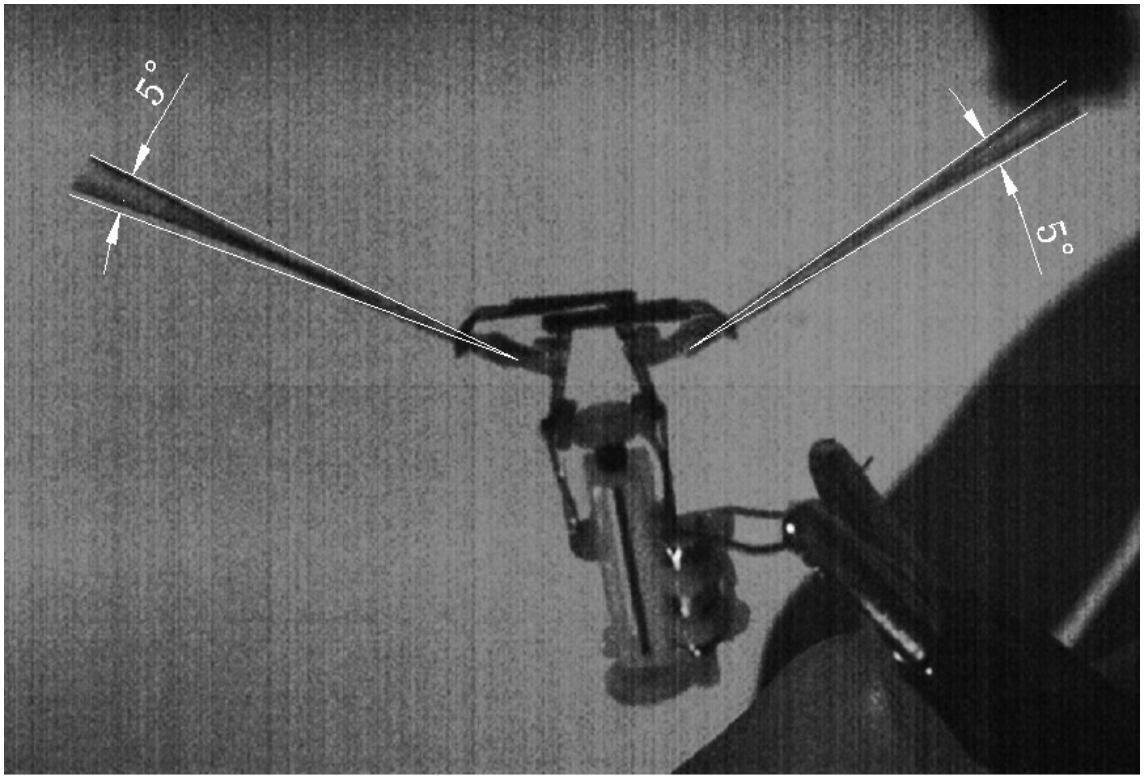

Figure 7-9 Subtractive graphical reconstruction of the captured flapping amplitude of the mechanical thorax at non-resonant oscillation (input excitation frequency f set to $200\ Hz$). Flapping amplitude is approximately $5°$.

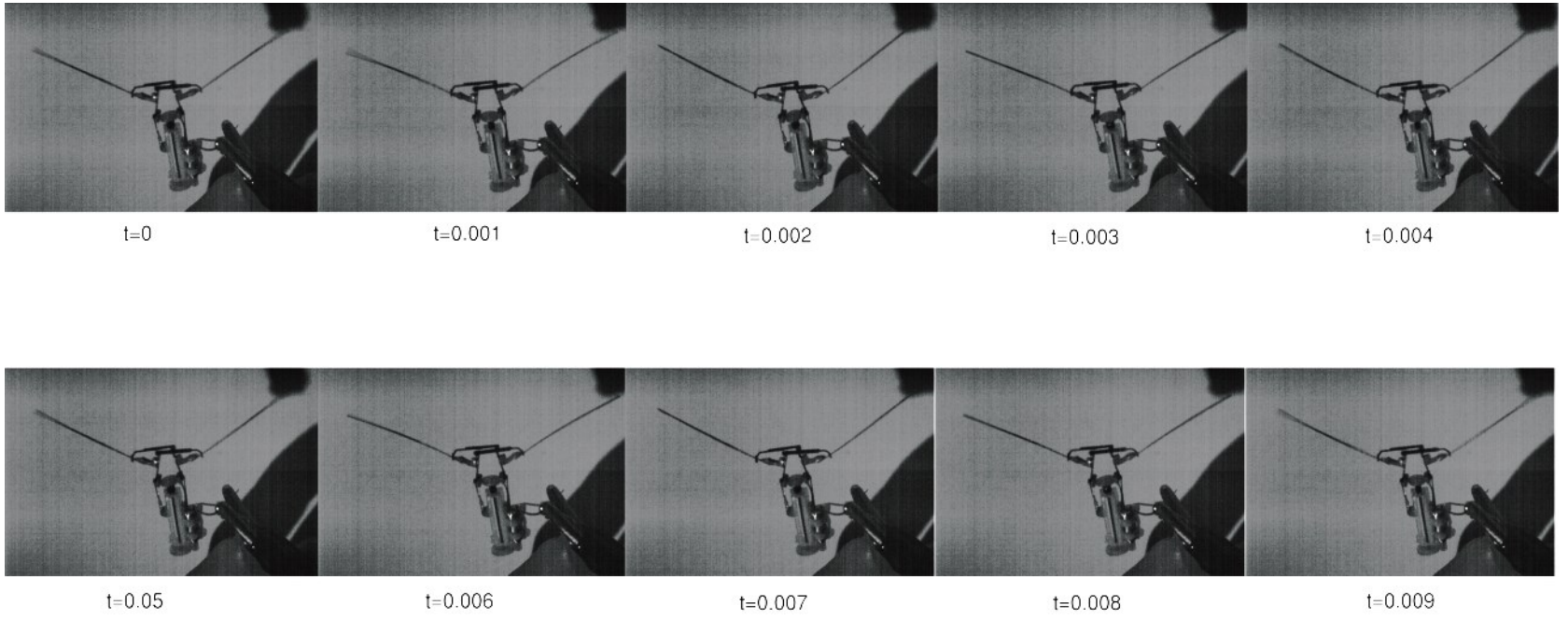

Figure 7-10 Captured motion sequences at non-resonant oscillation (input excitation frequency f set to $200\ Hz$). The time shown is actual time (unit in seconds).

7.4 **Discussions**

7.4.1 **Optimal design of the mechanical system for FWR**

For MAVs of microscopic scale, due to the limit of the power source and payload capability, the weight and energy efficiency is an important factor for design consideration.

Conventional design of the mechanical system for MAVs are restricted by the rotary motion of the actuator (electric motors), which in application of the biomimetic flapping wing MAVs design will cause excess weight and loss of efficiency due to the transmission of the rotary motion to the reciprocating flapping motion. Linear actuators, however, in the application of biomimetic flying robots have the potential of simple and light weight structures and compact mechanical systems (such as piezoelectric actuators).

In the sense of mechatronic design for FWR MAV, resonant systems with large amplitude of motion are the main design challenge. In our study, a novel 5-bar mechanical thorax system that is suitable for the application of micro FWR design is proposed. This mechanism is designed for linear actuators with small input motion. At resonant oscillation, the mechanism provides large amplitude flapping motion with maximized energy efficiency. Compared with the previously proposed 4-bar mechanism[57], the symmetric layout of the current design allows the motion of the two actuator bars to be transmitted to both left and right wings. Therefore, with the same number of actuators (two for two wings) and input displacements, the current design will yield much larger output motion.

In our analysis, the optimal amplification ratio of the 5-bar linkage mechanism is calculated with given constraints on the dimensions of the system. The optimized design is able to offer up to 30 times of amplification ratio of the output motion with respect to the input motion. Based on the calculation results, a practical design of the thorax mechanism with desirable output angles can be obtained.

For future studies, if the effect of length ratio of the 5-bar linkage system (such as the length ratio of the actuator bar AB to link bar BC) for the amplification ratio is also considered for optimization, further studies with multi-dimensional optimization procedures shall be applied.

7.4.2 **Feasibility of the resonant oscillation thorax**

The micro mechanical thorax is designed to work at a given oscillating frequency. At the resonant frequency of the mechanical system, the output flapping amplitude can be maximized with small input energy.

The initial tests of the manufactured resonant thorax system are shown in Figure 7-8~Figure 7-9. The two excitation frequency input to the system is $58.8\ Hz$ and $200\ Hz$, respectively. The subtractive graphical reconstructions of the captured flapping amplitude of the mechanical thorax show that the flapping amplitude reaches a maximum value of approximately $50°\sim70°$ at the resonant frequency of the system, which is much larger that the non-resonant oscillating frequency (approximately $5°$) case, despite the larger input power in the latter case. Thus, the proposed design is promising in application of biomimetic micro flapping wing MAVs with high energy efficiency.

The success of the initial design and tests indicates that the two-DOF resonant flapping wing mechanism would enable biomimetic flight with linear actuators for the desired input. In this case, problems regarding system dynamics, passive rotation of wing inertias, wing and link stiffness and damping, alignment of the flexures and the wing, interplay with surrounding fluids, control strategies and flight dynamics, etc. are very challenging for a successful thorax design, further studies in these areas are still required.

8 CONCLUSIONS

This thesis presents a systematic study on the aerodynamic and performance analysis and experiment of a novel FWR for MAV. In this last chapter, the main findings and conclusions of the study are summarised.

Kinematic and aerodynamic characterstics of the FWR MAV:

The FWR concept for MAV design combines both the insect-like flapping wing (dragonfly) kinematic pattern and the man-made rotary wing. The reciprocating flapping motion and the steady rotation motion are operated in the vertical direction and horizontal plane respectively. This unique kinematic pattern creates a 'quasi-steady' aerodynamic property for this type of MAV.

The dimensionless parameter η (see equation (3-47)) can be used to describe the relationship of the rotation and flapping motion and aerodynamic characterstics of the flapping wing. When η is zero, the kinematics of the wing is in pure flapping and the unsteady effects (added mass inertia and Kramer effect) strongly affect the instantaneous force production; as η increases, the flapping unsteady effects decreases; as η approaches infinity, the wing motion and aerodynamic force finally approaches steady rotation (see Figure 3-7). For a FWR in steady operation state (rotational speed reaches equilibrium and produce positive lift force), the value of η varies between 2~4 (see Figure 4-2 and Figure 4-3), the aerodynamic force production is 'quasi-static' (see Figure 3-7).

Quasi-steady aerodynamic estimations of FWR:

The quasi-steady aerodynamic model based on micro traditional flapping wing and rotorcraft test data has been extended to FWR aerodynamic calculation.

The instantaneous force calculated by the quasi-steady aerodynamic model agreed with the 3D CFD results (see Figure 3-11 and Table 3-1). Due to the computational efifciency and satisfactory accuracy, this quasi-steady aerodynamic model serves as an efficient tool for the initial design and analysis

of the FWR MAV. However, the excluded wing-wake interference and induced downwash effect on FWR performance needs further investigations.

Aerodynamic performance of FWR compared with other configurations:

Based on the aerodynamic analysis, the optimal kinematics of motion for the FWR and evaluation of its efficiency and potential application in comparison with other competitive MAVs has been made. The comparison of hovering aerodynamic efficiency of the FWR has been made with other two competitive configurations for MAV (conventional insect-like flapping wing and micro rotarcraft). The result shows that the FWR can produce the maximum lift coefficient larger than the other two, hence is better for payload carrying and performing rapid manoeuvre. It also shows that the FWR has comparable hovering efficiency with the other two, and all three types have their own advantages and application range for best performance (see Figure 4-6).

The FWR structure flexibility for aerodynamic performance:

One of the most challenging objectives to obtain a large aeroelastic twist of the flapping wing has been achieved in the study. The passive pitching mechanism serves as a simple design for the wing structure with minimal weight and structural complexity (see Figure 5-1). Passive pitching also helps to save energy cost for the design of a FWR MAV, since no extra power is needed to actively drive the pitching of the wing.

The test of FWR shows that by adjusting the wing's torsional stiffness, the desired wing motion can be obtained due to passive pitching dynamics of the wing structure.

The deformations of the wing structure (span-wise bending and chord-wise torsion) under aerodynamic loading and inertia loading will, in general, reduce the drive torque of the actuator and power consumption.

Also, since the deformation of the wing is sensitive to the force production, the flexible wing will 'smooth' the peak of the drive moment and power profile, which is beneficial for the actuator and power system.

Linear actuators and resonant mechanical thorax systems:

Linear actuators are promising for biomimetic flying robots application and have the potential to be applied for simple and light weight structures whilst being compact mechanical systems.

The proposed 5-bar mechanical thorax system is promising in application of biomimetic micro flapping wing MAVs with high energy efficiency. Compared with the previously proposed 4-bar mechanism[57], the symmetric layout of the current design is especially suitable for FWR configuration, and can yield much larger output flapping motion.

FWR concept feasibility and future work:

The theoretical analysis and the success of design, build and test of the flyable micro FWR model (FWR-EX1) has demonstrated the feasibility of the FWR concept and a step change of the FWR technology readiness.

However, in order to develop a fully operational FWR MAV that can perform sustained and controlled flight, the following topics need to be further investigated:

- Design and optimization of the airfoil for the desired aeroelastic deformations (such as insect wings) that minimize weight and maximize aerodynamic efficiency.
- Design and analysis of the system dynamics and structures of the 5-bar resonant mechanical thorax system for the optimal mechanical energy efficiency.
- Studies on the flight dynamics characteristics and stability of the FWR configuration, and sensors and control strategies for flight control systems.

REFERENCES

[1] Lentink, D. (2013), "Biomimetics: Flying like a fly", *Nature,* vol. 498, no. 7454, pp. 306-307.

[2] Guo, S., Li, D. and Huang, Z. (2009), "A smart material aeroelastic flapping wing micro rotorcraft", *International forum on aeroelasticity and structural dynamics,* .

[3] Guo, S., Li, D. and Wu, J. (2012), "Theoretical and experimental study of a piezoelectric flapping wing rotor for micro aerial vehicle", *Aerospace Science and Technology,* vol. 23, no. 1, pp. 429-438.

[4] Ellington, C. P. (1984), "The Aerodynamics of Hovering Insect Flight .4. Aerodynamic Mechanisms", *Philosophical Transactions of the Royal Society of London Series B-Biological Sciences,* vol. 305, no. 1122, pp. 79-&.

[5] Dickinson, M. H., Lehmann, F. O. and Sane, S. P. (1999), "Wing rotation and the aerodynamic basis of insect flight", *Science,* vol. 284, no. 5422, pp. 1954-1960.

[6] Sun, M. and Wu, J. H. (2003), "Aerodynamic force generation and power requirements in forward flight in a fruit fly with modeled wing motion", *Journal of Experimental Biology,* vol. 206, no. 17, pp. 3065-3083.

[7] Sun, M. (2005), "High-lift generation and power requirements of insect flight", *Fluid Dynamics Research,* vol. 37, no. 1-2, pp. 21-39.

[8] Wu, J. H. and Sun, M. (2005), "The influence of the wake of a flapping wing on the production of aerodynamic forces", *Acta Mechanica Sinica,* vol. 21, no. 5, pp. 411-418.

[9] Sun, M. and Tang, H. (2002), "Unsteady aerodynamic force generation by a model fruit fly wing in flapping motion", *Journal of Experimental Biology,* vol. 205, no. 1, pp. 55-70.

[10] Wang, Z. J. (2008), "Aerodynamic efficiency of flapping flight: analysis of a two-stroke model", *Journal of Experimental Biology,* vol. 211, no. 2, pp. 234-238.

[11] Pesavento, U. and Wang, Z. J. (2009), "Flapping Wing Flight Can Save Aerodynamic Power Compared to Steady Flight", *Physical Review Letters,* vol. 103, no. 11, pp. 118102.

[12] Lentink, D. and Dickinson, M. H. (2009), "Rotational accelerations stabilize leading edge vortices on revolving fly wings", *Journal of Experimental Biology,* vol. 212, no. 16, pp. 2705-2719.

[13] McMichael, J. M. and Francis, M. S. (1997), "Micro air vehicles-toward a new dimension in flight", *DARPA document,* .

[14] Pardesi, M. S. (2005), "Unmanned Aerial Vehicles/Unmanned Combat Aerial Vehicles", *Air & Space Power Journal,* , pp. 45-54.

[15] Pines, D. J., Bohorquez, F. A. and Sirohi, J. (2005), *Biomimetic mechanism for micro aircraft,* .

[16] Ellington, C. P. (1984), "The Aerodynamics of Hovering Insect Flight .3. Kinematics", *Philosophical Transactions of the Royal Society of London Series B-Biological Sciences,* vol. 305, no. 1122, pp. 41-&.

[17] Galinski, C. and Zbikowski, R. (2005), "Insect-like flapping wing mechanism based on a double spherical Scotch yoke", *Journal of the Royal Society, Interface / the Royal Society,* vol. 2, no. 3, pp. 223-235.

[18] Sane, S. P. and Dickinson, M. H. (2001), "The control of flight force by a flapping wing: Lift and drag production", *Journal of Experimental Biology,* vol. 204, no. 15, pp. 2607-2626.

[19] Wang, Z. J. (2004), "The role of drag in insect hovering", *The Journal of experimental biology,* vol. 207, no. Pt 23, pp. 4147-4155.

[20] Wang, Z. J. (2004), "The role of drag in insect hovering", *The Journal of experimental biology,* vol. 207, no. Pt 23, pp. 4147-4155.

[21] Weis-Fogh T (1973), *Quick Estimates of Flight Fitness in Hovering Animals Including Novel Mechanisms for Lift Production,* .

[22] Usherwood, J. R. and Ellington, C. P. (2002), "The aerodynamics of revolving wings - I. Model hawkmoth wings", *Journal of Experimental Biology,* vol. 205, no. 11, pp. 1547-1564.

[23] Sane, S. P. (2003), "The aerodynamics of insect flight", *The Journal of experimental biology,* vol. 206, no. Pt 23, pp. 4191-4208.

[24] Kramer, v. M. (1932), "Die Zunahme des Maximalauftriebes von Tragflugeln bei plotzlicher Anstellwinkelvergrosserung (Boeneffekt)", *Z.Flugtech.Motorluftschiff,* vol. 23, pp. 185-189.

[25] Sane, S. P. and Dickinson, M. H. (2002), "The aerodynamic effects of wing rotation and a revised quasi-steady model of flapping flight", *Journal of Experimental Biology,* vol. 205, no. 8, pp. 1087-1096.

[26] Birch, J. M. and Dickinson, M. H. (2003), "The influence of wing-wake interactions on the production of aerodynamic forces in flapping flight", *Journal of Experimental Biology,* vol. 206, no. 13, pp. 2257-2272.

[27] Rossby, C. and Montgomery, R. B. (1936), "On the momentum transfer at the sea surface. I. On the frictional force between air and water and on the occurrence of a laminar boundary layer next to the surface of the sea. II. Measurements of vertical gradient of wind over water. III. Transport of surface water due to the wind system over the North Atlantic", .

[28] Lentink, D., Muijres, F. T., Donker-Duyvis, F. J. and van Leeuwen, J. L. (2008), "Vortex-wake interactions of a flapping foil that models animal swimming and flight", *The Journal of experimental biology,* vol. 211, no. Pt 2, pp. 267-273.

[29] Wang, D., Wu, J. and Zhang, Y. "Aerodynamics on Flapping Rotary Wing in Low Reynolds Number", .

[30] Ellington, C. P. (1984), "The Aerodynamics of Hovering Insect Flight .1. the Quasi-Steady Analysis", *Philosophical Transactions of the Royal Society of London Series B-Biological Sciences,* vol. 305, no. 1122, pp. 1-15.

[31] Sedov, L. (1980), "Two-dimensional problems of hydrodynamics and aerodynamics", *Moscow Izdatel Nauka,* vol. 1.

[32] Wang, Z. J., Birch, J. M. and Dickinson, M. H. (2004), "Unsteady forces and flows in low Reynolds number hovering flight: two-dimensional computations vs robotic wing experiments", *Journal of Experimental Biology,* vol. 207, no. 3, pp. 449-460.

[33] Polhamus, E. C. (1971), "Predictions of vortex-lift characteristics by a leading-edge suctionanalogy", *Journal of Aircraft,* vol. 8, no. 4, pp. 193-199.

[34] Theodorsen, T. (1949), "General theory of aerodynamic instability and the mechanism of flutter", .

[35] Fung, Y. (2002), *An introduction to the theory of aeroelasticity,* Courier Corporation.

[36] Ellington, C. P. (1984), "The Aerodynamics of Hovering Insect Flight .5. a Vortex Theory", *Philosophical Transactions of the Royal Society of London Series B-Biological Sciences,* vol. 305, no. 1122, pp. 115-144.

[37] Stepniewski, W. Z. (1984), *Rotary-wing aerodynamics,* Courier Corporation.

[38] Birch, J. M. and Dickinson, M. H. (2003), "The influence of wing-wake interactions on the production of aerodynamic forces in flapping flight", *Journal of Experimental Biology,* vol. 206, no. 13, pp. 2257-2272.

[39] Berman, G. J. and Wang, Z. J. (2007), "Energy-minimizing kinematics in hovering insect flight", *Journal of Fluid Mechanics,* vol. 582, pp. 153-168.

[40] Dickinson, M. H. and Lighton, J. R. B. (1995), "Muscle Efficiency and Elastic Storage in the Flight Motor of Drosophila", *Science,* vol. 268, no. 5207, pp. 87-90.

[41] Dudley, R. and Ellington, C. P. (1990), "Mechanics of Forward Flight in Bumblebees .2. Quasi-Steady Lift and Power Requirements", *Journal of Experimental Biology,* vol. 148, pp. 53-88.

[42] Whitney, J. P. and Wood, R. J. (2010), "Aeromechanics of passive rotation in flapping flight", *Journal of Fluid Mechanics,* vol. 660, pp. 197-220.

[43] Dickinson, M. H. and Gotz, K. G. (1993), "Unsteady Aerodynamic Performance of Model Wings at Low Reynolds-Numbers", *Journal of Experimental Biology,* vol. 174, pp. 45-64.

[44] Wu, J. H. and Sun, M. (2004), "Unsteady aerodynamic forces of a flapping wing", *The Journal of experimental biology,* vol. 207, no. Pt 7, pp. 1137-1150.

[45] Ellington, C. P. (1984), "The Aerodynamics of Hovering Insect Flight .2. Morphological Parameters", *Philosophical Transactions of the Royal Society of London Series B-Biological Sciences,* vol. 305, no. 1122, pp. 17-40.

[46] Sun, M. and Du, G. (2003), "Lift and power requirements of hovering insect flight", *Acta Mechanica Sinica,* vol. 19, no. 5, pp. 458-469.

[47] Dickson, W. B., Straw, A. D., Poelma, C. and Dickinson, M. H. (2006), "An integrative model of insect flight control", *Proceedings of the 44th AIAA Aerospace Sciences Meeting and Exhibit,* pp. 31.

[48] Ellington, C. P. (1984), "The Aerodynamics of Hovering Insect Flight .6. Lift and Power Requirements", *Philosophical Transactions of the Royal Society of London Series B-Biological Sciences,* vol. 305, no. 1122, pp. 145-181.

[49] Sun, M. and Wu, J. H. (2003), "Aerodynamic force generation and power requirements in forward flight in a fruit fly with modeled wing motion", *Journal of Experimental Biology,* vol. 206, no. 17, pp. 3065-3083.

[50] Ruijgrok, G. J. (1990), *Elements of airplane performance,* Delft university press.

[51] Ennos, A. R. (1988), "The inertial cause of wing rotation in Diptera", *Journal of experimental biology,* vol. 140, no. 1, pp. 161-169.

[52] Zhao, L., Huang, Q., Deng, X. and Sane, S. P. (2010), "Aerodynamic effects of flexibility in flapping wings", *Journal of the Royal Society, Interface / the Royal Society,* vol. 7, no. 44, pp. 485-497.

[53] Shyy, W., Lian, Y., Tang, J., Liu, H., Trizila, P., Stanford, B., Bernal, L., Cesnik, C., Friedmann, P. and Ifju, P. (2008), "Computational aerodynamics of low Reynolds number plunging, pitching and flexible wings for MAV applications", *Acta Mechanica Sinica,* vol. 24, no. 4, pp. 351-373.

[54] Kamakoti, R. and Shyy, W. (2004), "Fluid–structure interaction for aeroelastic applications", *Progress in Aerospace Sciences,* vol. 40, no. 8, pp. 535-558.

[55] Ho, S., Nassef, H., Pornsinsirirak, N., Tai, Y. and Ho, C. (2003), "Unsteady aerodynamics and flow control for flapping wing flyers", *Progress in Aerospace Sciences,* vol. 39, no. 8, pp. 635-681.

[56] Wootton, R. J. (2010), "Springy shells, pliant plates and minimal motors: Abstracting the insect thorax to drive a micro-air vehicle", in *Flying insects and robots,* Springer, , pp. 207-217.

[57] Sitti, M. (2003), "Piezoelectrically actuated four-bar mechanism with two flexible links for micromechanical flying insect thorax", *Mechatronics, IEEE/ASME Transactions on,* vol. 8, no. 1, pp. 26-36.

APPENDICES

Appendix A Derivation of the Vector-form Formula for Induced Velocity Calculation of Flapping Wing

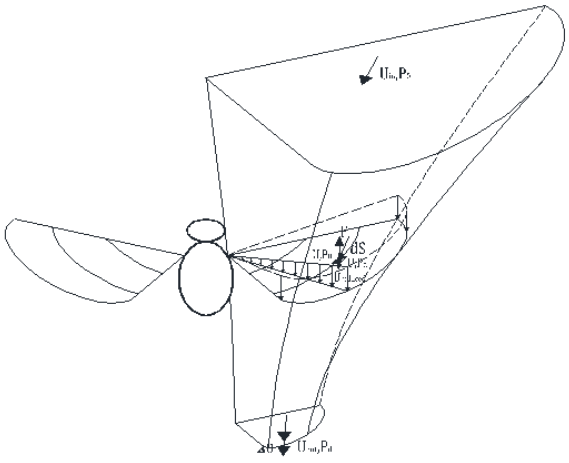

Figure A-1 Schematic of induced flow on single flapping wing. On the upstream far field, the flow has velocity vector $\mathbf{U_{in}}$ and pressure $\mathbf{P_0}$, the local flow velocity vector at the stroke surface is $\mathbf{U}$, and at the downstream far field, the flow has velocity vector $\mathbf{U_{out}}$ and restore the pressure $\mathbf{P_0}$.

Due to the coupled flapping and rotation kinematics of the FWR wing, it is convenient to calculate the induced velocity in vector form. Therefore, we derived the vector-form formula for the calculation of induced velocity of flapping wing based on the classical *Rankine-Froude momentum theory*[22; 37]. It can be seen that the vector form of the equations will apply not only to hovering flight, but also to other flight model (such as forward flight) and complicated kinematic motion of the wing.

The momentum theory simply models the flow as a pipe with a discontinuous surface at the stroke plane, where the flow energy is increased due to the rapid flapping of the wing. On the upstream far field, the flow has velocity vector $\mathbf{U_{in}}$ and pressure P_0. We first choose a small area on the stroke plane as the control surface dS, where the flow particles pass through this control surface and reach the velocity $\mathbf{U_{out}}$ and pressure P_0 at the downstream far field, as shown in Figure A-1. The average force vector generated by the wing on dS is $\mathbf{dF}$. It shall be

justified that this force will induce an opposite momentum in the flow, therefore, the resultant velocity of the flow particles pass through dS on the downstream far field is increased by $\mathbf{\Delta U}$ (assume the downstream flow is steady, irrotational and non-viscous). Apply Newton's second law, we have:

$$\mathbf{dF} = \dot{m}\mathbf{\Delta U} \tag{A-1}$$

In which $\dot{m}$ refers to the mass flow rate across the control surface dS, where the local flow has velocity vector $\mathbf{U}$, which equals to the vector sum of the far field velocity and the induced velocity, i.e.:

$$\mathbf{U} = \mathbf{U_{in}} + \mathbf{U_{induced}} \tag{A-2}$$

Therefore, the mass flow rate can be decided by the following equation:

$$\dot{m} = \rho\mathbf{U} \cdot \hat{\mathbf{n}}dS = \rho(\mathbf{U_{in}} + \mathbf{U_{induced}}) \cdot \hat{\mathbf{n}}dS \tag{A-3}$$

in which $\hat{\mathbf{n}}$ refers to the unit normal vector of the control surface. Therefore,

$$\mathbf{dF} = \rho(\mathbf{U_{in}} + \mathbf{U_{induced}}) \cdot \hat{\mathbf{n}} \cdot \mathbf{\Delta U}dS \tag{A-4}$$

Also, the force vector on the control surface can be decided by the pressure difference between the upper and lower surface, i.e.:

$$\mathbf{dF} = (P_d - P_u)dS\hat{\mathbf{n}} = \Delta P_{dS}\hat{\mathbf{n}}dS \tag{A-5}$$

Apply Bernoulli's principle on the upper and lower volume of the stroke plane, we have:

$$H_u = P_0 + \frac{1}{2}\rho\|\mathbf{U_{in}}\|^2 = P_u + \frac{1}{2}\rho\|\mathbf{U}\|^2 \tag{A-6}$$

and

$$H_d = P_0 + \frac{1}{2}\rho\|\mathbf{U_{out}}\|^2 = P_d + \frac{1}{2}\rho\|\mathbf{U}\|^2 \tag{A-7}$$

subtracting H_u from H_d yields:

$$\Delta P_{dS} = P_d - P_u = \frac{1}{2}\rho(\|\mathbf{U_{out}}\|^2 - \|\mathbf{U_{in}}\|^2) \tag{A-8}$$

$$= \frac{1}{2}\rho(\|\mathbf{U_{in}} + \mathbf{\Delta U}\|^2 - \|\mathbf{U_{in}}\|^2)$$

$$= \frac{1}{2}\rho(\|\mathbf{\Delta U}\|^2 + 2\mathbf{U_{in}} \cdot \mathbf{\Delta U})$$

$$= \rho\left(\frac{1}{2}\mathbf{\Delta U} + \mathbf{U_{in}}\right) \cdot \mathbf{\Delta U}$$

Therefore, combine equation (A-5) and (A-8) we have:

$$\mathbf{dF} = \rho\left(\frac{1}{2}\mathbf{\Delta U} + \mathbf{U_{in}}\right) \cdot \mathbf{\Delta U} \cdot \hat{\mathbf{n}} dS \quad \textbf{(A-9)}$$

Comparing equations (A-4) and (A-9), we have:

$$\mathbf{U_{induced}} = \frac{1}{2}\mathbf{\Delta U} \quad \textbf{(A-10)}$$

Therefore, taking equation (A-10) back to (A-4),we have:

$$\mathbf{dF} = 2\rho(\mathbf{U_{in}} + \mathbf{U_{induced}}) \cdot \hat{\mathbf{n}} \cdot \mathbf{U_{induced}} dS \quad \textbf{(A-11)}$$

This is the differential-vector form of the relationship of the induced velocity vector $\mathbf{U_{induced}}$, the aerodynamic force vector $\mathbf{dF}$ and the inflow velocity vector $\mathbf{U_{in}}$. Its validity relies on the assumption that the downstream flow of the differential control surface dS is steady, irrotational and non-viscous. Generally, for the FWR wing, due to the large vortex shedding and unsteady motion, this assumption does not hold, therefore, emprical studies that account for the corrections for the 'idealized flow' shall be applied.

Appendix B Characteristic Dimensionless Parameters of Insect Flapping Wing

Through the quasi-steady calculations, the variations of the characteristic dimensionless parameters (mean lift coefficient $\bar{C}_L$, mean drag coefficient $\bar{C}_D$, mean power coefficient $\bar{C}_P$ and power factor P_f) with the change of the geometric AoA (α_d and α_u) of insect flapping wing: the fruit fly-like kinematic pattern (flapping horizontally) and the dragonfly-like kinematic pattern (flapping vertically) are presented below.

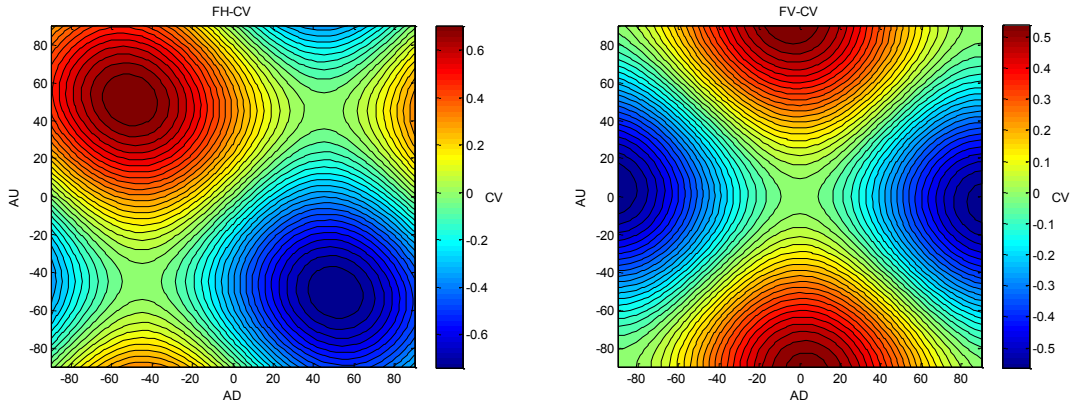

Figure B-1 The variations of Mean Lift Coefficients ($\bar{C}_L$) with the change of geometric AoA (ranging from $-90°\sim90°$) of flapping insect wing.

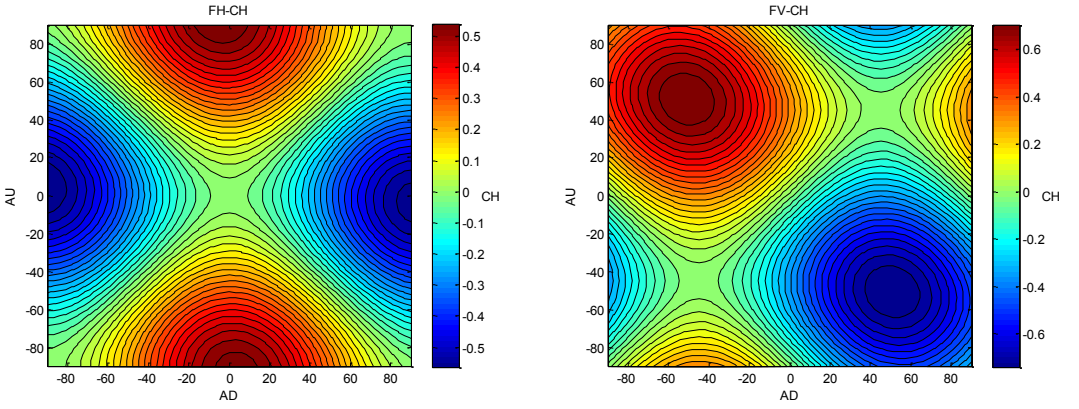

Figure B-2 The variations of Mean Drag Coefficients ($\bar{C}_D$) with the change of geometric AoA (ranging from $-90°\sim90°$) of flapping insect wing.

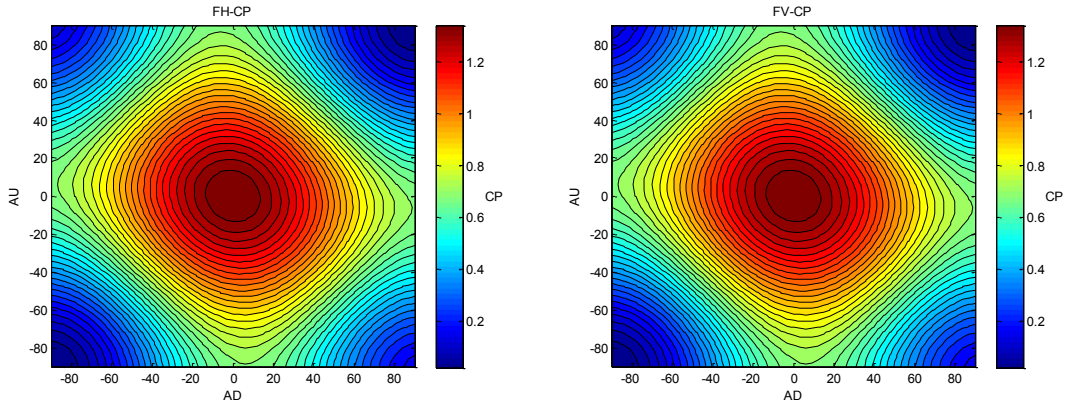

Figure B-3 The variations of Mean Power Coefficients ($\bar{C}_P$) with the change of geometric AoA (ranging from $-90°\sim90°$) of flapping insect wing.

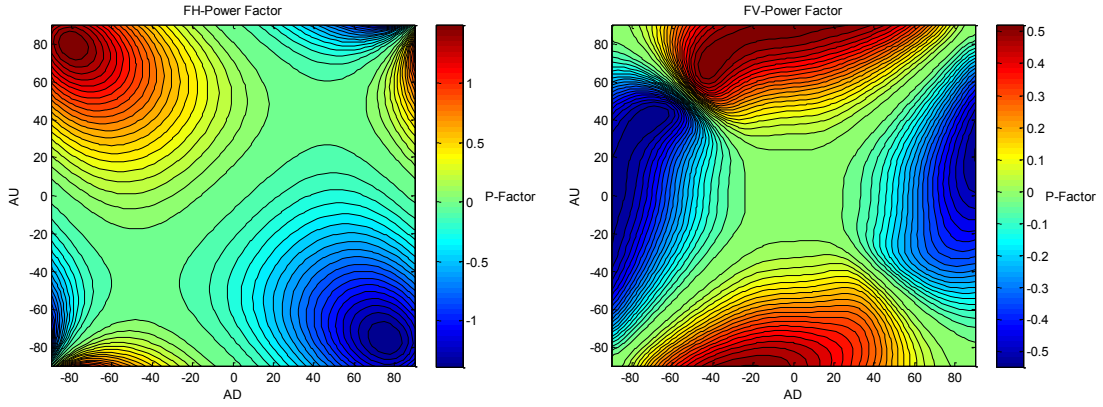

Figure B-4 The variations of Power Factors (P_f) with the change of geometric AoA (ranging from $-90°\sim90°$) of flapping insect wing.

In the above figures, FH indicates fruit fly-like kinematic (flapping horizontally); FV indicates dragonfly-like kinematics (flapping vertically); α_d and α_u indicates the geometric AoA at mid-downstroke and mid-upstroke, respectively (for definition, see chapter 3.2). The pseudocolor represents the magnitude of the corresponding dimensionless parameters ($\bar{C}_L$, $\bar{C}_D$, $\bar{C}_P$ and P_f).